Nanofabrication and Characterization of Photonic Crystals

Thesis by

Chuan-cheng Cheng

In Partial Fulfillment of the Requirements

for the Degree of

Doctor of Philosophy

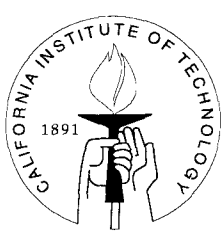

California Institute of Technology

Pasadena, California

1998

(Submitted April 30, 1998)

Acknowledgements

I would like to thank all the people who have supported and helped me during the five years of study and research at Caltech. In particular, I would like to acknowledge my academic advisor, Professor Axel Scherer. It was Professor Scherer who brought me into this exciting field of nanofabrication. More importantly, he has provided me the key ideas, professional guidance and supports through all these years. Above all, his patience and encouragement, like an invaluable friend, were always present to me when I needed it. His wife, Dr. Teresa Cheeks, also deserves my special thanks for her support.

Caltech has been for me a fantastic environment to work and to study. I am very grateful to Professors Amnon Yariv and William Bridges for their inspiration on the field of optoelectronics. I would like to thank Professor Michael Roukes for his kindness and support for sharing the microfabrication facilities. Special thanks to Professor Tom Tombrello for his excellent ideas about spectral tuning of photonic crystals. I am also grateful to Professors Kelly Vahala, Demetri Psaltis, Nai-Chang Yeh, and Yu-Chong Tai for letting me share their knowledge and thinking.

In particular, I would like to thank Professor Eli Yablonovitch in electrical engineering of University of California, Los Angeles. His brilliant idea about photonic bandgap crystals opens my view and leads me to the most advanced project "photonic band engineering." And Professor Yeshayahu Fainman in electrical engineering of University of California, San Diego, also deserves my special thanks for his great support on "micropolarizing beam splitter" project.

I am also grateful to Dr. John O'Brien, Dr. Andrew Cleland, Dr. Tom Tight, Dr. John Hartman, Dr. Thomas Krauss, and Dr. Tomoyoki Yoshi who shared their knowledge and valuable suggestions with me. I am indebted to Reginald Lee, a close collaborator and friend, who always devoted his time to help me when I needed it. And thanks to all the people who have devoted their time to help me such as Ali

Ghaffari, Yong Xu, and Zhiwen Liu from Dr. Yariv's group for "hemisphere lenses" project, Frank Monzon, Darrell Harrington, Melissa Midzor, Keith Schwab and Nils Asplund from Dr. Roukes's group, Wen Hsieh, Dr. Thomas Tsao, and Ellis Meng from Dr. Tai's group, Dr. Steve Yamamoto, Dr. Robert O'Barr, Mladen Todorovic from CMRR, UCSD.

I deeply thank the fellow members of the research project teams at UCLA, especially, Dr. Vincent Arbet-Engels, Dan Sievenspiper, George Witzgall, and Patty Chang-Chien who gave me numerous helps on the characterization of 3D photonic crystals and microwave models. I also thank the members at UCSD, especially Dr. Fang Xu and Rong-Chung Tyan who helped me on the design and characterization of micropolarizing beam splitters. I would like to thank the National Science Foundation (NSF) and MURI program in the Army Research Office for their financial support in the past five years.

The research partners in our group always present their great help during my study. In particular, I would like to thank Oskar Painter who always inspires me with his smart thinking and helps me improve my computer skills. I am also indebted to Joyce Wong, who always shows her patience and helps me organize the lab. I would like to thank the past member of the group, Weihua Xu, who together shared the wonderful experience of the first few years of working in the lab. I am also grateful to Hou-pu Chou, Jelena Vukovic, David Barsic, Marko Loncar, Brian D'Urso, and Oliver Dial for their support and help. Good Luck to David, who is the man for all my nasty jobs. I am always impressed by Brian and Oliver for their excellent programs which save me a lot of time. I will never forget Michelle Vine, who is not only the greatest secretary but also the greatest cookie maker. I would also like to thank Reynold Johnson who always makes my life in the lab easier.

I am very grateful to all the past and present members of Caltech Taiwanese Graduate Association, especially Dr. Chieh-Ming Liu, Dr. See-May Phoong, Dr. Pei-Lin Chen, Dr. Chao-Ping Hsu, Dr. Donald Lie, Dr. Richard Ping Chen, Dr. Jung-Fu Cheng, Dr. Ching-Tung Huang, Dr. Chi-Ming Yang, Dr. Yuan-Pei Lin, Dr. Pei-Long Chen, Dr. Jung-Chi Chiao, Po-An Sung, Dr. Lih-Yuan Lin, and Dr.

Wei Chang for their great friendship and guidance through my study. I also wish the great success for all the present members, Hsiao-Ching Hung, Hui-Ming Hung, Meina Xu, Joyce Peng, Samuel Tang, and Tzu-Jung Yao.

I would like to thank my long time friends, Chia-Pei Lee, Annie Liang-Hui Lee, Min-Jay Wang, for whom I spent a lot on phone bills, and Dr. Woe-jer Lee and his family, Meihui Su and Kenny Lee. Special thanks to Albert Chun-Ming Wang, who together shared the exciting moments through years at Caltech.

Finally, my parents, my sister, Shu-kuang Chen, and brother-in-law, Dr. HsinFu Wang, deserve the credit for guiding me toward great success and endless support. My dearest wife, Hsi-I Yang, who is always patient and supportive in my life and gives me the most comfortable home when I come back from work. For their unassuming love, I can not thank them enough.

Abstract

Both techniques and applications of nanofabrication have been explored in the field of periodic dielectric nanostructures. These periodic dielectric structures are expected to exhibit interesting properties in both fields of physics and engineering. These artificial nanostructures are named "photonic crystals" because photons demonstrate similar behavior in these structures as electrons in natural semiconductor crystals. In order to construct these crystals in the optical regime, suitable nanofabrication techniques have to be developed and demonstrated, including high resolution electron beam lithography and anisotropic chemically assisted ion beam etching. In this work, both 2D and 3D photonic crystals are fabricated and characterized in the near-infrared range.

In the first part of this thesis, exploration of resolution limit of nanofabrication will be demonstrated and discussed. 15nm structures with 30nm period dot arrays and 20nm line width with 40nm period gratings are presented. Along with high resolution lithography, anisotropic pattern transfer is also developed. These powerful fabrication techniques enable us to miniaturize the dimension of both electronic and optical devices into the nanometer regime.

In the second and third part of this thesis, detailed experiments and characterization of 2D and 3D photonic crystals are discussed. A brief introduction and a theoretical simulation are also presented. In the second part, computer generated form-birefringent nanostructures are first discussed and their performance demonstrated to agree well with design using rigorous coupled wave analysis (RCWA). In-plane 2D photonic crystals used as beam splitting micropolarizers are introduced and fabricated. High extinction ratios (>820:1) between transmitted TE and TM modes are measured. These in-plane photonic crystals are the first working devices using the idea of 2D photonic crystals. Three-dimensional artificial photonic crystals with a complete 3D bandgap represent a more attractive idea.

In the third part of this thesis, we challenge the nanofabrication limits encountered when fabricating a 3D photonic crystal. The first three-dimensional photonic crystals with a forbidden photonic bandgap lying in the near infrared region of the electromagnetic spectrum, 1.1 μm $< \lambda <$ 1.5 μm, just beyond the electronic band-edge of Gallium Arsenide (GaAs) are demonstrated in the world. These 3D photonic crystals were originally proposed by E. Yablonovitch and can now be fabricated using anisotropic angle etching at three directions through a hexagonal hole array mask. The field distribution using filtered finite-difference time-domain (FFDTD) calculation is briefly discussed. Development of the fabrication techniques and the optical transmission characterization are shown. Photonic crystals with up to six repeating layers are obtained and presented 90% attenuation of transmission measurement in the bandgap region. We also show the spectral shift in the transmission measurement corresponding with 2D lithographic control of microfabrication. Those artificial photonic crystals are expected to be useful in the study of inhibition of spontaneous emission and single-mode light-emitting diodes.

Contents

List of Figures

List of Tables

Part I

The exploration of resolution limit of nanofabrication

Chapter 1 Introduction and motivation

1.1 Motivation

When observing the beauty of the microfabrication, which now integrates millions of transistors on a square inches chip, I start to believe that there is a broad world which is invisible to human eyes. I truly believe that I am not only an engineer but also an architect building this tiny world. Lithography and etching are our powerful tools. Recently, the research and development of these technologies from experts have made the fastest progress. Combined with these powerful tools, knowledge and a little imagination can lead us to explore this whole new world. Our goal is to develop and to utilize advanced fabrication techniques in the field of next generation semiconductor devices.

1.2 History of exploration of resolution

When the size of the transistors becomes smaller and the number of the transistors exponentially increases on a square inch chip [8], the resolution of lithography always plays a very important role in the development of microfabrication technologies [9]. During the last twenty years, photolithography has decreased the minimum feature size from 2μm down to 0.25μm through the continuous improvement of optics, masks, and resists. With the diffraction limit of light, photolithography requires progressively shorter wavelength light sources such as i-line, excimer, DUV, as well as modification of phase shift masks. In the meantime, various alternative lithography techniques have been developed to generate sub-100nm structures. Electron beam lithography, X-ray lithography and atomic beam lithography have demonstrated excellent resolution for the next generation devices [1, 10, 11]. These techniques all share the common advantage over photolithography in that the source has a much shorter wavelength

which reduces the diffraction limit. But the complexity of these lithography systems increases the cost and the difficulty.

The principle of X-ray proximity printing is similar to that of photolithography [11]. The high cost of synchrotron X-ray sources, the reflective X-ray masks, and the precise requirement of mask alignment are the key disadvantages. Electron microscopes have been developed since the 1930s [12]. The sophisticated electron lenses and electron sources enable electron beams to be focused to a very small spot size (<1nm) without aberration. Electron beam direct writing has many advantages such as resolution, flexibility, and alignment accuracy, but suffers from a low throughput. Commercial electron beam writers usually sacrifice resolution to decrease exposure time by using large beam currents. High acceleration voltages are also commonly used in the commercial beam writer to avoid proximity effect exposure of the resist by electron back scattered from the substrate. Scanning electron microscopes (SEM) usually have higher resolution in order to image nanostructures. Therefore, converting a scanning electron microscope into an electron beam writer gives us a significantly better resolution and an instrument which is ideally suited for research of nanostructures.

1.3 High resolution lithography

The progress of new fabrication technologies has enabled us to miniaturize the dimension of the devices smaller than the wavelength of the light. Lithography is the most critical procedure of defining dimensions of such structures. Smaller structures have been obtained by various state-of-the-art technologies. Figure 1.1 shows the progress of lithography resolution [1]. When the dimensions of the structures approach the wavelength of the light, optical lithography suffers from the diffraction limit. Therefore, new types of lithography systems with higher resolution are desired including electron beam direct writing, EUV lithography, or X-ray proximity printing, since X-ray and electron beam have smaller effective wavelength about 1nm and 0.3nm, respectively.

X-ray lithography usually requires precise mask fabrication and careful alignment for 1:1 proximity printing. The practical resolution of proximity printing is expressed by R $\propto \sqrt{\lambda d}$ where λ is the wavelength of X-ray and d is the separation between mask and wafer which is around 10-20μm. So the minimum resolution of 1:1 X-ray proximity printing is approximately 50nm.

In contrast, electron beam direct writing is a maskless lithography which offers the great flexibility in design and process. The De Broglie wavelength of the electron is expressed by

$$\begin{aligned} \lambda &= \frac{h}{\sqrt{2mE_0}} \\ &= \frac{1.24}{\sqrt{E_0}} \end{aligned}$$

where E_0 is the energy of the electron in electron volts and λ is in nanometer. It is typically a few tenths of angstroms, and the diffraction limitation in optical lithography no longer applied. The resolution of electron beam lithography is limited by the electron scattering in the resist layer and various aberrations of electron optics. When electrons are incident on a resist layer, they lose energy by scattering and generate secondary electrons. The profile of the electron scattering depends on the resist thickness, beam energy, and substrate composition [12]. The other important effect is the proximity effect which results from back scattering of electrons from the substrate [13].

Recently, commercial electron microscopes with excellent electron optics have become available. Therefore, high resolution patterns can be generated by adjusting the beam voltage and the thickness and the composition of the resist layer [14, 15, 16, 17, 18]. Once the high resolution patterns are lithographically defined, pattern transfer without distortion is required. Typically, electron beam resist is not as strong as photoresist during etching processes. Multilayer resist or mask amplification processes can be used to solve the problem. Anisotropic transferred structures with high aspect ratios are obtained by chemically assisted ion beam etching. Details of the work are described in the Appendix A.

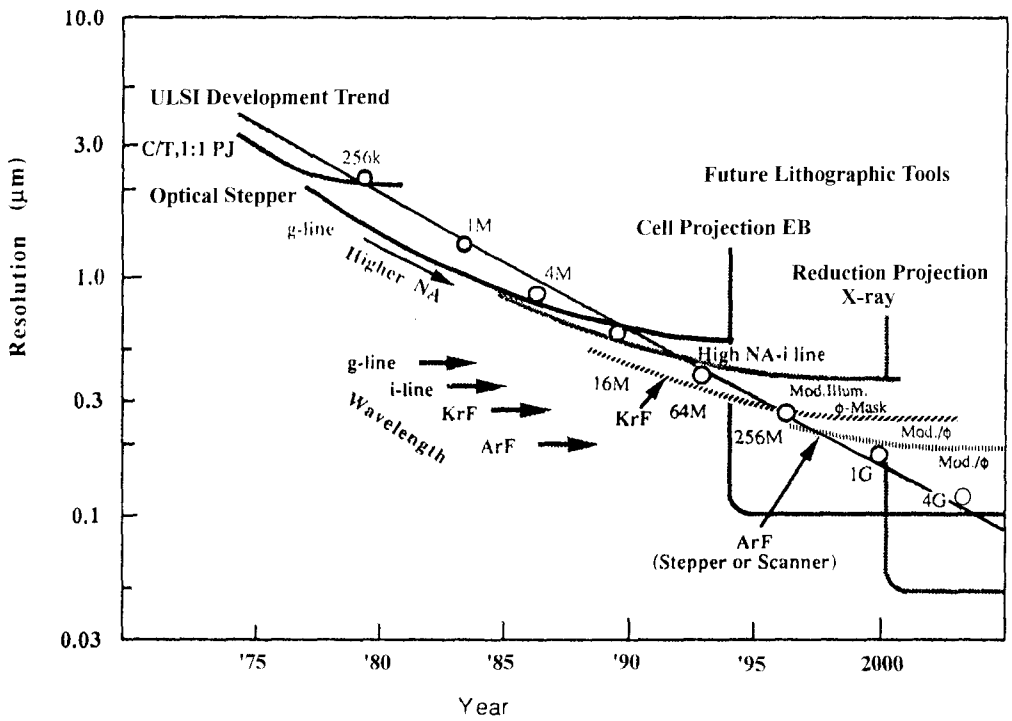

Figure 1.1: Trend of the lithography for nanofabrication, after S. Okazaki 1993 [1]

1.4 Electron beam lithography system

In this chapter, we would like to demonstrate fabrication method for building high density nanostructures using electron beam lithography. These small structures are expected to be useful in the study of electronic and optical devices and nanomagnets [19]. The lithography is conducted in a commercial scanning electron microscope (Hitachi S-4500 II) with a cold field-emission tip. Figure 1.2 shows a scheme of the whole system setup.

The computer generates X/Y scanning signals from an AutoCAD file and sends them to a scan coil of the SEM through a 16bit D/A card. The field of view is about 200μm at 500X magnification. Therefore, the distance between each individual pixel can be expressed by

$$d = \frac{200\mu m \times 500X}{Magnification \times 2^{16}}$$

The distance between each pixel is about 3nm at 500X. The exposure dose is maintained at a constant level by dynamically monitoring the beam current through a floating objective aperture. Automatic stage control increases the flexibility of the system. The whole system is located on an isolated foundation slab to reduce the vibration noise from the building. The field-emission tip is free from thermionic emission and has the smallest effective source size compared with the other types of electron sources such as tungsten and LaB_6. It offers a suitable probe size for high resolution electron beam lithography. The lower acceleration voltage ranging from 500V to 30kV further reduces the proximity effect which is more serious due to the backscattering electrons from high energy incident electrons. Some of the smallest structures have been reported by using high voltage electron beam lithography (typically $>$ 50kV) or using inorganic resists such as AlF_3 or CaF_2 [20, 21, 22]. The goal of this work is to reach the resolution limit using PMMA as a positive resist with conventional beam voltages ($<$ 40kV) using a standard electron beam lithography process.

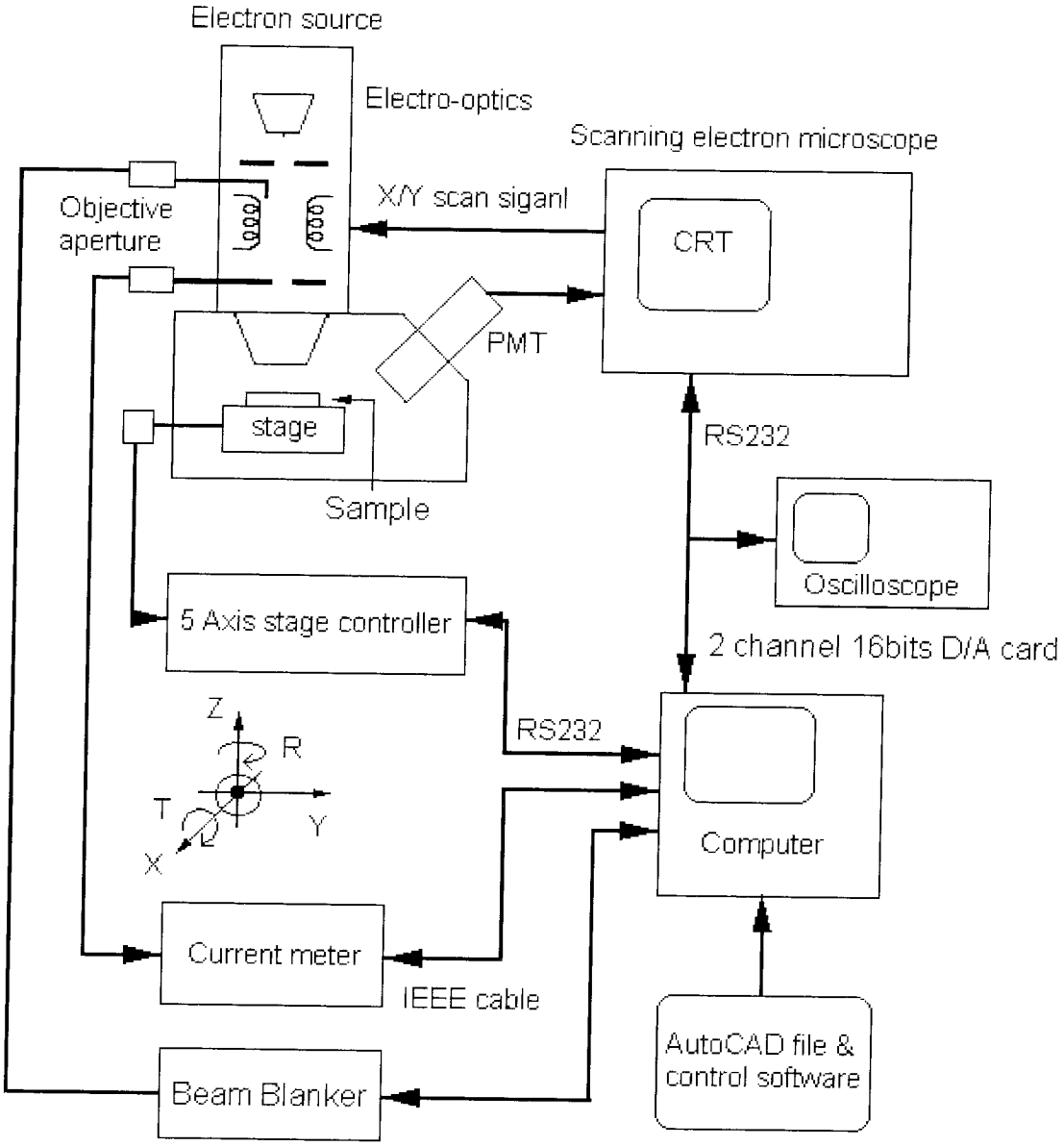

Figure 1.2: Scheme of an electron beam lithography system modified from a scanning electron microscope with computer control

Chapter 2 Experimental approach

2.1 Calibration and alignment

Alignment is performed before electron beam lithography, since a small spot size is necessary for high resolution electron beam writing. Typically, small beam current, small objective aperture, and short working distance are adjusted to get the smallest probe size. The beam current is measured through a Faraday cup and adjusted by changing the focus of the condenser lens and the size of the objective aperture. The beam spot size is measured by scanning over a sharp edge on the wafer and then determined by the contrast of the curve [12]. Figure 2.1 shows the spot size and beam current as a function of acceleration voltage at the different condenser lens settings. The higher the acceleration voltage, the higher the beam current and the smaller the beam probe size. But the probe size saturates at around 4-7nm due to the noise from vibration and alignment as well as the error from the scan signal measurement. In addition to a small probe size, a large depth of focus is also required for performing lithography over large areas. The definition of depth of focus is

$$D = \frac{2r}{\alpha} \quad and \quad \alpha = \frac{R}{WD}$$

where r is spotsize, R is diameter of objective aperture, and WD is working distance. A low atomic weight substrate can be prepared to reduce the backscattering electron exposure. Exposure dose and development condition are both very important in the process of making nanostructures. PMMA electron beam resist usually requires exposure dose about $100\mu C/cm^2$. Figure 2.2 shows that the best feature size versus development time when optimize the exposure dose at 30kV accelerated voltage. We have tried two different development procedures. One is a conventional 3:7 cellusive : methanol mixture, the other is pure IPA (isopropyl alcohol). We found that the

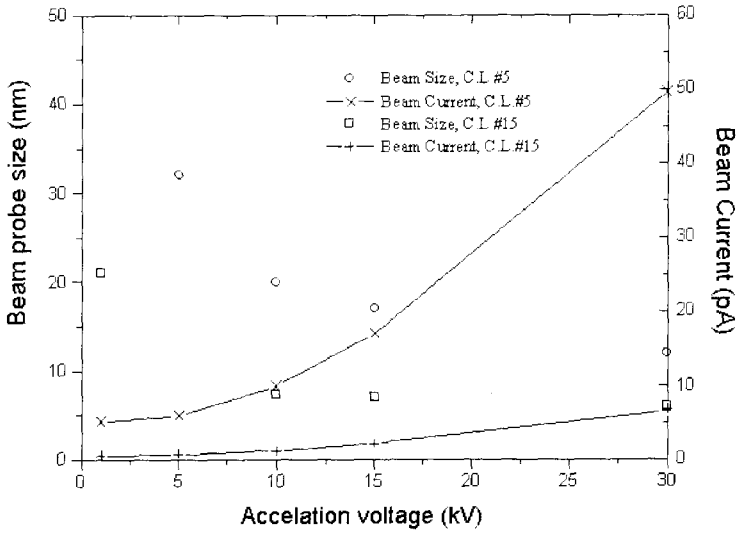

Figure 2.1: Measured beam probe size and beam current as a function of acceleration voltage

best feature size can be obtained by developing the sample in IPA for 15 seconds. We could control the developing time within +/- 1 second. [23]

The experimental approach for exploration of ultimate resolution using electron beam lithography is shown schematically in Figure 2.3. First, a 15nm Gold Palladium (AuPd) layer is sputtered on the top of a Silicon (Si) or GaAs wafer and a thin 40nm high molecular weight PMMA (poly-methyl methacylate) layer is spun on. Then the wafer is baked at 150°C in an oven for one day. Another 2 minute hot plate bake at 180°C is performed immediately before the exposure to promote adhesion. The 30KV electron beam with a spot size around 4nm exposes the desired pattern generated by AutoCAD on the PMMA layer. Exposure doses ranging from 4.15 mC/cm^2 to 12.5 mC/cm^2 are used to find the best exposure range for dot arrays. And the exposure dose for gratings is around 1 nC/cm^2. This sample is then developed in pure IPA at room temperature and dried in Nitrogen (N_2). Next, the pattern is transferred into the AuPd layer by argon ion milling using 10mA beam current and 1500V beam voltage. This AuPd layer can then be used for further mask amplification and etching.

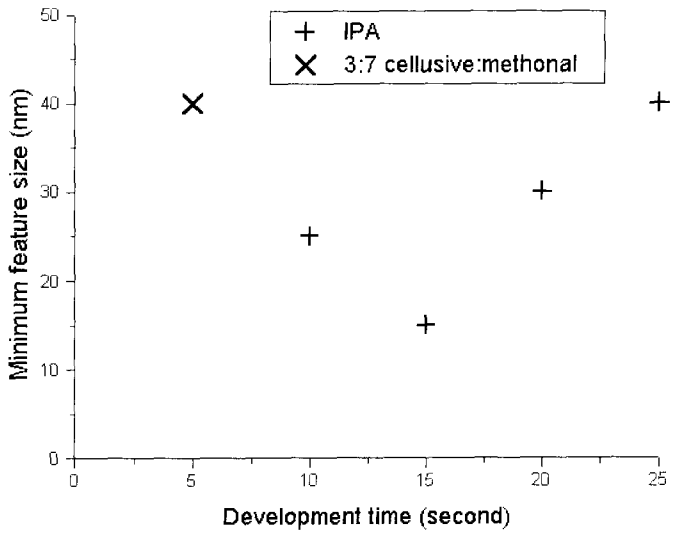

Figure 2.2: Minimum feature size as a function of development time using IPA and 3:7 cellusive:methonal

Finally we determine the resolution of the pattern by using the same scanning electron microscope.

2.2 Result of lithography resolution

To test the resolution of the SEM, 20nm wide lines with 40nm pitch gratings were defined on the AuPd layer. Similarly, 15nm diameter dots with 30nm pitch arrays were written by using the fabrication procedure described above. Figures 2.4 and 2.5 show the SEM images of these two high density nanostructures. A 15 second development in pure IPA gives the best resolution of 15nm structures with a period ranging from 30nm to 80nm. In order to confirm the clean development process, lift-off experiments are conducted. Figure 2.6 shows a SEM image of 40nm pitch AuPd short line on GaAs by sputter deposition. Some flags after lift-off process can be seen because of conformal deposition. Figure 2.7 shows a SEM image of 20nm wide and 60nm pitch Au bars on GaAs by vapor deposition. Uniform structures can be

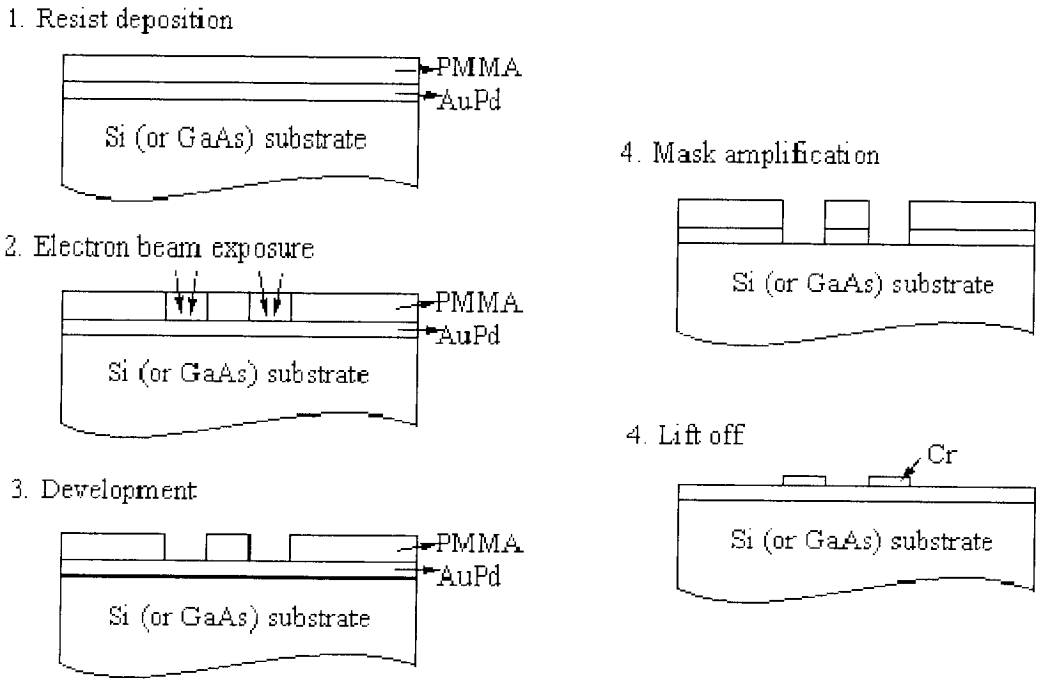

Figure 2.3: Procedure of electron beam lithography

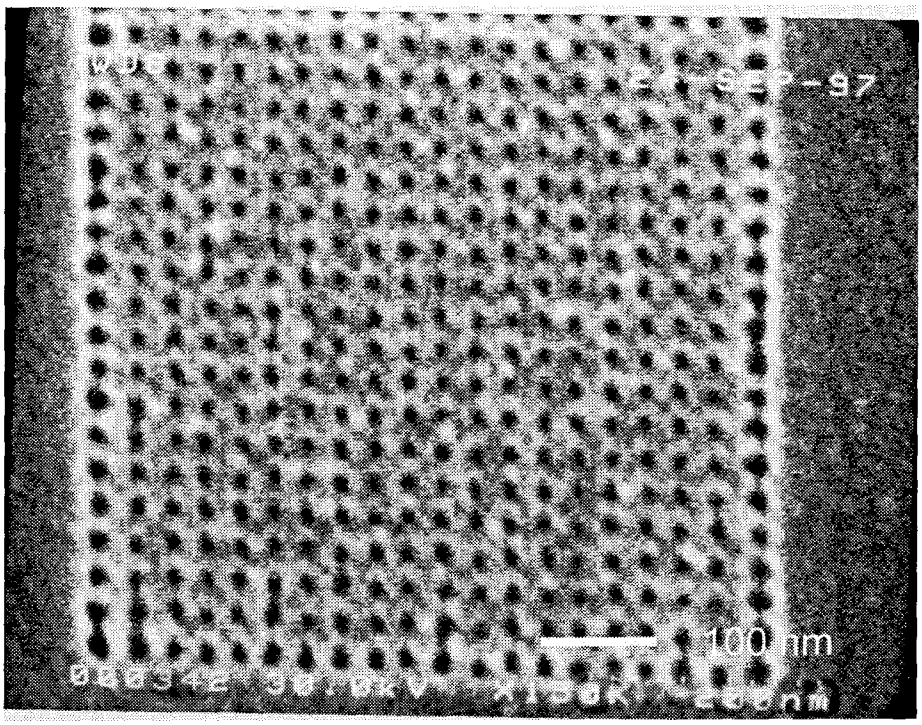

Figure 2.4: SEM image of 15nm diameter dots with 30nm pitch arrays on Si

obtained by directional deposition.

The hot plate baked before the exposure was found to enhance the adhesion of PMMA during the development. Figure 2.8 shows the SEM images of the difference between the developed pattern with and without the prebaked procedure. The flexibility of EB lithography can be found in the SEM image of a Caltech logo made by the same process (see Figure 2.9). This complicated pattern can be designed in different layers which can be exposed with different dosages.

2.3 Discussion

We have successfully converted a commercial SEM to a high resolution electron beam lithography system. We have also demonstrated a fabrication process to generate high density nanostructures using electron beam lithography with conventional beam voltage, PMMA resist, and IPA developer. To further improve the resolution of the

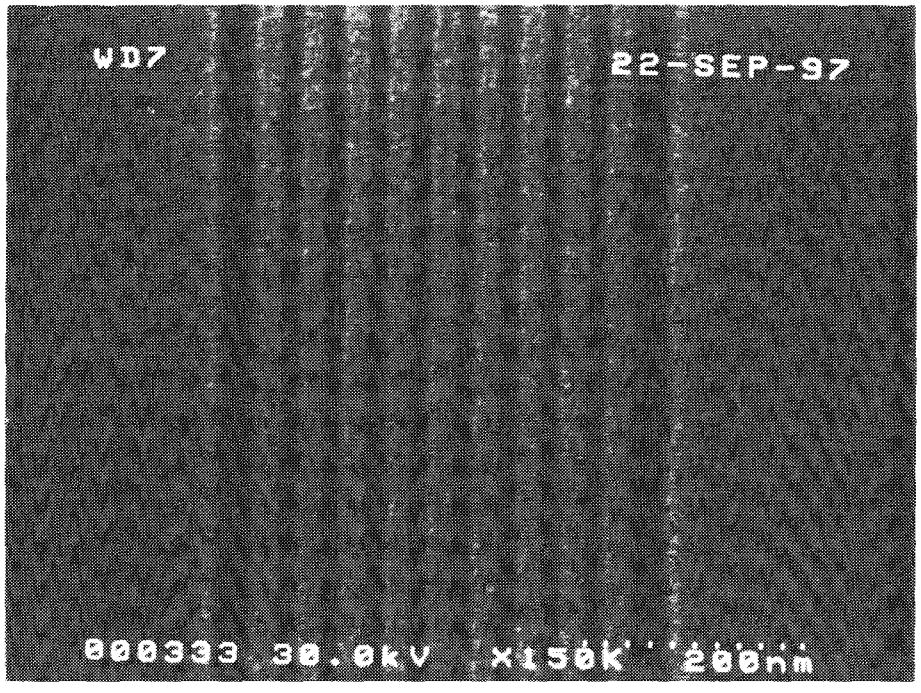

Figure 2.5: SEM image of 20nm wide lines with 40nm period gratings on Si

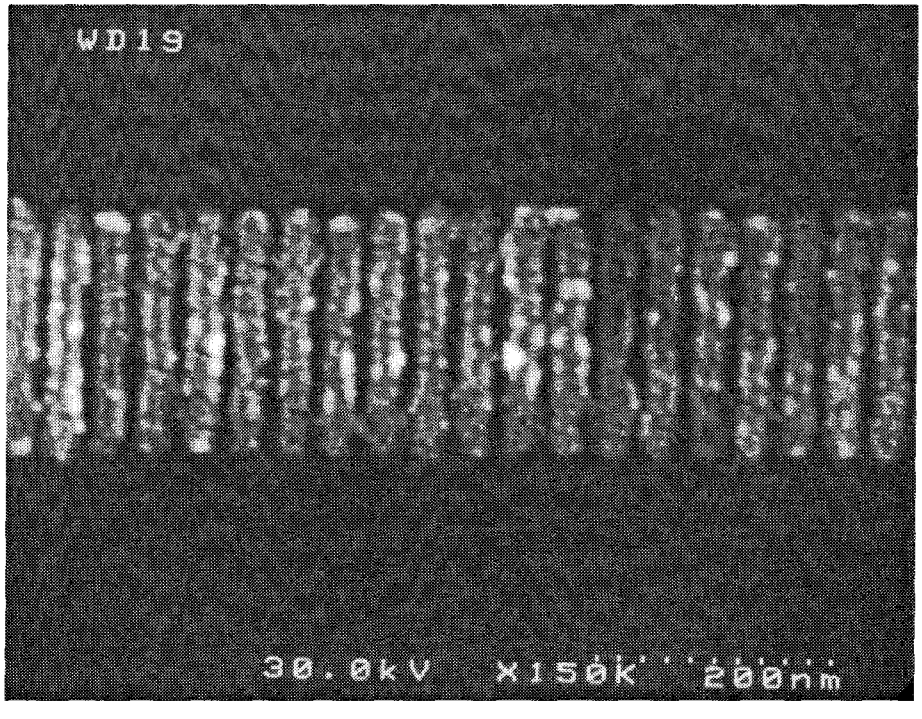

Figure 2.6: SEM image of 40nm pitch AuPd bars by lift-off on GaAs

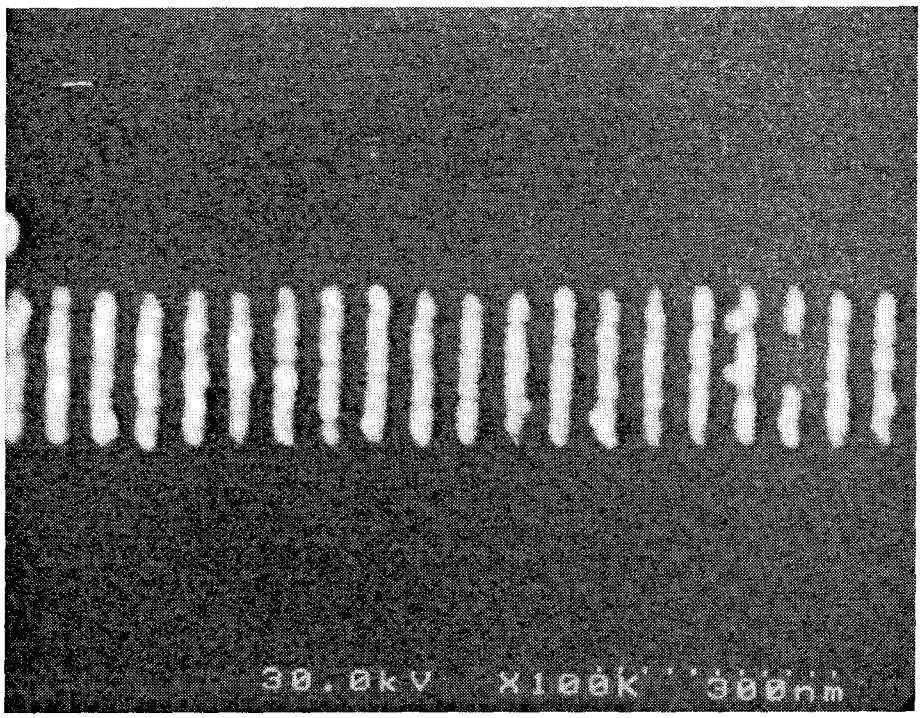

Figure 2.7: SEM image of 20nm wide Au bars with 40nm pitch by lift-off on GaAs

high density nanostructures, we can optimize the exposure dose and development conditions. The uniformity of the array is expected to improve when a stable and low noise electron beam is available. Alignment mark detection procedure is presently being developed to increase the overlaid accuracy for continuous pattern generation such as distribution feedback gratings and long waveguide structures.

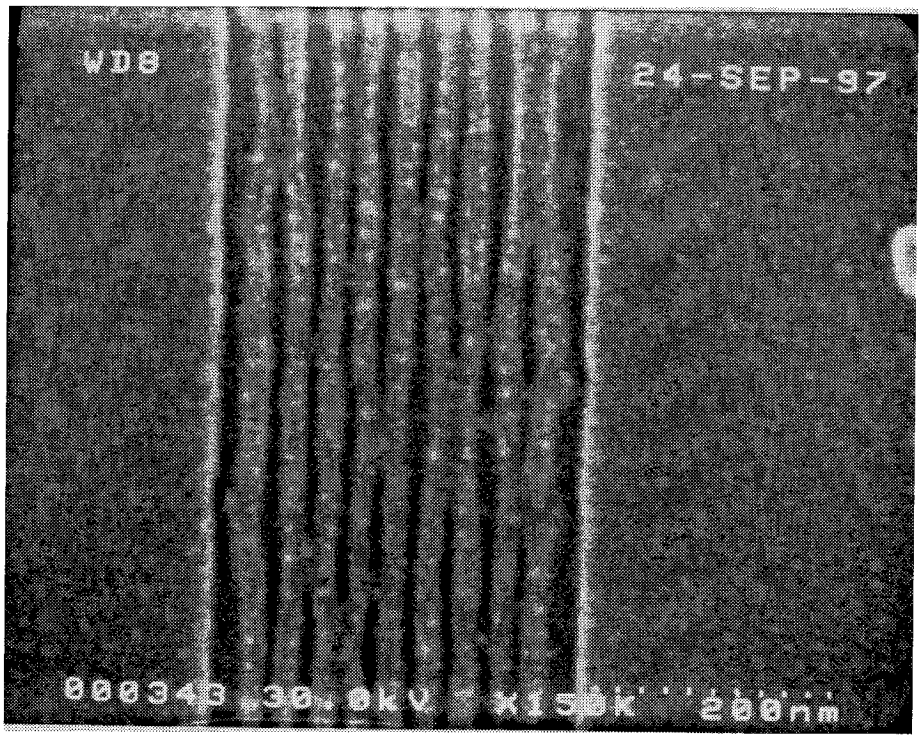

Figure 2.8: SEM image of nanogratings without prebaked procedure showing the resist adhesion problem

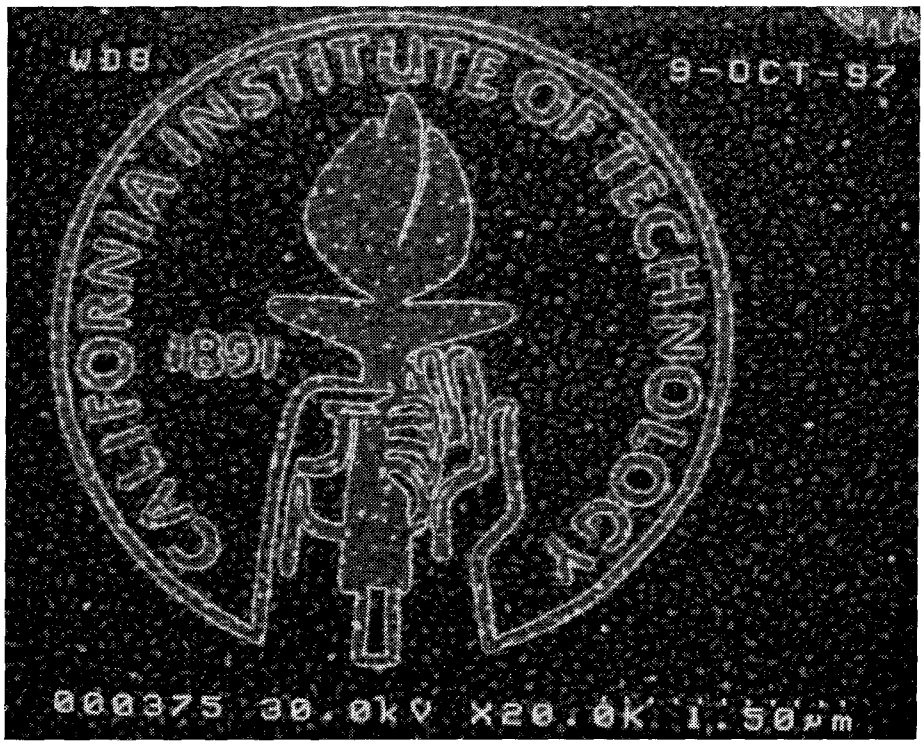

Figure 2.9: SEM image of a Caltech Logo with 3μm diameter

Part II

Form-birefringent nanostructures and micropolarizers

Chapter 3 Introduction and motivation

Propagation of electromagnetic waves in periodic dielectric structures exhibits some interesting and useful phenomena such as diffraction of light, forbidden bandgaps and so on. These effects are employed in wide applications such as diffraction gratings, holograms, distributed feedback (DFB) lasers, high reflectance Bragg mirrors, and form-birefringent gratings [24]. Polarization selective elements are widely used in diffraction optics, storage and image processing. It is now possible to produce artificial periodic nanostructures which show better polarization selectivity than natural materials because of their high dielectric constant and flexibility in design and fabrication. With advanced fabrication technologies, these nanostructures are obtained with precise dimensions.

Two substrate form-birefringent structures have been demonstrated in the past [25]. These structures are made with larger dimensions and complicated fabrication processes. Here we present the fabrication and design methods using a single substrate high spatial frequency (HSF) gratings as form-birefringent structures. The good agreements between fabricated sample measurements and simulation results are also shown. One of the most important advantages of making the period of these microstructures smaller than the wavelength of light is that these elements will have only zero-order effects in the far field pattern.

In the beginning of this task, we fabricate form-birefringence nanostructures to test the simulation program defined by effective medium theory (EMT) and rigorous coupled wave analysis (RCWA) and optimize the fabrication capability. High resolution electron beam lithography and anisotropic ion beam etching are used in the fabrication process. We have found that these artificial gratings exhibit better form-birefringence than the naturally birefringent materials and show good agreement with theoretical results [26]. The 180 degree change in phase gives us a starting point in the design of phase retardation plate. Next, we try to design a polarization selective

diffractive element using similar techniques. We also observe high selection efficiency (275:1) for transmitted TE and TM modes at first order [27]. The first micropolarizers based on 2D periodic structures are then modeled by rigorous coupled wave analysis. High extinction ratios (as large as 820:1) between transmitted TM and TE modes are demonstrated. The great advantage of this structure is its simple design and manufacture capability. In this part of thesis, the fabrication techniques and measurement results for in-plane form-birefringent microstructures are presented.

Chapter 4 Form-birefringent nanostructures

4.1 Form-birefringence effect

When orthogonal polarized light, in which one polarization is parallel to the groove (TE mode) and the other is perpendicular to the groove (TM mode), propagates through surface relief gratings, the two polarizations will experience different dielectric constants. Therefore, these two orthogonal polarizations of light have different phase shifts when passing through the grating. The phase difference between these two polarized modes can be carefully designed to yield a large birefringence effect. The advantage of using artificial-birefringence nanostructures is that the far field of the transmitted radiation pattern will possess only zero-order diffraction when the period of such microstructures is much less than the wavelength of the incident optical field. A detailed analysis can be obtained by effective medium theory (EMT) and even more precisely by the rigorous coupled wave analysis (RCWA). We use EMT to predict the initial guess and use RCWA to calculate the results. Here, we briefly discuss these two approaches.

4.2 Simulation and design

4.2.1 Effective medium theory

The effective medium theory treats the grating as a uniform layer with the same thickness but different dielectric constants for the TE mode (i.e., the electric field is parallel to the groove) and the TM mode (i.e., the electric field is normal to the groove) (see Figure 4.1) [28]. The gratings can be divided into thin layers with different

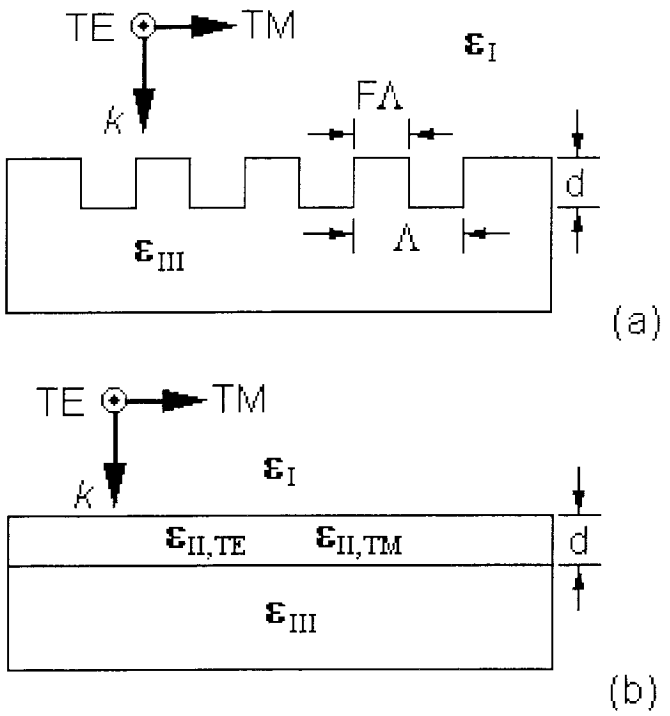

Figure 4.1: Effective medium theory for grating

dielectric constants. The properties of the single or multiple layers replacing the grating region are obtained by using methods of wave propagation in stratified media. When a grating has a small period (i.e., $\Lambda/\lambda \ll 1$) compared with the wavelength of the incident light, the higher order terms of diffraction are evanescent and only the zero-order can propagate. The EMT is not valid when $\Lambda/\lambda \sim 1/(\sqrt{\varepsilon_1} + \sqrt{\varepsilon_2})$. Here, we use second order EMT to simulate the performance of the devices. The dielectric constants for both TE and TM modes can be evaluated by the second order EMT,

$$\varepsilon_{2,TE} = \varepsilon_{0,TE} + \frac{1}{3}(\frac{\Lambda}{\lambda})^2\pi^2F^2(1-F)^2(\varepsilon_3-\varepsilon_1)^2, \tag{4.1}$$

$$\varepsilon_{2,TM} = \varepsilon_{0,TM} + \frac{1}{3}(\frac{\Lambda}{\lambda})^2\pi^2F^2(1-F)^2(\frac{1}{\varepsilon_3}-\frac{1}{\varepsilon_1})^2\varepsilon_{0,TM}^3\varepsilon_{0,TE} \tag{4.2}$$

where $\varepsilon_{0,TE}$ and $\varepsilon_{0,TM}$ are zero-order EMT

$$\varepsilon_{0,TE} = F\varepsilon_3 + (1-F)\varepsilon_1, \tag{4.3}$$

$$\varepsilon_{0,TM} = \frac{\varepsilon_3\varepsilon_1}{F\varepsilon_1 + (1-F)\varepsilon_3} \tag{4.4}$$

The EMT is only valid when analyzing structures with small period to wavelength ratios. Under this assumption, the EMT can precisely calculate the reflectance of the structure but can not calculate the phase information of the two TE and TM modes [29]. In order to get more precise information about diffraction, the rigorous coupled wave analysis is used.

4.2.2 Rigorous coupled wave analysis

The rigorous coupled wave theory has been developed to analyze the diffraction of a dielectric surface-relief grating [2, 30, 31, 29, 32]. The analysis applies to more general cases such as arbitrary gratings profiles, groove depths, angles of incidence, and the wavelengths. In the beginning, an arbitrary shape of dielectric surface-relief grating is divided into a large number of thin slices (see Figure 4.2). The case of lossless dielectrics and TE mode is treated for simplicity. The total electric field in region I is the sum of the incident and the backward-traveling waves. The total electric field in region III is the sum of the transmitted waves. We have

$$E_1 = exp(-j\vec{k_1}\cdot\vec{r}) + \sum_i R_i exp(-j\vec{k_{1i}}\cdot\vec{r}), \tag{4.5}$$

$$E_3 = \sum_i T_i exp(-j\vec{k_{3i}}\cdot(\vec{r} - d\hat{z})) \tag{4.6}$$

where $j = (-i)^{1/2}$, $\vec{k_1} = 2\pi(\epsilon_I)^{1/2}/\lambda$, $\vec{k_3} = 2\pi(\epsilon_{III})^{1/2}/\lambda$.
R_i is the normalized amplitude of the ith reflected wave and T_i is the normalized amplitude of the ith transmitted wave.

In each thin layer of region II, the optical fields are formulated in terms of spatial harmonics by Fourier series expansions of the dielectric constant. The effective dielec-

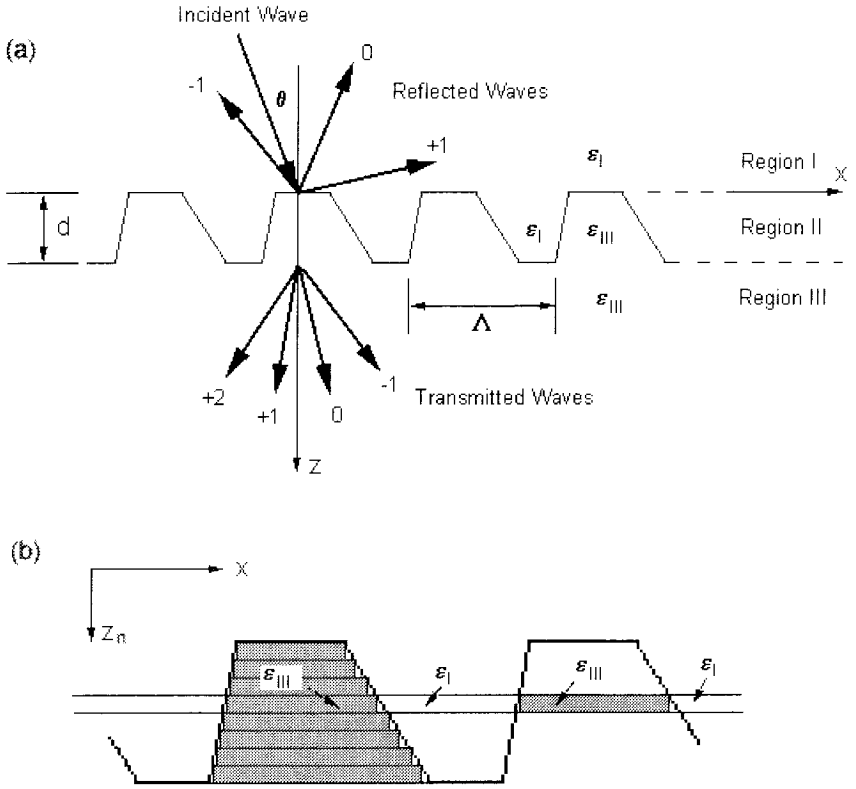

Figure 4.2: Rigorous coupled wave analysis for dielectric surface relief gratings. (a) the geometry of the grating and both forward-diffracted and backward-diffracted waves (b) the planar grating slab resulting from the decomposition of the grating into N thin gratings, after M. G. Moharam *etal.* 1982 [2]

tric constant of each layer is calculated as a volume-weight average of the dielectric constants of the incident and the substrate regions.

$$\epsilon_n(x, z_n) = \epsilon_I + (\epsilon_{III} - \epsilon_I) \sum_h \varepsilon_{h,n} exp(jhKx), \tag{4.7}$$

$$E_{2,n} = \sum_i S_{i,n}(z) exp(-j(\vec{k_{2,n}} - iK) \cdot \vec{r}) \tag{4.8}$$

where $K = 2\pi/\Lambda$ is the magnitude of the grating vector and $\varepsilon_{h,n}$ are the normalized complex harmonic amplitude coefficient. $S_{i,n}(z)$ are the space-harmonic field amplitude. $\vec{k_3} = 2\pi(\epsilon_{0,n})^{1/2}/\lambda$, $\epsilon_{0,n}$ is the average relative dielectric constant for the nth slab grating. Each ith diffracted field in different regions must phase matched.

When we substitute the wave equation with the components of these spatial harmonics, a sequence of coupled first-order linear differential equations are generated. The equations can be solved in terms of their eigensolutions [30]. The field distribution in each layer of the grating can be represented by the superposition of these eigensolutions. Transmission and reflection diffraction fields can then be derived by a match of the appropriate boundary conditions. Subsequently, diffraction efficiencies are calculated for the propagating transmitted and reflected diffraction orders. Energy conservation is used as a criterion for the convergence of numeric solutions [2]. We design and construct the period of the surface-relief grating smaller than the wavelength of light; therefore, only the zero and the lowest orders are propagated and calculated through the gratings.

4.3 Results

4.3.1 Fabrication

Fabrication of these artificial birefringence nanostructures in the near-infrared range requires high resolution lithography and anisotropic etching [33]. Figure 4.3 shows the fabrication procedure. High refractive index contrast ratios can be obtained by choosing a high refractive index GaAs substrate. First, a GaAs wafer is coated with a

layer of SiO_2, then a layer of Au and finally a layer of high molecular weight PMMA. Electron beam lithography with 30kV incident beam energy is used to define the high resolution gratings over a square area of $100\mu m \times 100\mu m$ on 70nm thick resist layer. The PMMA pattern is then developed for 14 sec in 3:7 cellusive : methanol and transferred into Au layer by Ar ion milling. This Au layer serves as a mask in reactive ion etching. During the etching, 60mtorr C_2F_6 serves as a reactive gas, and a 300V bias voltage is applied to obtain an etching rate of 20nm/min. Then chemically assisted ion beam etching is used to etch the high resolution grating to the desired depth in GaAs by Ar ion assisted with Cl_2 reactive gas. Finally we remove the SiO_2 mask by a HF wet etch. The structure is then examined in a scanning electron microscope to determine the period and the profile. Figure 4.4 and 4.5 show the SEM images of top view and cross sectional view of the artificial birefringence nanostructures. The grating period is 200nm and the etching depth is 490nm, respectively. The SEM image of the cross section view shows the triangular profile of the nanostructures. Mask erosion during the ion beam etching results in the triangular profile instead of rectangular shape.

4.3.2 Measurement and comparison

The optical characterization measurement system is shown schematically in Figure 4.6. An Ar^+-pumped Ti:Sapphire laser is operated at a wavelength of 920nm, where GaAs is transparent with minimum absorption. The polarization of the laser beam is controlled by a polarization rotator so that the normally incident optical wave is polarized linearly at 45° with respect to the grooves' direction. The incident beam is focused onto the pattern by a microscope objective. These high spatial frequency gratings allow only zero-order in the far field pattern. At a distance of 100cm from the sample, an aperture and a polarization analyzer are introduced followed by a photodetector. Figure 4.7 shows a typical curve of measured and calculated intensity vs. the orientation angle of the analyzer. The cross and diamond marks correspond to the measurements of GaAs substrate with and without nanostructures, respectively. The

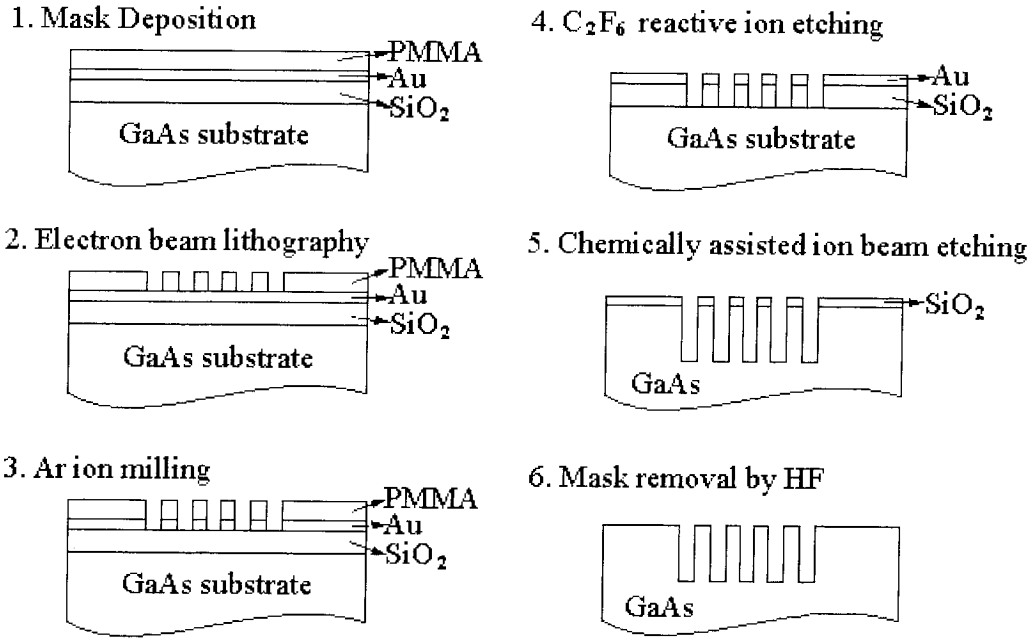

Figure 4.3: Fabrication procedure of form-birefringent nanostructures

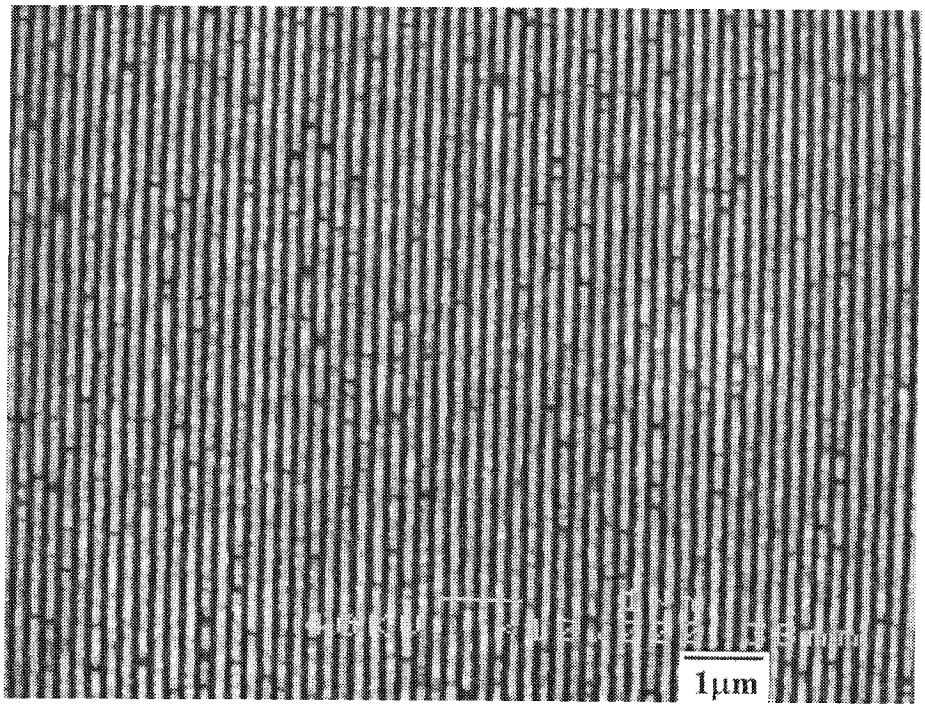

Figure 4.4: SEM image of top view of form-birefringent nanostructure: the period Λ is 200nm and the fill factor F is 0.5

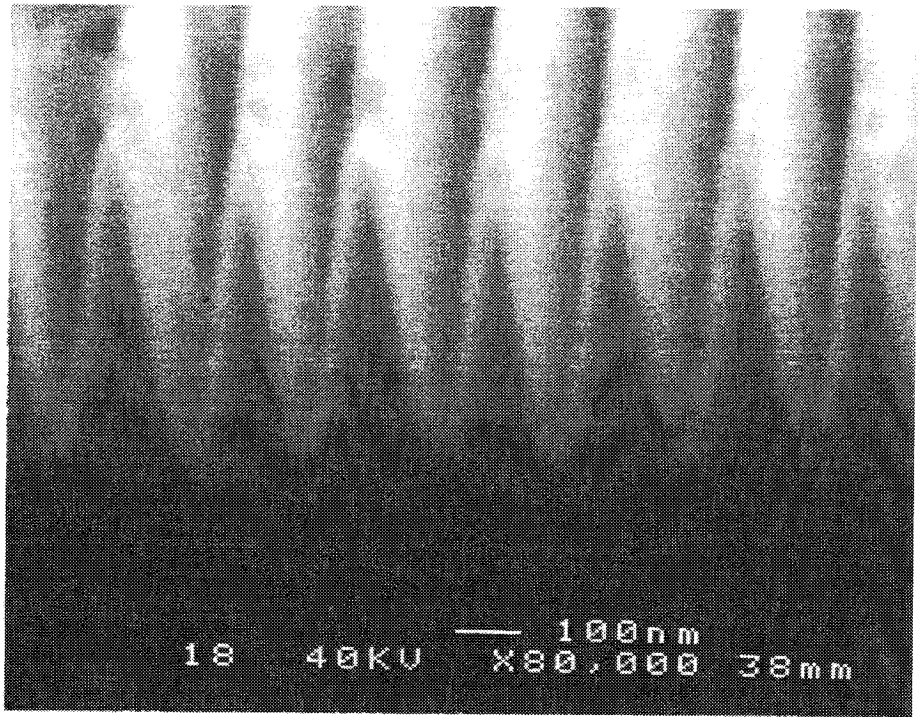

Figure 4.5: SEM image of cross section view of form-birefringent nanostructure: the triangular profile is due to the mask erosion

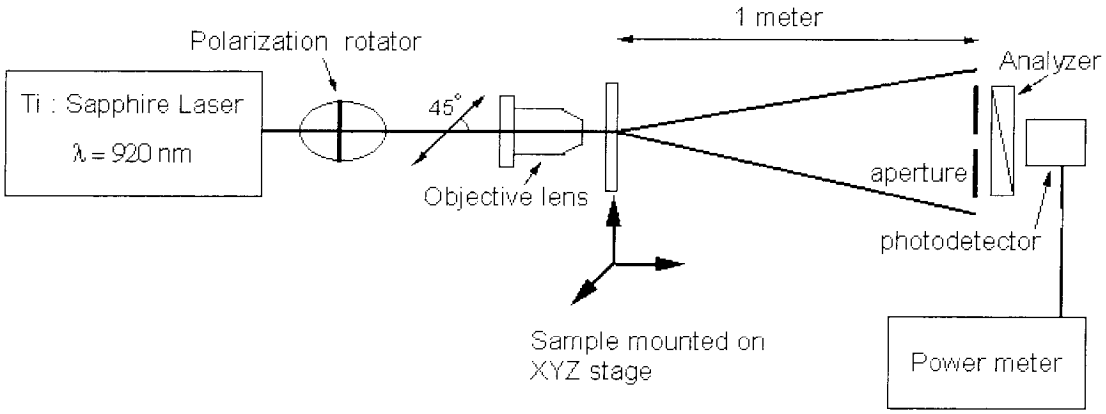

Figure 4.6: Measurement setup for form-birefringent nanostructures

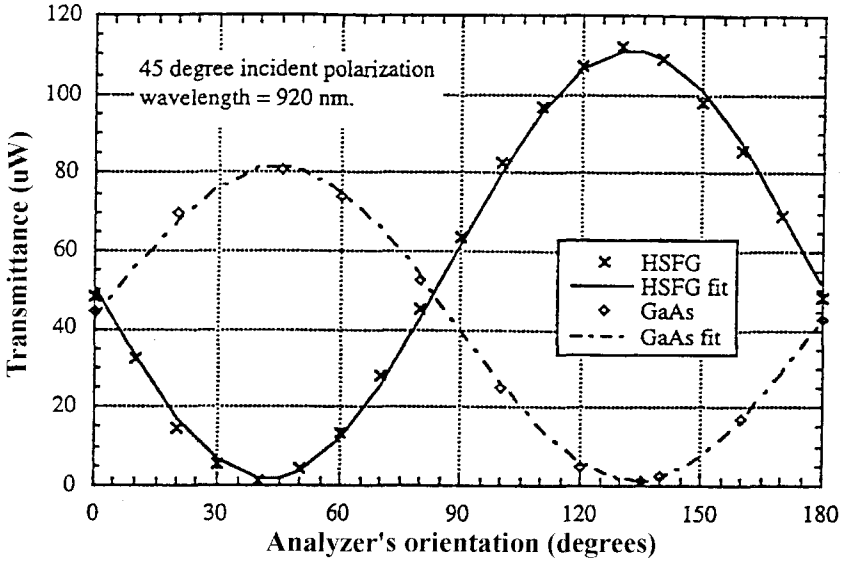

Figure 4.7: Measured intensity vs. the orientation angle for form-birefringent nanostructures

solid and dotted lines are calculated results by RCWA. We found that the measured and calculated results agree very well and the related phase shift between TE and TM modes is 162 degrees. The large phase shift between two orthogonal polarizations when passing through these artificial form-birefringent nanostructures enables us to design polarization selective elements and binary phase array for data storage [26].

4.4 Polarization selective computer generated holograms

We have shown the techniques to design and to fabricate form-birefringent nanostructures to generate 180 degree phase shifts. Polarization selective elements such as holograms are more attractive. We use the similar design to generate high spatial frequency gratings (HSFG) as polarization-selective computer-generated holograms [25, 27]. Figure 4.8 and Figure 4.9 show the design and the SEM image of the structures. The period of the binary phase diffractive grating, T, is 10μm. The

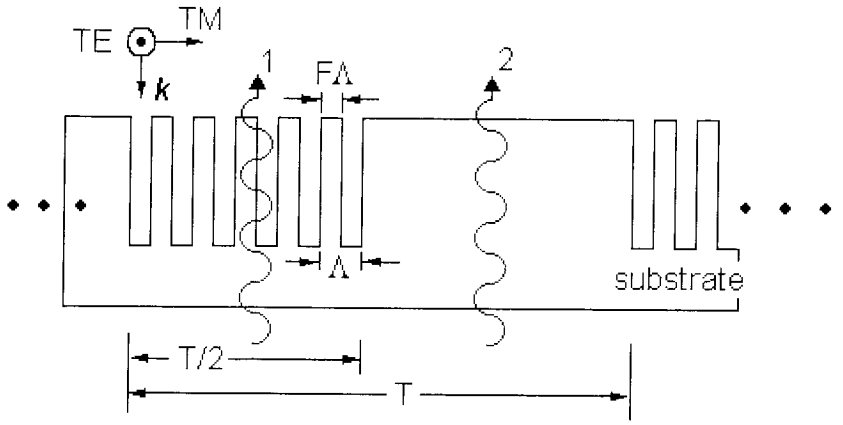

Figure 4.8: Design of polarization selective CGH structure

Table 4.1: Polarization contrast ratio comparison table

Performance	0th Order	1st Order	-1st Order
TE efficiency	0.86%(0.0%)	41.4%(40.5%)	44.2%(40.5%)
TM efficiency	75.5%(100%)	0.15%(0%)	0.44%(0%)
Polarization contrast ratio	88.2:1	275:1	99.2:1

period of HSFG, Λ is 0.3μm, and the fill factor of the HSFG F is 0.35. The depth of the fabricated element is 0.75μm. The setup for optical measurement is shown in Figure 4.10. We use a He-Ne laser operating at 1.523μm. A Ge detector is used to measure the far-field diffraction patterns. The measured diffraction efficiency excluding reflection, and the polarization contrast ratios, are summarized in Table 4.1 [27].

Those two form-birefringent nanostructures are designed by using EMT and verified to be effective in the rigorous coupled wave analysis. The design and the fabricated devices are found to be in good agreement. The device shows a large polarization contrast ratio (as large as 275:1) and high diffraction efficiencies (>40% for the first diffraction orders). Such form-birefringent computer generated holograms (FBCGH) are expected to be useful in fabrication of compact and efficient free space transparent photonic switching fabrics as well as for packaging optoelectronic devices.

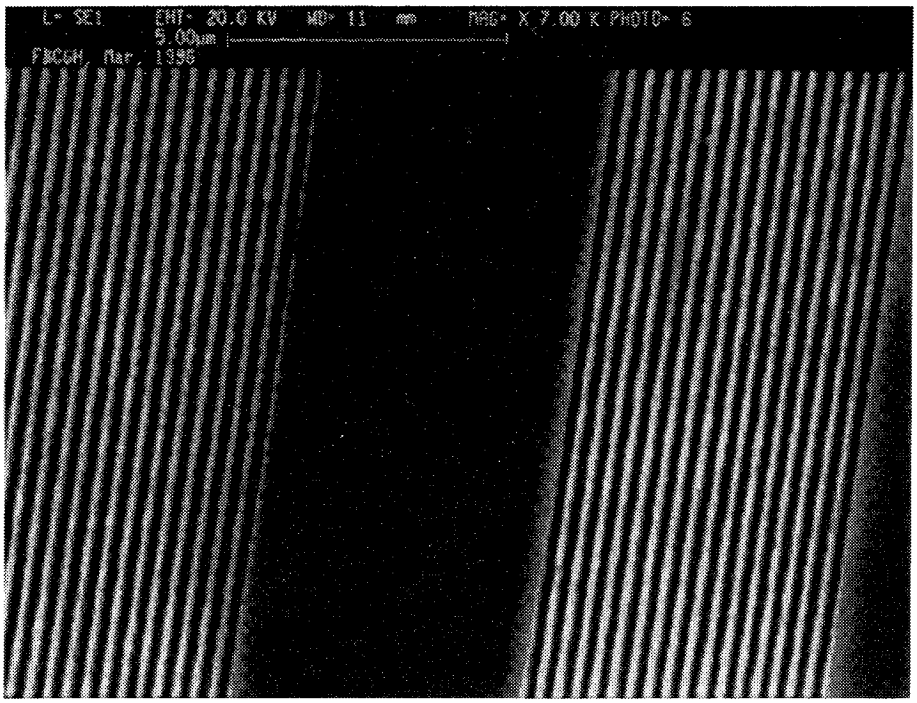

Figure 4.9: SEM image of a polarization selective CGH structure

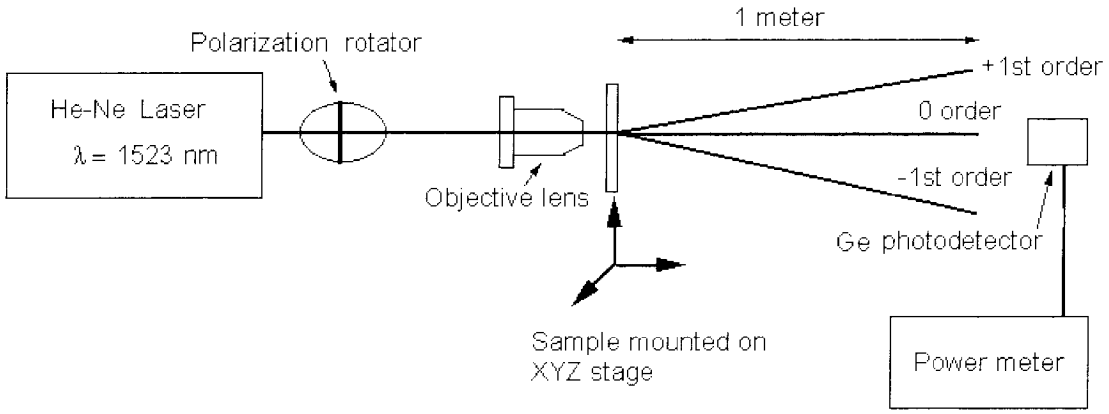

Figure 4.10: Measurement setup for polarization selective CGH

4.5 Discussion

We have shown our design tools and fabrication techniques to construct high spatial frequency gratings for polarization selective elements. The single-substrate form-birefringent nanostructures exhibit larger form-birefringence effect than natural crystals and simplify the fabrication procedure. We have demonstrated that large polarization contrast ratio ($>$ 275:1) and high diffraction efficiencies ($>$40%) for the first diffraction orders are achieved by using polarization selective computer generated holograms.

Chapter 5 Micropolarizer

5.1 Introduction and motivation

The idea of using two-dimensional photonic crystals in optical devices has been studied for years. Details of structure design and experimental approaches have been presented by many groups [34, 35, 36, 37]. Typically, drilling a set of holes straight into a semiconductor forms a 2D photonic crystal. For a good performance of the photonic crystal, the 2D structures must have a high aspect ratio in the Z-direction normal to the incident plane. The technology for building such geometries requires highly anisotropic etching of very small structures. The depth of these etched features can be decreased by placing a waveguide structure perpendicular to the 2D plane to reduce light scattering. These 2D photonic crystals are useful in high reflectivity mirrors or small resonant cavities. Recently, passive elements like polarizers have also become very attractive. Therefore, 2D photonic crystals with different purposes are explored. These 2D dielectric crystals have a wider spectral range and larger angle tolerance compared with 1D Fabry-Perot cavities.

Here we introduce a novel polarizing beam splitter based on 2D periodic structures that uses the anisotropic spectral reflectivity (ASR) characteristic of a high spatial frequency multilayer binary grating. Such ASR effects allow us to design an optical element that is transparent for TM polarization and reflecting for TE polarization. These polarization selective mirrors are a novel application for 2D photonic crystals. Compared with conventional two-dimensional photonic crystals, these structures have several advantages. Figure 5.1 shows the difference in fabrication schemes between these two 2D photonic crystals. One big advantage is that the geometry of the multilayer binary grating structures allows easy fabrication of high aspect ratio 2D photonic crystals which are quasi-infinite in length.

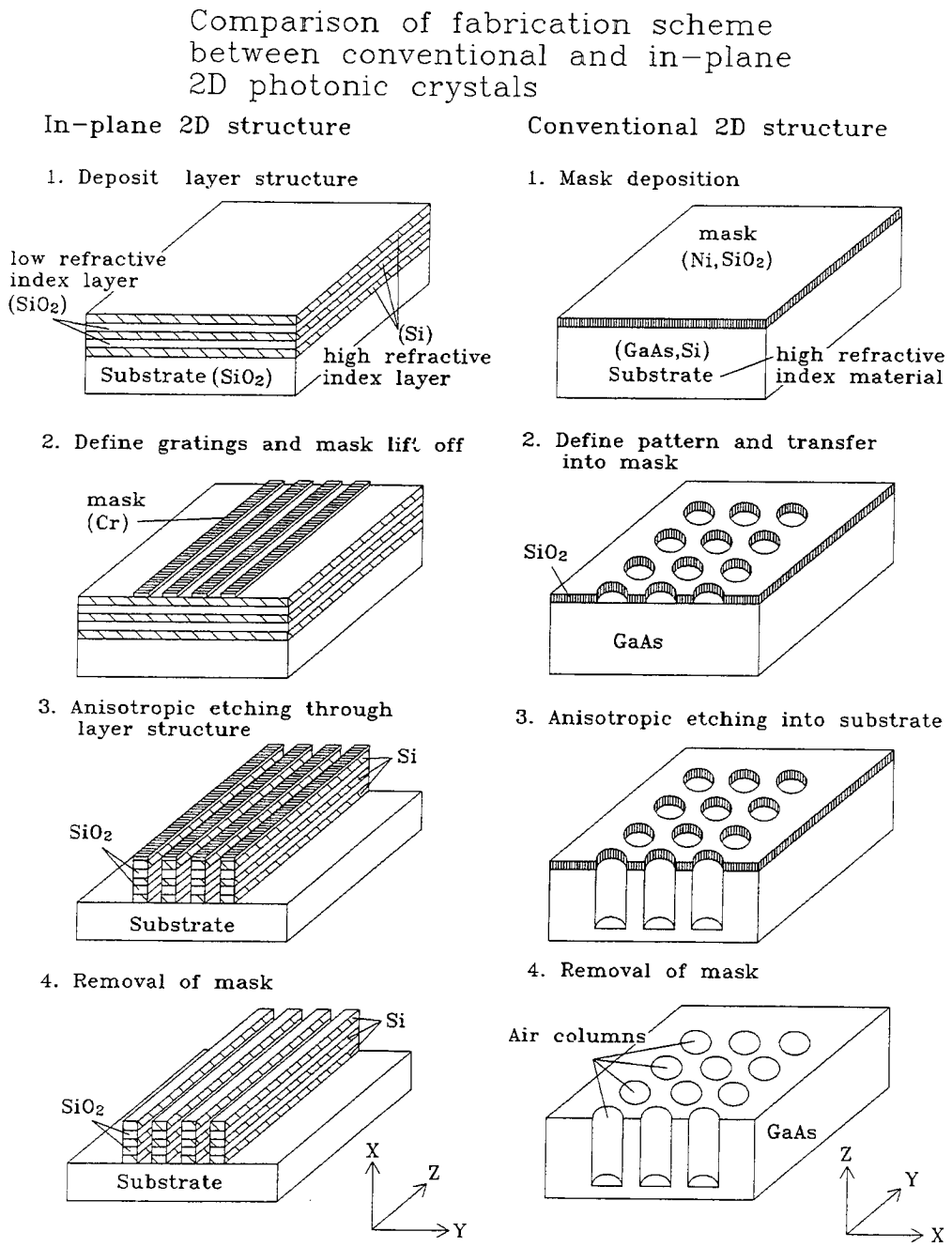

Figure 5.1: Comparison of fabrication and geometry between two 2D photonic crystals

5.2 Design

The design of these 2D photonic crystals starts from form-birefringent nanostructures. The calculated reflectivity for both TE and TM modes through Si/SiO_2 multilayer structures are shown in Figure 5.2. The designed dimensions of these Si/SiO_2 multilayers are 130nm/260nm, respectively. A 42 degree incident angle is chosen to separate the incident and reflected light. An angular incidence which increases optical path and reflectivity when passing through these multilayers can be used to reduce the number of layers. The high refractive index layers placed on the top and the bottom of the structures also increases the reflectivity [38]. The wide band spectrum and the large angular spectrum come from the nature of 2D periodic structures. Comparable optical properties can not be obtained by natural crystals or simple gratings.

5.3 Results

5.3.1 Fabrication procedure

The fabrication procedure is shown in Figure 5.3. Instead of single layer substrate high spatial frequency (HSF) binary gratings, we fabricate multilayer HSF binary gratings. First, five Si/SiO_2 alternate layers with 130nm/260nm, respectively, are deposited by reactive RF sputtering on the top of a glass slide. The two layers of PMMA resist are used to improve lift-off quality. Next, 30kV electron beam lithography defines a grating with 300nm lines and a 600nm period on the 200nm PMMA layer. This PMMA layer then works as a template to lift-off 80nm chromium. The Cr layer in turn is the etch mask during reactive ion etching. The Si and SiO_2 layers are anisotropically etched by using C_2F_6 at etch rate of 20nm/min and mixture of CCl_2F_2 and NF_3 at etch rate of 100nm/min in a reactive ion etcher (RIE), respectively. The layers are over etched to make the bottom of each layer clean. Finally, the remaining Cr mask is removed by a wet etch. In this way, a high quality photonic crystal with 600nm period and 0.9μm depth is constructed [39]. Figure 5.4 shows the SEM image of this Si/SiO_2 multilayer structure. The roughness is due to mask erosion during the long

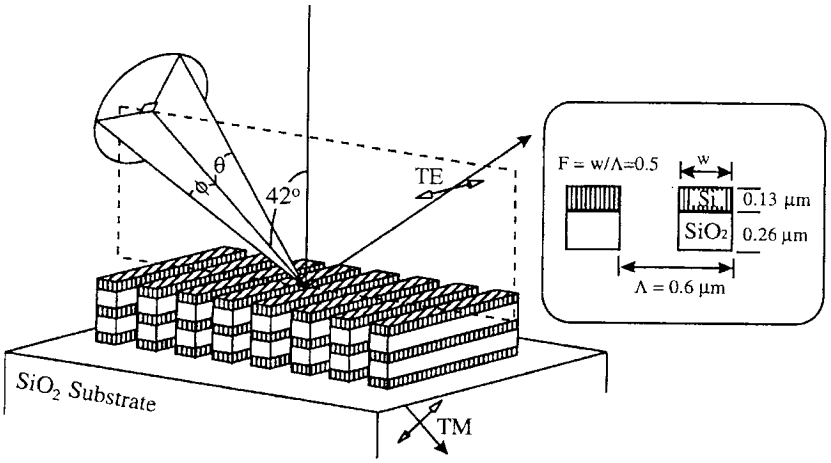

(a)

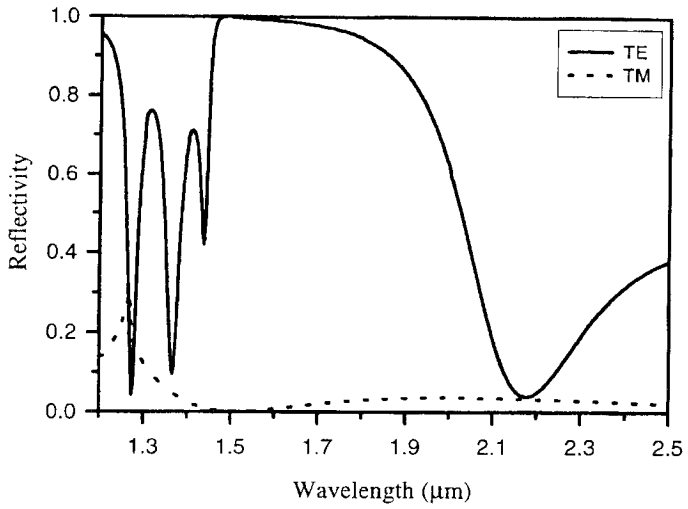

Figure 5.2: Calculated reflectivity for both TE and TM modes as a function of wavelength for a micropolarizer show high extinction ratio at 1.5μm, which light incidents at 42 degree to the normal and the designed thickness for Si/SiO_2 are 130nm/260nm, respectively

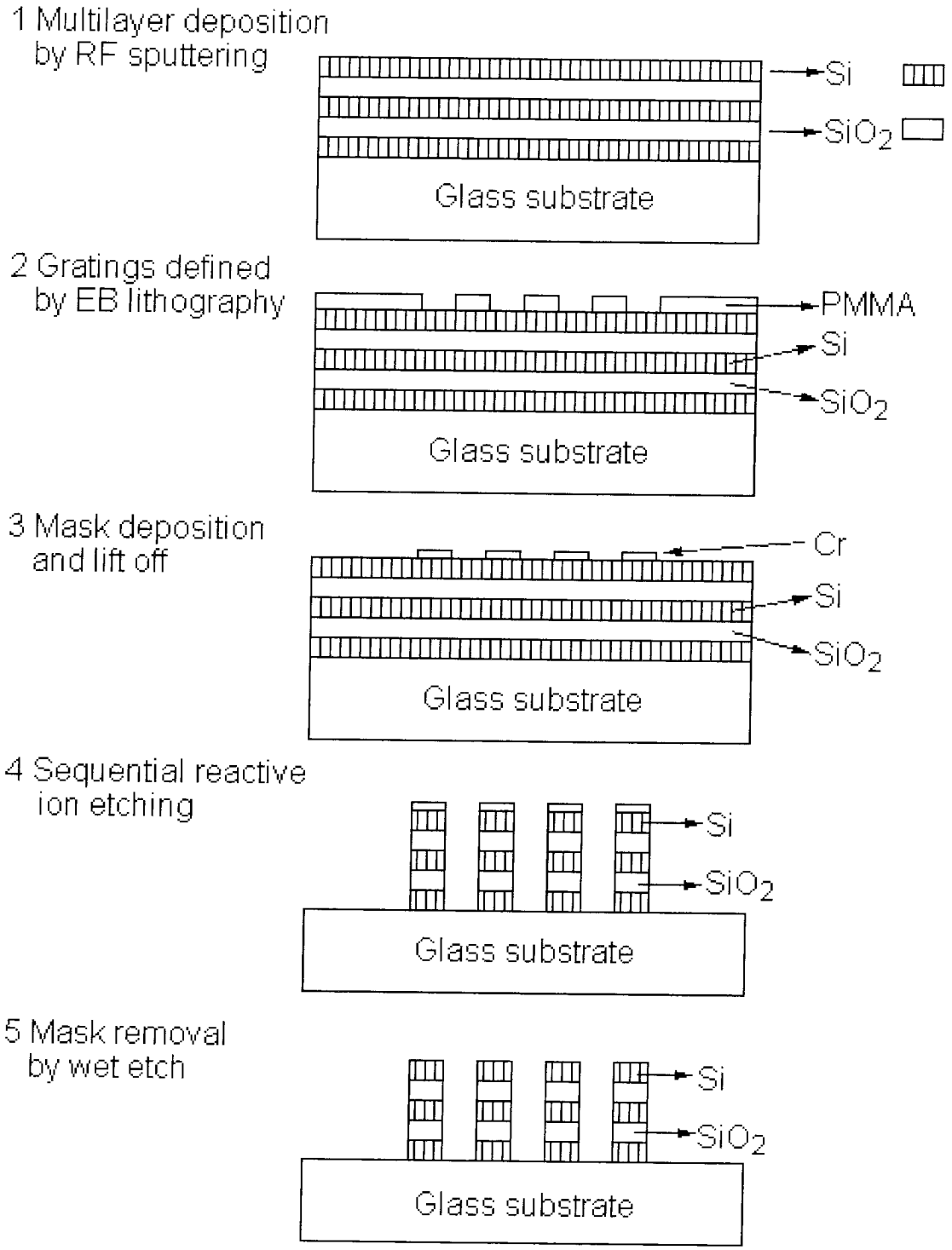

Figure 5.3: Fabrication procedure of 2D micropolarizer

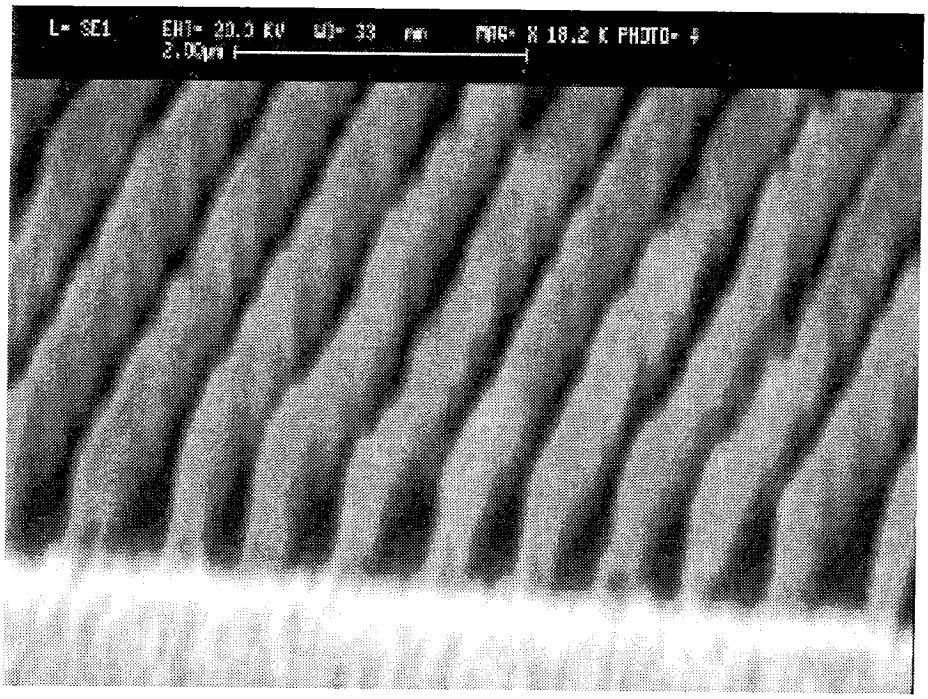

Figure 5.4: SEM image of Si/SiO_2 multilayer structures. The roughness is caused by the mask erosion

sequential reactive ion etching procedure.

5.3.2 Measurement and comparison

The optical characterization is shown schematically in Figure 5.5. A He-Ne laser at 1.523μm passes through a polarization rotator to select the desired polarization. This polarized light is then focused on the sample mounted on a rotation stage. A visible He-Ne laser is used to help focus on the pattern. This polarizing beam splitter is characterized by measuring both the transmitted and reflected power of TE and TM modes for different incident angles. Then the results were compared with the numerical simulation results obtained by rigorous coupled-wave analysis (RCWA). Figure 5.6 shows the comparison between measurement and simulation of the 2D micropolarizer with the extinction ratio as high as 820:1 for transmission at 1.5μm. The roughness of the structure causes a significant drop of extinction ratio at the designed angle. But the broadband nature of the 2D photonic crystal really exhibits

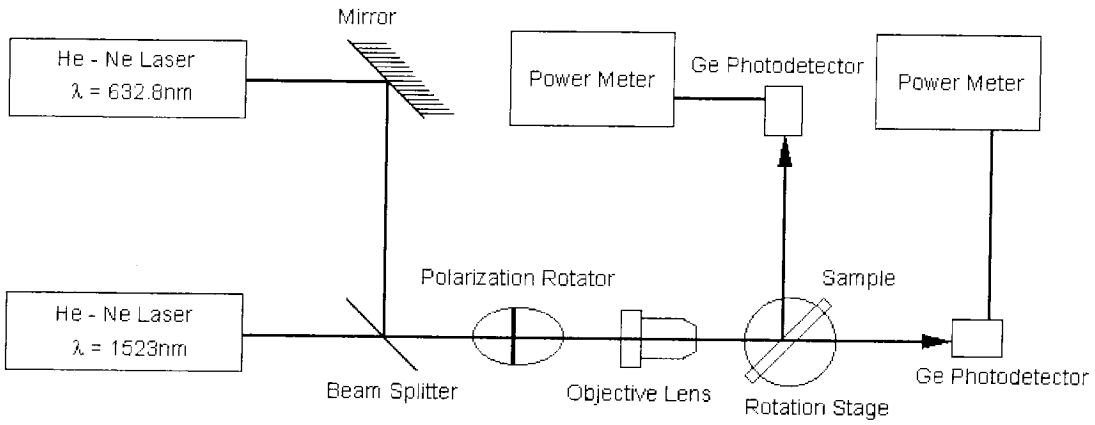

Figure 5.5: Measurement setup for 2D micropolarizer

the strong extinction ratio between transmitted TM and TE modes even with the fabrication errors. The manufacturable process and the excellent performance show the promising application of 2D photonic crystal in polarization selective elements.

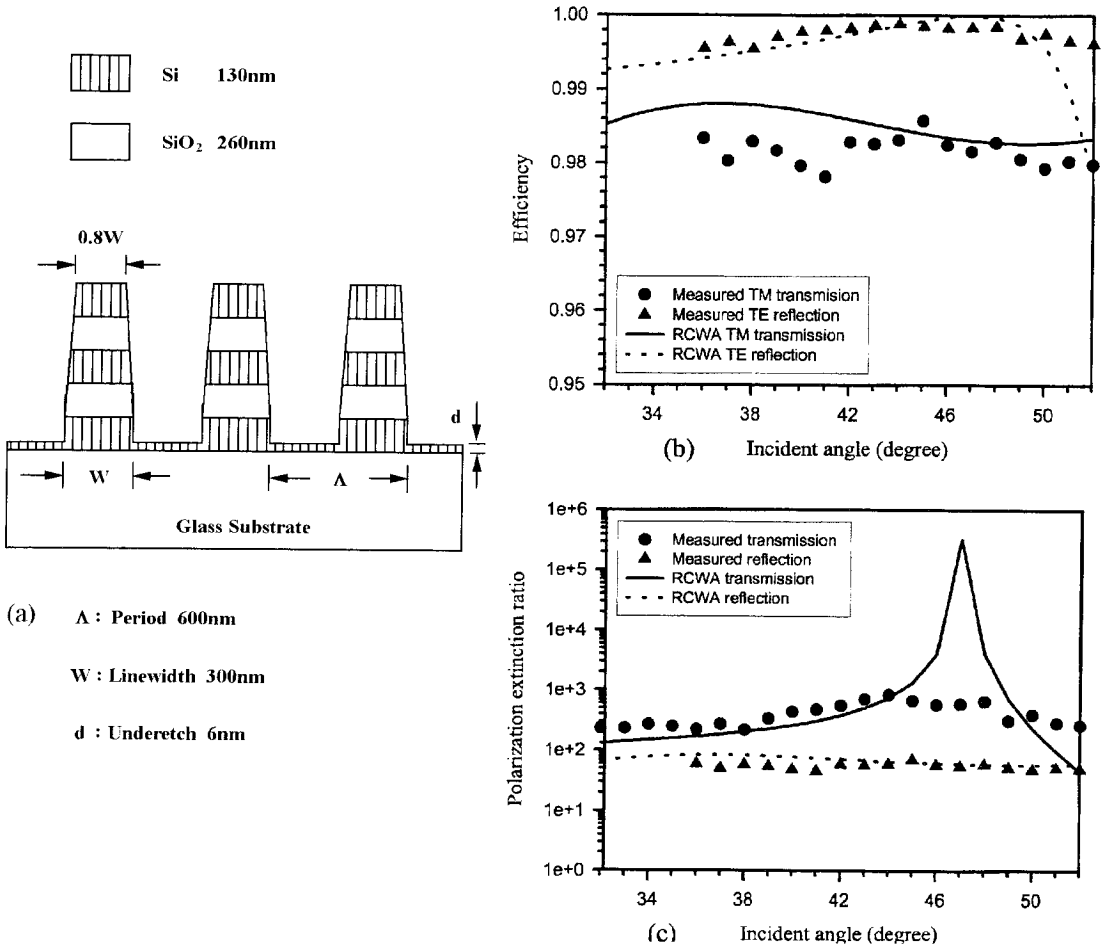

Figure 5.6: Comparison of experimental and simulation results for 2D Si/SiO_2 micropolarizer. (a) Efficiency as a function of incident angle, (b) Polarization extinction ratios as a function of incident angle for both transmitted TM modes and reflected TE modes

Chapter 6 Discussion

6.1 The next generation micropolarizers

To further simplify the fabrication process and to reduce fabrication errors, we can use the GaAs/AlAs material system to construct a polarizing beam splitter. Figure 6.1 shows the fabrication procedure. First, two and a half pair of GaAs/AlAs layers with thickness 130nm and 220nm respectively are grown by molecular beam epitaxy (MBE). Then a 200nm SiO_2 layer followed by a 50nm Au layer is deposited on the top of the wafer. 30kV electron beam lithography is conducted to define 300nm line width and 600nm period on PMMA layer. The PMMA pattern is then transferred by Ar ion milling into a Au layer. This Au mask layer is then amplified by etching into SiO_2 layer using C_2F_6 reactive ion etching. This SiO_2 layer serves as an etch mask in Ar ion beam etching assisted by reactive Cl_2 gas. The grating pattern is transferred into GaAs/AlAs layers with a depth of 1.6μm. Then steam oxidation converts AlAs layer into Al_2O_3 layer. This process will increase the contrast of the refractive-index between alternate layers. Finally, the SiO_2 mask is removed in HF [40]. Figure 6.2 and 6.3 show SEM images of this multilayer structure and a close-up view of the alternate layers. The dark lines in the picture are Al_2O_3 layers due to the low secondary electron emission and show a volume shrinkage of about 10% from AlAs to Al_2O_3. The optical characterization of this device doesn't exhibit the high extinction ratio as the Si/SiO_2 micropolarizers because the high refractive index substrate is used as a reflecting mirror. The extinction ratio can be improved by inserting a low refractive index substrate underneath the 2D micropolarizer. The simple way to accomplish this is by growing an AlAs layer underneath and converting it into Al_2O_3 as an antireflection coating.

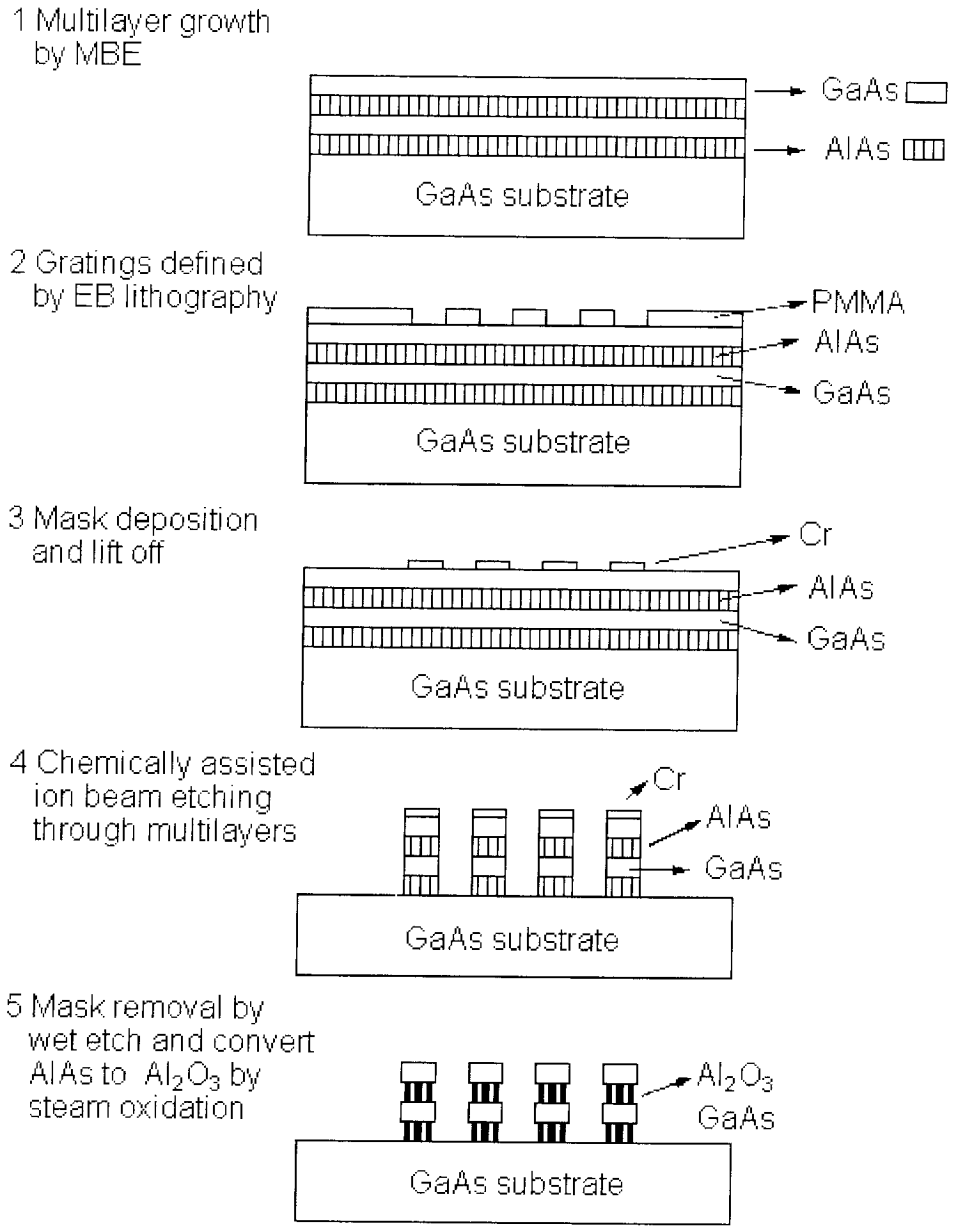

Figure 6.1: Improved process for 2D micropolarizer to reduce mask erosion during fabrication

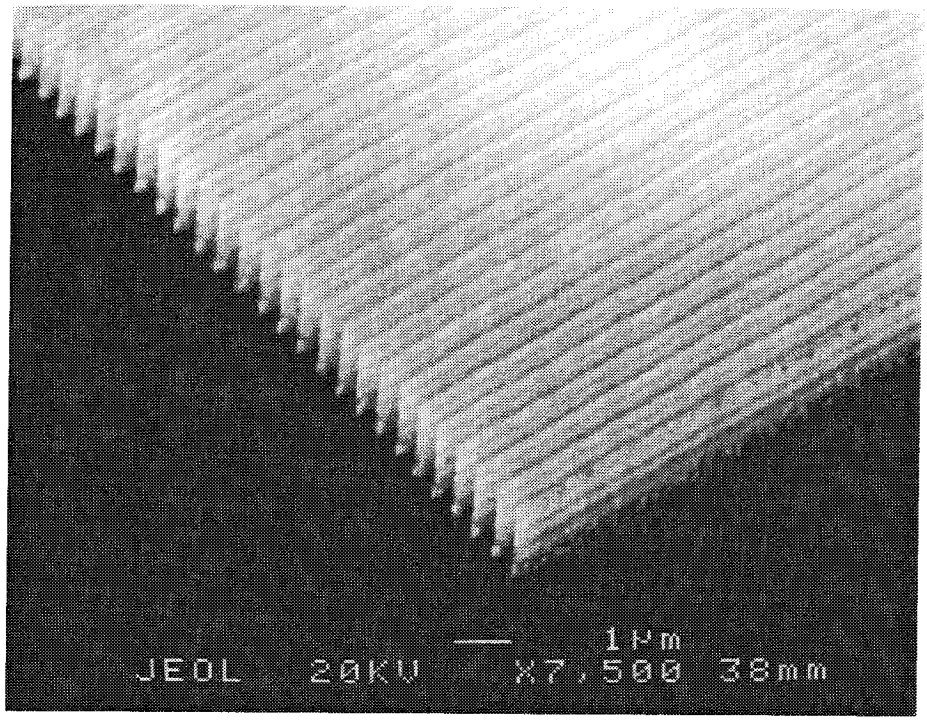

Figure 6.2: SEM image of a 2D micropolarizer with GaAs/Al_2O_3 structures

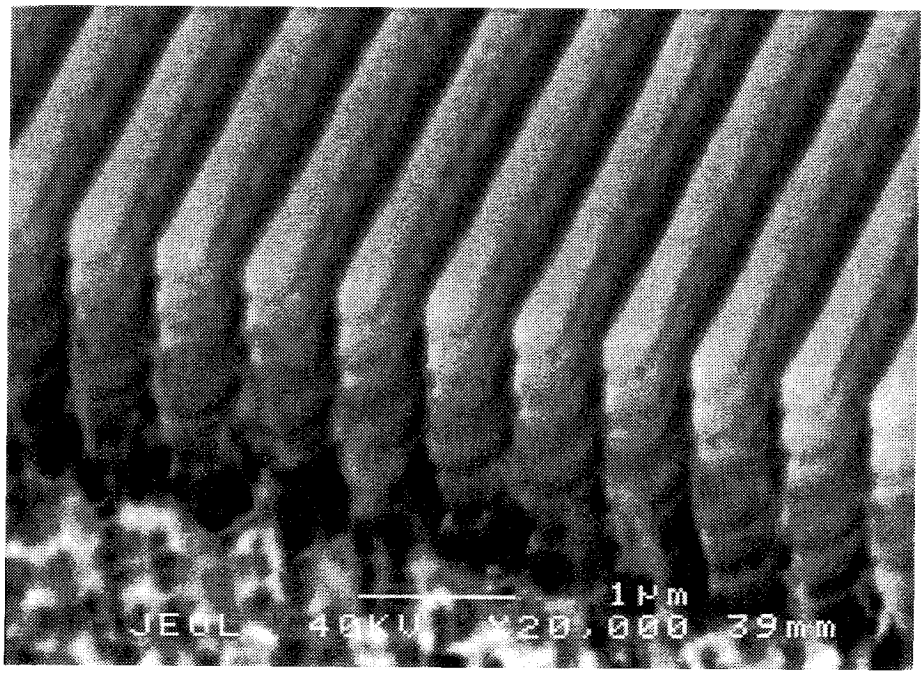

Figure 6.3: SEM image of a close view of a 2D micropolarizer; the bright layer is GaAs and the dark layer is Al_2O_3 which shows volume shrink

6.2 Design of the next generation polarization selective mirrors

We have demonstrated the micropolarizing beam splitter based on multilayer structures. One of the applications is to control the polarization of vertical cavity surface emitting lasers (VCSEL) [41, 42]. In order to amplify only one polarization of a VCSEL, a polarization selective mirror is required. Typically, an external mirror is used to control the polarization of VCSEL. Here, we propose a polarization selective mirror which can be easily fabricated and integrated with top mirrors of VCSELs. These mirrors are simply 2D photonic crystals with a square lattice. Figure 6.4 shows the fabrication scheme and calculated spectra of these mirrors. A single substrate with high refractive index is required. We define the line grating using electron beam lithography and transfer into robust mask. Next, angle anisotropic etching is performed at 45 degrees to the normal. Finally, the mask is removed by a wet chemical etch. These mirrors are predicted to show a high reflectivity ($\gg$99%) for TE mode and low reflectivity ($\approx$30%) for TM mode. A thin antireflection layer of low refractive index can be placed under the mirrors to further reduce the reflectivity of the TM mode.

6.3 Summary

We have shown that these artificial periodic nanostructures exhibit excellent form-birefringence properties. Micropolarizers based on 2D photonic crystals are demonstrated with great polarization selectivity between transmitted TE and TM modes and are the first useful and manufacturable photonic crystal structures. The simple fabrication method makes these 2D micropolarizers useful in a wide range of applications for diffraction optics. The choice of dielectric materials is made to widely tune the devices in different spectral ranges. Although looking for a complete bandgap or suppressing all the optical modes in photonic crystals has been the first goal in photonic band engineering, the physics resulting from passive photonic crystals is also

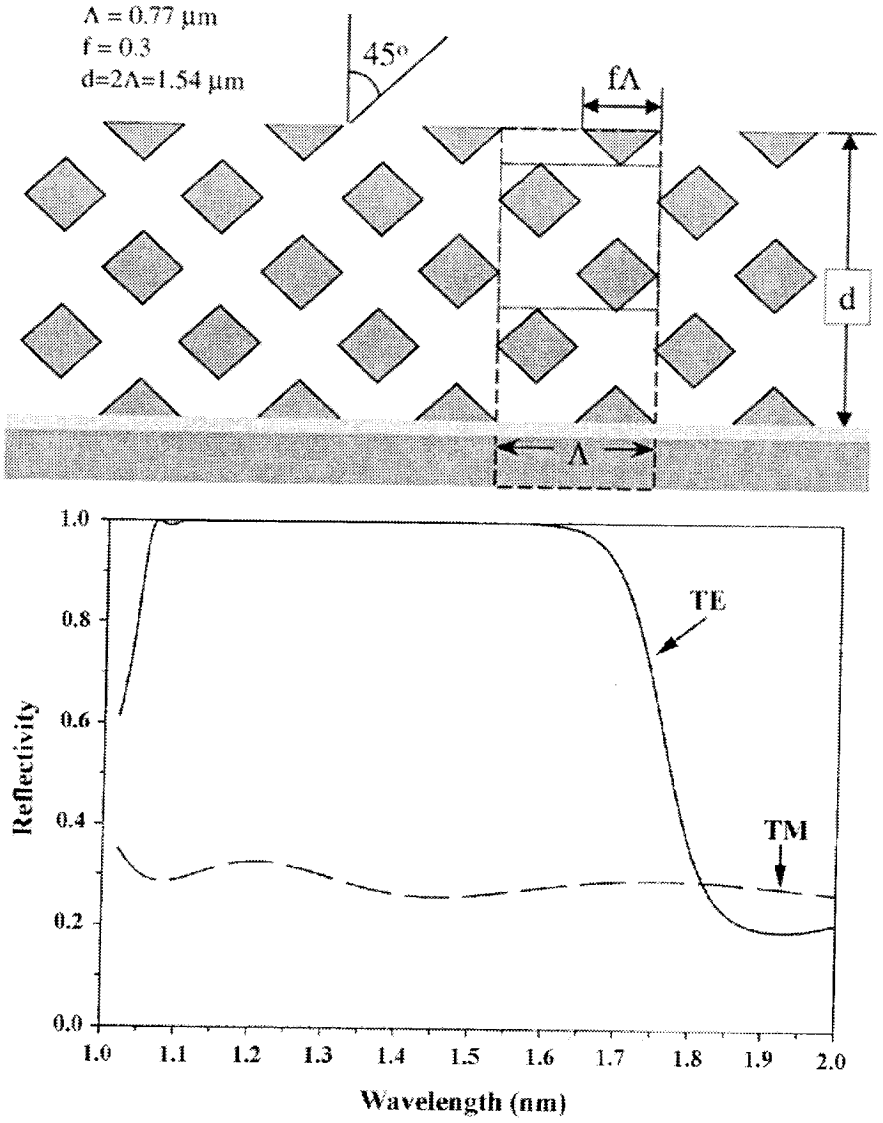

Figure 6.4: (a) Fabrication scheme of next generation polarization selective mirrors based on square lattice 2D photonic crystals. (b) Calculated efficiency of polarization selective mirrors as a function of wavelength shows larger than 99% reflectivity for TE mode and only 30% for TM mode

very interesting. Engineering and characterization of these crystals in optical devices are presently of greater immediate interests.

Part III

3D photonic crystals

Chapter 7 Introduction and motivation

7.1 Introduction

The properties of a photon can be modified in a periodic dielectric structure if the period of the structure is comparable to the wavelength of light [43, 44, 24]. In the simple one-dimensional case, dielectric Bragg mirrors exhibit a high reflectivity region or a stopband at the normal incident direction. If the structure has periodicity in all directions, a complete 3D photonic bandgap can open in all directions. To understand that new idea, it was natural for researchers to devise artificial photonic crystal structures which behave toward electromagnetic waves in the same manner as natural semiconductor crystals behave toward Schrödinger waves. The possibility of a complete 3-D photonic bandgap has stimulated the imagination and led to a field [3, 45] of electromagnetic band structure engineering. Based on the similarities between the Schrödinger equation and Maxwell's equation, the terminology which was used to describe photon waves [43, 44] has been largely borrowed from solid state physics [46, 47]: reciprocal lattice, Brillouin zones (BZ), dispersion relations, Bloch function, etc.

A frequency-forbidden band around the K vector is raised due to the periodicity in space. Figure 7.1 shows the dispersion relation of both electron and photon in crystal. The forbidden band is open in the photonic crystal due to the periodicity of the structure, and the electron dispersion relation is scaled down 1000 times to fit in the same plot. Electrons in the conduction band have a tendency to recombine with holes in the valence band and emit a photon with a frequency characteristic of the energy gap. But if the energy of this emitted photon lies into the forbidden gap of the photonic crystal, this electron-hole recombination process is then inhibited. The most interesting property is that if the photonic bandgap lies over the semiconductor bandgap, we will be able to control the spontaneous recombination process. To find

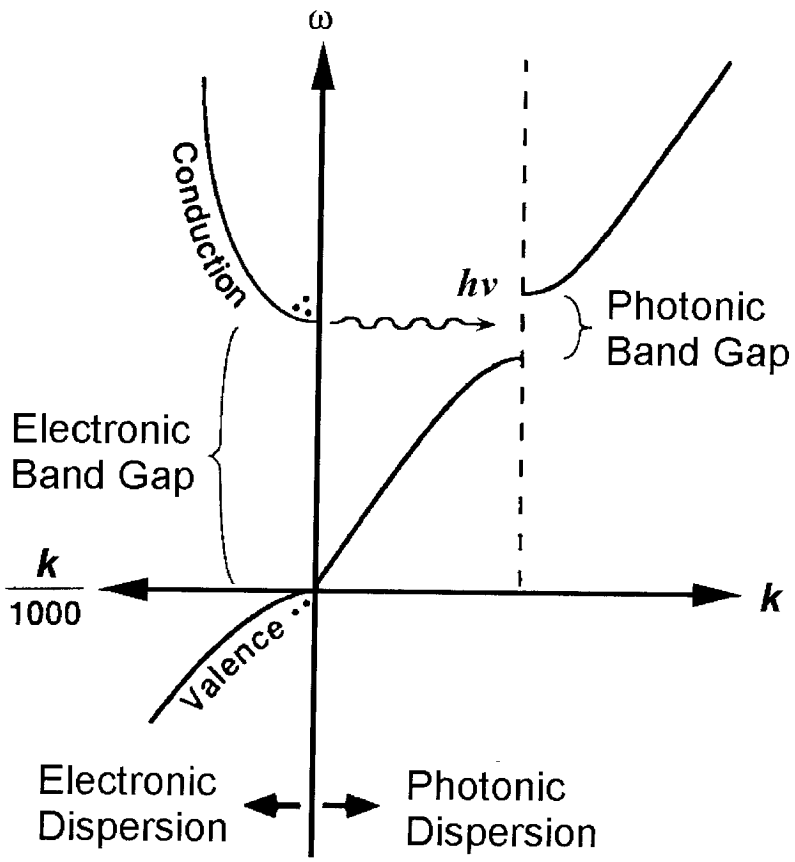

Figure 7.1: Dispersion relation of both electron and photon in a photonic bandgap crystal, after E. Yablonovitch 1993 [3]

a structure with three-dimensional periodicity and a complete bandgap, we can learn from solid state physics. In order to overlap the forbidden bands in different directions, the face center cubic (FCC) structure in which the first Brillouin zone closely matches a sphere is a good candidate. Yablonovitch *etal.* made several attempts in searching for the complete bandgap using variations of FCC structures [48, 49, 5, 50]. In addition to the geometry of the structure, he also found that the refractive index contrast should be large enough to obtain a complete photonic bandgap. The detailed description of such a 3D photonic crystal will be given in next chapter.

Donor and acceptor modes in solid state physics are the essential properties of semiconductor devices and also applicable to photonic crystals [51, 3, 45]. Photonic bandgap structures are expected to lead to devices with interesting and unusual properties such as inhibition of spontaneous emission, and localization of modes [43, 44, 3]. In 1946, E. Purcell suggested that the spontaneous emission can be enhanced in a small cavity [52].

$$spontaneous\ emission\ enhancement\ factor = \frac{(\frac{\lambda}{n})^3 Q}{8\pi V_{cav}} \tag{7.1}$$

In a 3D photonic bandgap structure, electromagnetic modes, spontaneous emission and zero-point fluctuations are all absent. The insertion of a local defect in a photonic crystal leads to a high-Q, single-mode nano-cavity [5]. These nano-cavities will ultimately permit full 3D confinement in the tiniest optical mode volume $\approx (\lambda/2n)^3$, where n is the refractive index. The spontaneous emission enhancement factor is higher, and all spontaneous emission will be useful. The ability to control electromagnetic mode density has suggested the use of these artificial structures for applications in quantum optics such as photon-number state-squeezing [53], single-mode light-emitting diodes [3] and photon localization [44], the analog of Anderson localization [54] for electrons in disordered media.

Originally, the application for photonic crystals was focused on lowering threshold currents for lasers and increasing the efficiency of light emitting diodes. However, more recently passive elements such as high reflectivity mirrors, low loss waveguides,

and polarizing beam splitters have also become very attractive. In this part of work, we would like to demonstrate the techniques for fabrication and characterization of the first 3D photonic crystal in the infrared region.

7.2 Motivation

The beauty of the Maxwell's equations is that the dimensions are scaleable. Researchers have developed sophisticated techniques in the microwave field for years. Usually, microwave models are used to study photonic crystals. Many groups have successfully designed and fabricated 2D and 3D photonic structures in the microwave region [49, 55, 56, 57, 58, 59]. They showed a good agreement between the theoretical prediction and experimental results. In 1991, Yablonovitch built the first 3D photonic crystal which was modified from a face center cubic (FCC) structure showing a complete bandgap in the microwave range [50]. This structure is later referred to as "Yablonovite" [45]. Figure 7.2 is a schematic procedure for defining Yablonovite. A group in Iowa State University later proposed a layer-by-layer structure shown in Figure 7.3 which is a modified version of diamond structure and obtained a complete bandgap [4, 60].

The complete bandgap obtained in microwave spectra raises a lot of interests in scaling the dimension down to the optical range. However, because of the absence of easy microfabrication processes, the interest in applying photonic crystals to the optical region has focused mainly on 1D and 2D photonic crystals [61, 34, 62, 35]. Typically, 2D photonic crystals have been made by planar pattern definition of rods or holes perpendicular to the wafer surface by transferring 2D periodic patterns straight into the semiconductor (as we show in part 2). The microfabrication of 3D photonic crystals, however, is more difficult than that of 2D crystals because angle etching or regrowth are required to obtain a refraction index modulation in the Z direction. For far infrared radiation, the structures proposed by the Iowa group can be fabricated simpler than Yablonovite in larger dimensions. But when the dimensions of the structures shrinks down to the sub-micron range, the Iowa structure requires pre-

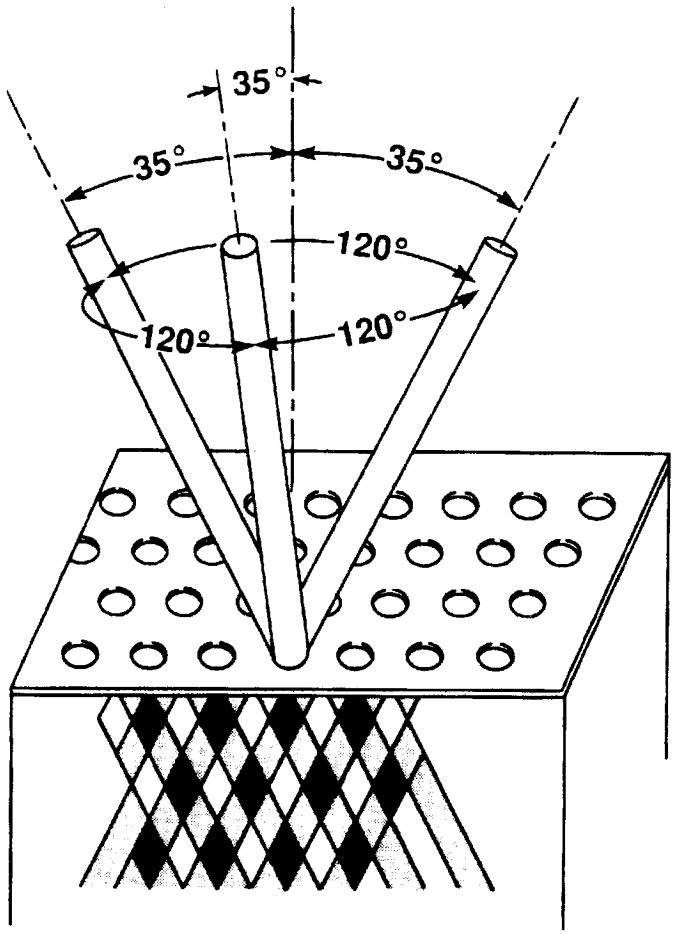

Figure 7.2: Schematic process of 3D photonic crystals (Yablonovite)

cise alignment of layer-by-layer patterns. Compared with complicated regrowth and alignment procedure for Iowa structures, Yablonovite seems more straightforward in the fabrication issue. The details of this structure will be described in the following section.

7.2.1 Structure of Yablonovite

In 1991 Yablonovitch proposed a modified FCC structure which exhibits a complete photonic bandgap and later was referred to as "Yablonovite" [5]. Before he proposed this idea, he had been working on several versions of FCC structures but none of them showed a complete bandgap [48, 49]. Yablonovite is based on an FCC-like structure

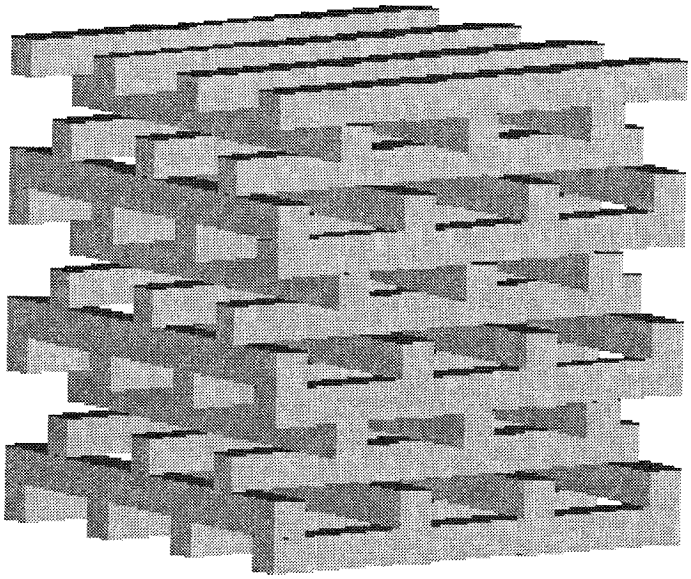

Figure 7.3: Picture of 3D photonic crystals proposed by Iowa group, after K.M. Ho *etal.* 1994 [4]

which three straight rods etched into a hexagonal array of holes at 35.26° to the normal and spread 120° on the azimuth (see Figure 7.2 in the previous session). It is essentially a diamond-like structure. The idea originally came from an FCC crystal because the first Brillouin zone (BZ) of an FCC crystal is very close to a sphere which may increase the chance of an overlapping continuous bandgap in all directions. (see Figure 7.4) Instead of putting air spheres in the lattice locations, three straight holes are etched into three facets in the Wigner-Seitz cell of an FCC crystal [3, 5] (see Figure 7.5). Looking straight onto the (1,1,1) plane of an FCC cubic, these three holes are corresponding to ⟨1,1,0⟩, ⟨1,0,1⟩, and ⟨0,1,1⟩ directions.

Figures 7.6–7.9 show the four different views of the crystal. The air volume and the refractive index contrast of the structures can also change the band structures. The detail of the design will be discussed in the next section. Figure 7.10 shows a complete forbidden gap along the BZ of Yablonovite. Theoretical calculations and microwave experimental results are compared [5]. The width of the forbidden gap is

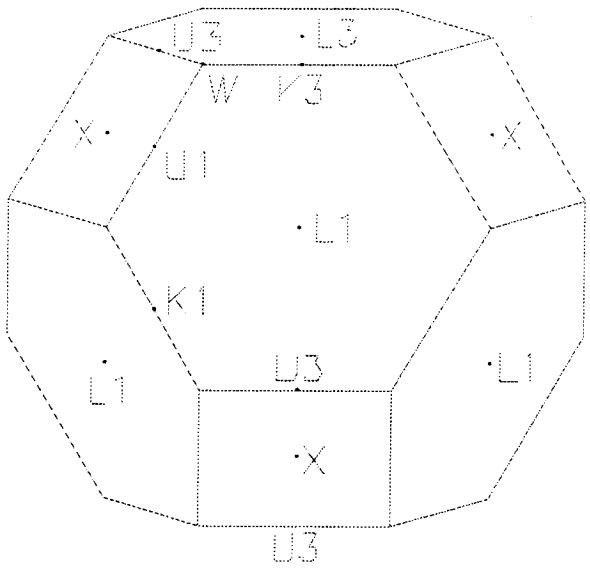

Figure 7.4: First Brillouin zone of Yablonovite which is similar with an FCC crystal

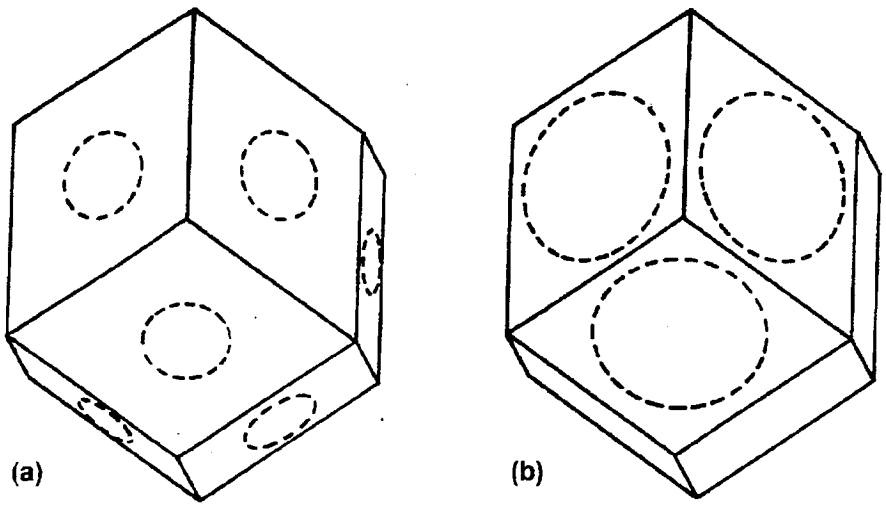

Figure 7.5: Wigner-Seitz cell of (a) FCC crystal and (b) Yablonovite, the dot circle indicates the air sphere or air column

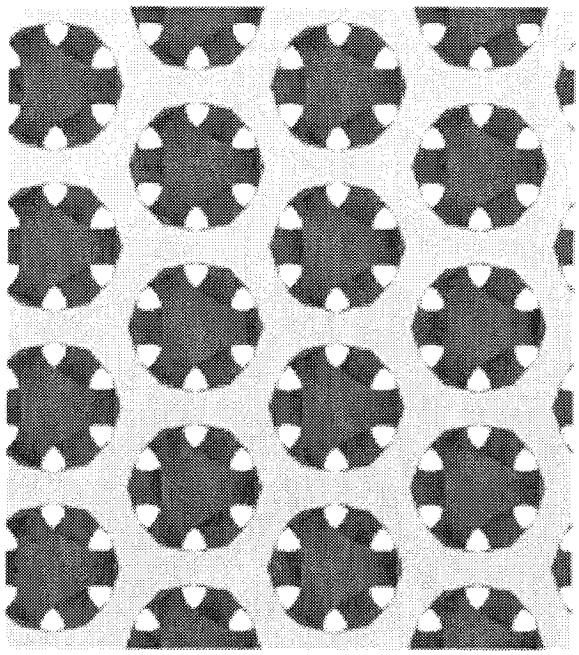

Figure 7.6: Top view of a 3D photonic crystal

determined by both the geometry and the refractive index contrast [7].

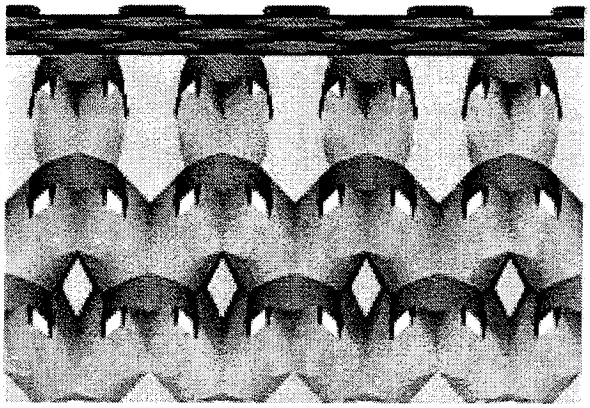

Figure 7.7: Cross section view of a 3D photonic crystal

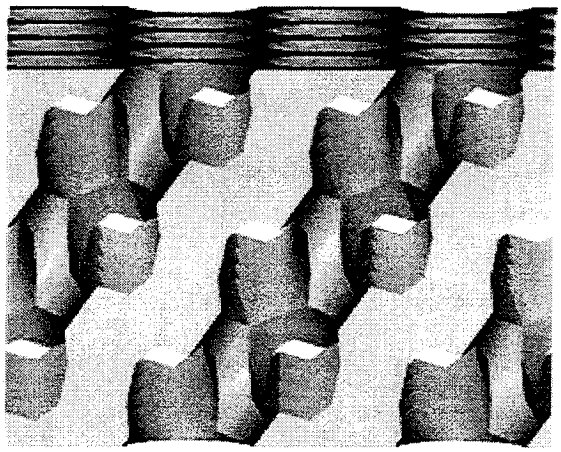

Figure 7.8: Cross section view of a 3D photonic crystal

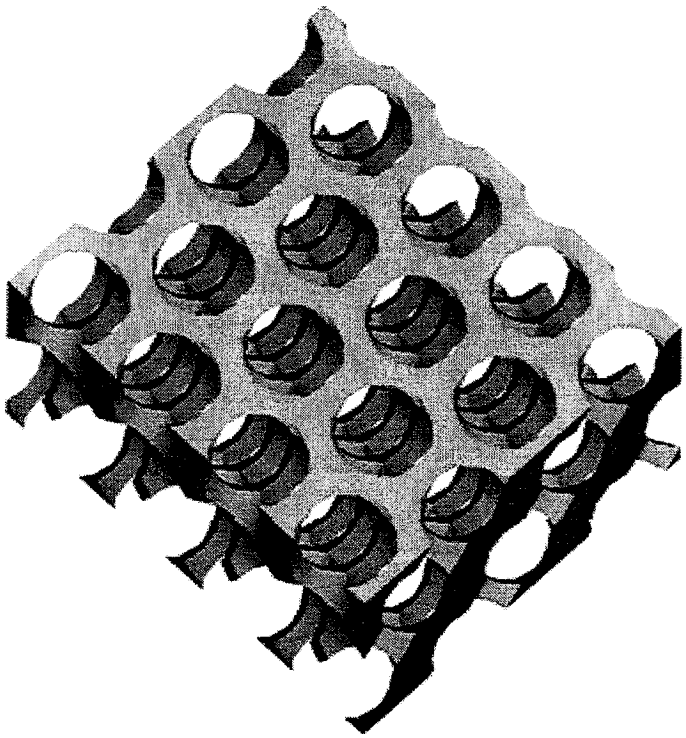

Figure 7.9: Tilt view of a 3D photonic crystal

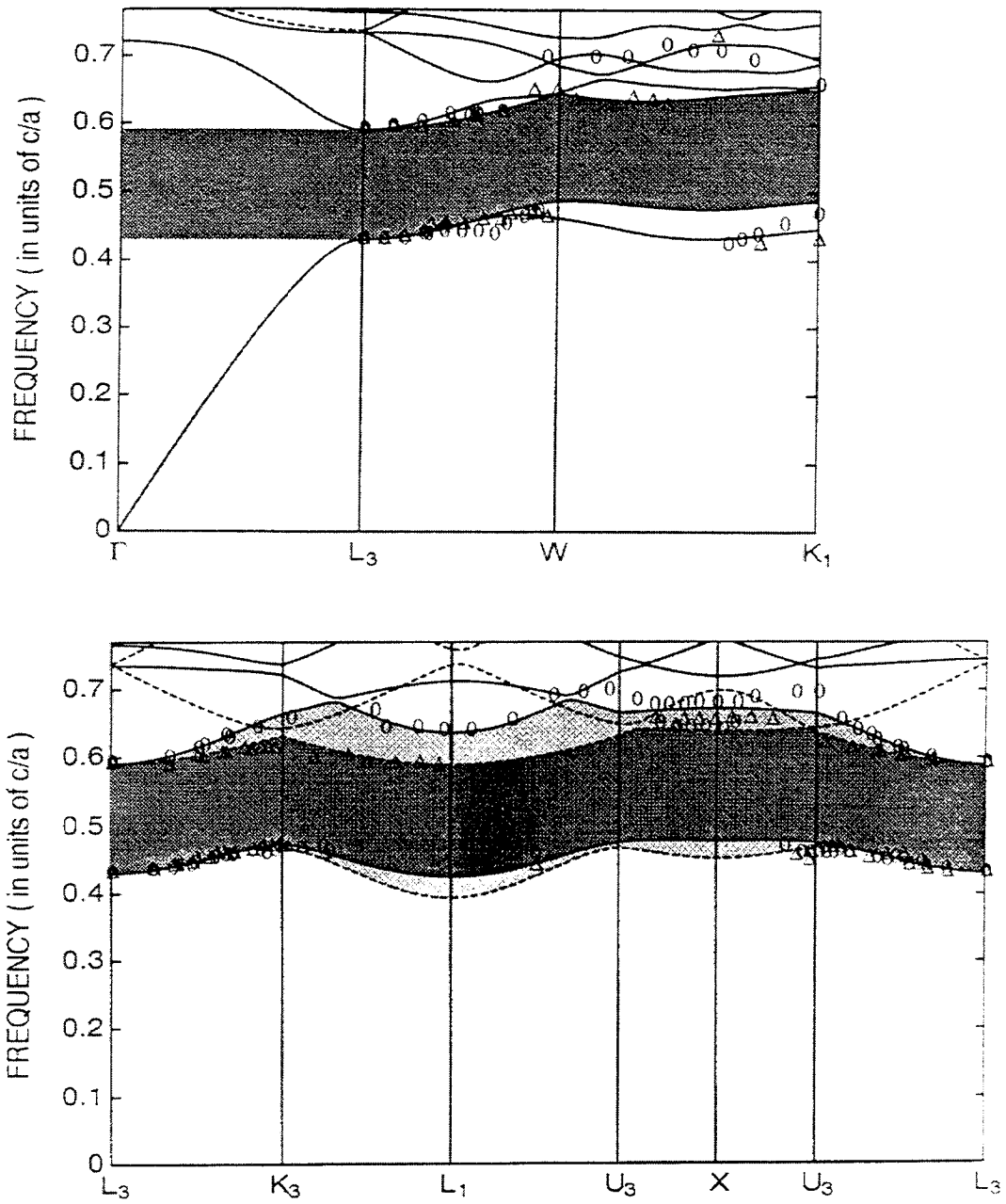

Figure 7.10: The dispersion relationship exhibits a complete forbidden gap along the BZ of Yablonovite shown in Figure 7.4. The solid and dashed curves are the theoretical calculations for s and p polarization, respectively. The ovals and triangles are the microwave experimental results for s and p polarizations, respectively, after E. Yablonovitch *etal.* 1991 [5]

Chapter 8 Design and fabrication of 3D photonic crystals

8.1 Theoretical approach

8.1.1 Plane wave expansion

The behavior of the electromagnetic waves can be clearly described by Maxwell's equations [63, 64]. We consider the simplest case which the medium is linear, isotropic, source-free and magnetic permeability is constant over the medium. We have

$$\nabla \cdot \epsilon(\vec{r})E(\vec{r},t) = 0 \tag{8.1}$$

$$\nabla \cdot H(\vec{r},t) = 0 \tag{8.2}$$

$$\nabla \times E(\vec{r},t) = -\frac{1}{c}\frac{\partial H(\vec{r},t)}{\partial t} \tag{8.3}$$

$$\nabla \times H(\vec{r},t) = \frac{\epsilon(\vec{r})}{c}\frac{\partial E(\vec{r},t)}{\partial t} \tag{8.4}$$

and the wave equations for both magnetic field and electric field are

$$\nabla \times (\frac{1}{\epsilon(\vec{r})}\nabla \times H(\vec{r})) = \frac{\omega^2}{c^2}H(\vec{r},t) \tag{8.5}$$

$$\nabla \times (\nabla \times E(\vec{r})) = -\frac{\omega^2}{c^2}\epsilon(\vec{r})E(\vec{r},t) \tag{8.6}$$

We start with a lossless periodic dielectric structure. Since the dielectric constant $\epsilon(\vec{r})$ is a periodic function, it is possible to expand it into a series of Bloch functions.

$$\epsilon(\vec{r}) = \sum_G \varepsilon_G exp(iG \cdot \vec{r}) \tag{8.7}$$

where G is a reciprocal-lattice vector, and ε_G is Fourier coefficient. The electric and magnetic fields can be expanded by the same Bloch functions.

$$H(\vec{r},t) = e^{-wt}\sum_G H_G exp[i(\vec{k}+G)\cdot\vec{r}] \tag{8.8}$$

$$E(\vec{r},t) = e^{-wt}\sum_G E_G exp[i(\vec{k}+G)\cdot\vec{r}] \tag{8.9}$$

where H_G and E_G are Fourier coefficients. Therefore, we substitute the wave equations with the Block function above and we have [24]

$$(\vec{k}+G)\times[\sum_{G'}\eta_{G'G}(\vec{k}+G')\times H_{G'}]+\omega^2 H_G = 0 \tag{8.10}$$

$$(\vec{k}+G)\times[(\vec{k}+G)\times E_G]+\omega^2\sum_{G'}\varepsilon_{GG'}E_{G'} = 0 \tag{8.11}$$

where

$$\epsilon_{GG'} = \varepsilon(G-G') \quad , \epsilon(\vec{r}) = \sum_G \varepsilon_G exp(iG\cdot\vec{r}) \tag{8.12}$$

$$\eta_{GG'} = \eta(G-G') \quad , \frac{1}{\epsilon(\vec{r})} = \sum_G \eta_G exp(iG\cdot\vec{r}) \tag{8.13}$$

By solving these eigenvalue problems, we quickly obtain the dispersion information about the structures. The accuracy of the calculation is determined by the number of expansion waves. The magnetic wave equation is easier to calculate because the operator of the eigenvalue problem is Hermitian [45, 65]. If the periodicity of the structure is only in one or two dimensions, we can easily solve the eigenvalue problem [24, 66]. But in three-dimensional case, the problem becomes more complicated. Leung *etal.* have solved the particular Yablonovite case using a full vector wave calculation [7]. The result is shown in the previous chapter. For three-dimensional structures or non-perfect periodic structures, the plane wave expansion method is not a convenient way to proceed. To overcome these problems, a finite-difference time-domain (FDTD) method is used.

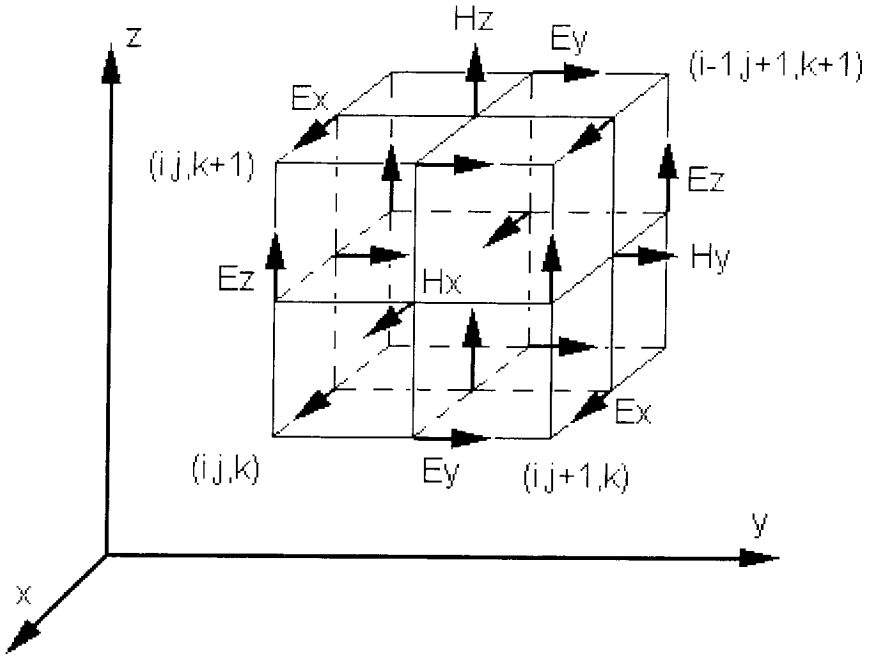

Figure 8.1: The position of the field components in Yee's mesh for finite-difference approximation, after K. S. Yee 1966 [6]

8.1.2 Finite-difference time-domain method

Finite-difference (FD) techniques have been developed to provide a very efficient way of solving time domain electromagnetic field problems. In a FD method, a space-time mesh is applied and Maxwell's equations are replaced by a system of FD equations on the mesh. The mesh can be applied on either homogeneous or inhomogeneous structures [6, 67, 68]. Typically, a mesh with Cartesian coordinates is used. We denote mesh points as

$$(i, j, k) = (i\delta, j\delta, k\delta) \tag{8.14}$$

where $\delta = \delta x = \delta y = \delta z$ is the space increment, and any function of space and time as

$$F^n(i, j, k) = F(i\delta, j\delta, k\delta, n\delta t) \tag{8.15}$$

We position the field components of E and H on the mesh following Yee's notation and evaluate E and H at alternate half-time steps (see Figure 8.1). Using the differential form of Maxwell's equations

$$\mu \partial_t H = -\nabla \times E \tag{8.16}$$

$$\epsilon \partial_t E = \nabla \times H \tag{8.17}$$

we get the FD approximation. (Here, only the x-component is shown.)

$$\begin{aligned} {H_x}^{n+\frac{1}{2}}(i, j+\frac{1}{2}, k+\frac{1}{2}) &= {H_x}^{n-\frac{1}{2}}(i, j+\frac{1}{2}, k+\frac{1}{2}) \\ &- (\frac{\delta t}{\mu \delta}) \cdot [{E_z}^n(i, j+1, k+\frac{1}{2}) - {E_z}^n(i, j, k+\frac{1}{2}) \\ &- {E_y}^n(i, j+\frac{1}{2}, k+1) + {E_y}^n(i, j+\frac{1}{2}, k+1)] \end{aligned} \tag{8.18}$$

$$\begin{aligned} {E_x}^{n+1}(i+\frac{1}{2}, j, k) &= {E_x}^n(i+\frac{1}{2}, j, k) \\ &+ (\frac{\delta t}{\epsilon \delta}) \cdot [{H_z}^{n+\frac{1}{2}}(i+\frac{1}{2}, j+\frac{1}{2}, k) - {H_z}^{n+\frac{1}{2}}(i+\frac{1}{2}, j-\frac{1}{2}, k) \\ &- {H_y}^{n+\frac{1}{2}}(i+\frac{1}{2}, j, k+\frac{1}{2}) + {H_y}^{n+\frac{1}{2}}(i+\frac{1}{2}, j, k-\frac{1}{2})] \end{aligned} \tag{8.19}$$

One can now evolve in time the initial field values at each point using the above equations.

If the crystal is not perfectly periodic, the plane wave expansion method usually has difficulty in converging because of the high frequency terms caused by the discontinuity. In this case, the finite-difference time-domain method has several advantages over the plane wave expansion method. The arbitrary dielectric function can be solved to an arbitrary accuracy dependent on the size of the cells. The time domain calculation with an additional filter can greatly reduce the calculation time. In order to find a field distribution at a certain frequency, we multiply the frequency spectrum with a notch filter [69]. We did all the calculations in the time domain, which corresponds to a convolution between the real field distribution and a sinc function. The length of convolution determines the width of the resultant filter in frequency.

The disadvantage of this method is the large demand on the computing memory. With limited computer memory, we applied the filtered finite-difference time-domain calculation to analyze the finite depth of a 3D photonic crystal. The calculation is conducted on 3D photonic crystals with infinite periodicity in X-Y plane and only three and a half layers in Z direction. The crystals are sandwiched by air and dielectric substrate. The structure is shown in Figure 8.2. In order to calculate the electric field distribution, an initial plane wave incident on the surface was used. The structure is mirrored in the Z direction. Figure 8.2 shows the simulated electrical field distribution in $3\frac{1}{2}$ periods of Yablonovite. The simulated results show that most of electric energy is scattered outside of photonic crystals and only a small part of electric energy passes through photonic crystals and leaks out from the substrate. We can calculate the quality factor (Q-factor) by calculating the energy dissipation.

$$Q = \frac{-\omega \int_0^T u(t)}{(u(T) - u(0))} \tag{8.20}$$

where $u(t)$ is the energy distribution at time t, and ω is the specific frequency. Then we can obtain the reflectivity of the structure by

$$Q = \frac{2\pi L_\lambda}{-lnR} \tag{8.21}$$

where L_λ is the cavity length in wavelength, and R is the modal reflectivity [69].

8.2 Experimental approach in 3D optical photonic crystals

8.2.1 Design criterion

Here, we describe the methods used to fabricate a 3D photonic crystal in the near infrared range. First, we have to choose a material which is transparent with low absorption in the wavelength regime. The higher the refractive index contrast is, the

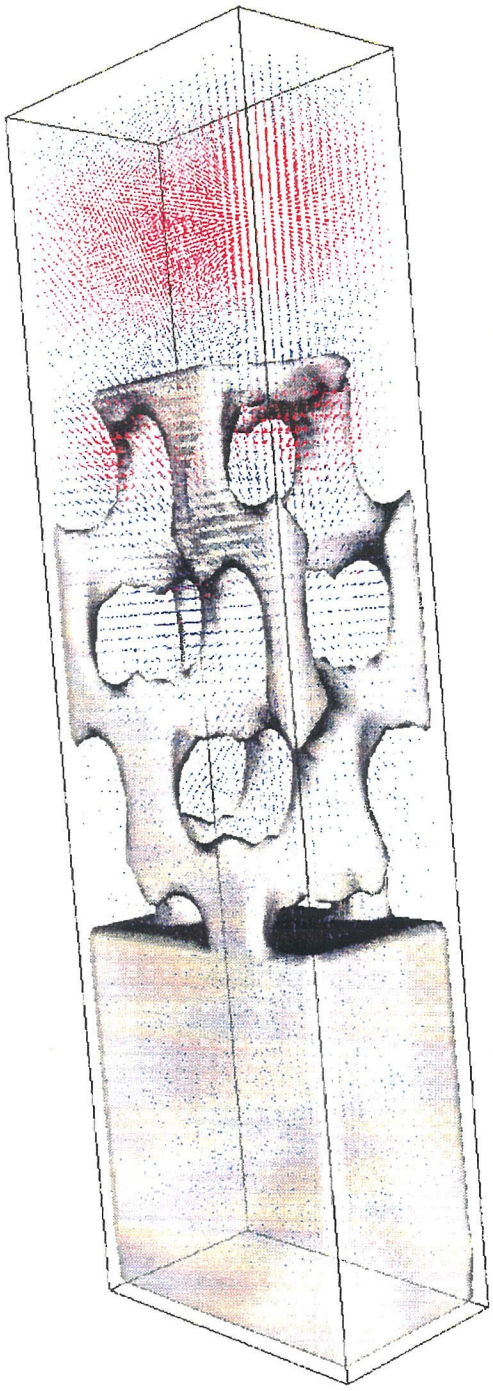

Figure 8.2: Stimulated electric field distribution calculated by filtered finite-difference time-domain method for a unit cell of $3\frac{1}{2}$ layers of Yablonovite, the dielectric constant is 12.96 and the major hole diameter is 0.53 in unit of length of lattice constant

wider the resulting bandgap will open. Moreover, the most important issue is the fabrication capability. Combined with all of the factors mentioned above, we have chosen GaAs as a substrate with a high refractive index (n=3.6) and low absorption in the near infrared region.

The dimension of the crystal depends on the hexagonal array of (1,1,1) planes. Figure 8.3 is a contour plot of gap widths and the midgap frequency as a function of refractive index n and d/a [7]. From this figure, we choose the midgap frequency and the gap width (15% of the midgap frequency) for GaAs and then find out the lattice constant a and the major diameter d. In order to characterize 3D photonic crystals in the infrared range, the dimension of photonic crystals must locate within a window of the GaAs band edge and the absorption limitation of the InGaAs photodetector. Figure 8.4 shows the conduction band edge as a function of center to center spacing in the (1,1,1) plane and major hole diameter within the window for GaAs substrate.

8.2.2 Calibration of process

The fabrication of these 3D photonic crystals depends on both lithography and anisotropic etching processes. Nonuniformity in lithographically defined hexagonal patterns results from an unstable electron beam during resist exposure and development. A better way to reach uniformity is to adjust the exposure dose and the development. The mask amplification process also requires high anisotropic etching. Careful calibration is required during the angle etching. Figure 8.5 shows that excessive reactive gas causes undercuts and hollow structures under the mask. Figure 8.6 shows that less reactive gas causes significant surface roughness of structure during the etching. The roughness results in the undesirable optical properties. The anisotropic etching can be accomplished by adjusting the reactive gas pressure and the ion beam voltage.

Figure 8.7 shows the unbalanced etching depth between three different angle directions resulting in the gradient refractive index contrast [33]. The unbalanced etching in three directions can be improved by rotating the sample frequently during the

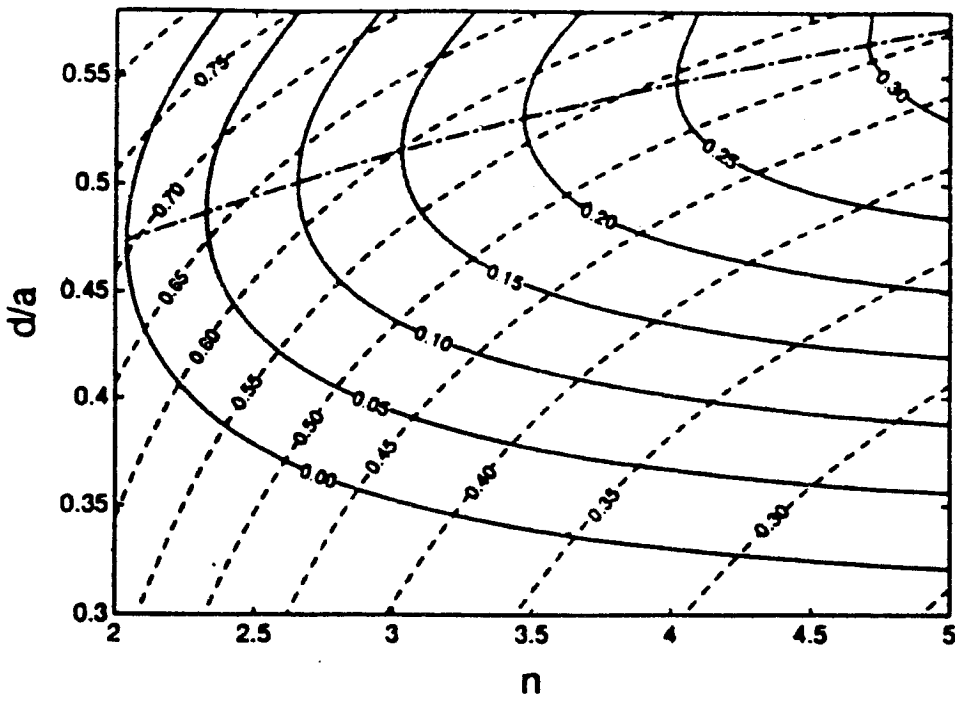

Figure 8.3: Contour relationship of gap width to the midgap frequency ratio (solid lines) and the midgap frequency in reduced unit (i.e., c/a) (dashed lines) as a function of both the refractive index contrast n and the major diameter of the oval holes (i.e., d/a) for Yablonovite. The dashdotted line gives the optimum diameter as a function of the refractive index, after G.X. Qian *etal.* 1991 [7]

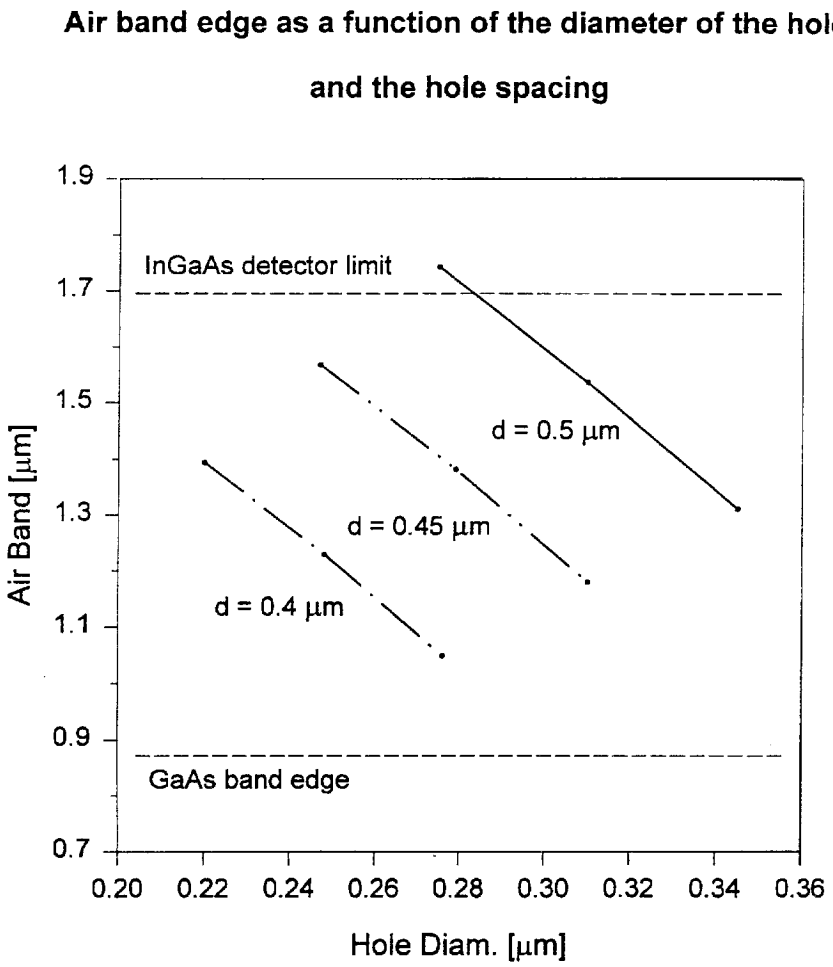

Figure 8.4: Conduction band edge as a function of the center to center spacing and the major hole diameter for Yablonovite in the infrared range

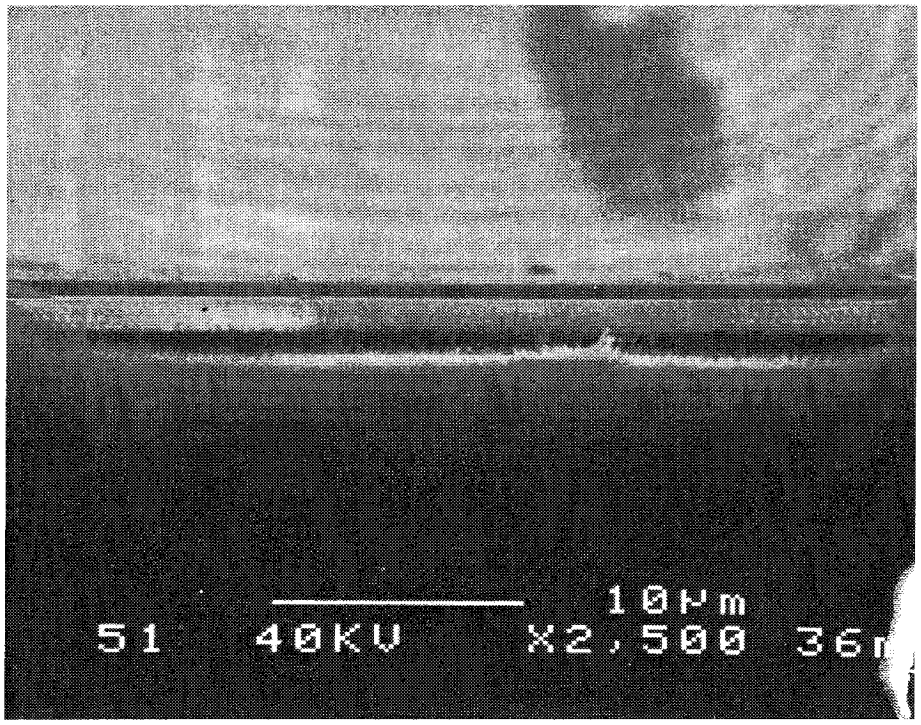

Figure 8.5: SEM image of undercut structures due to excess reactive gas

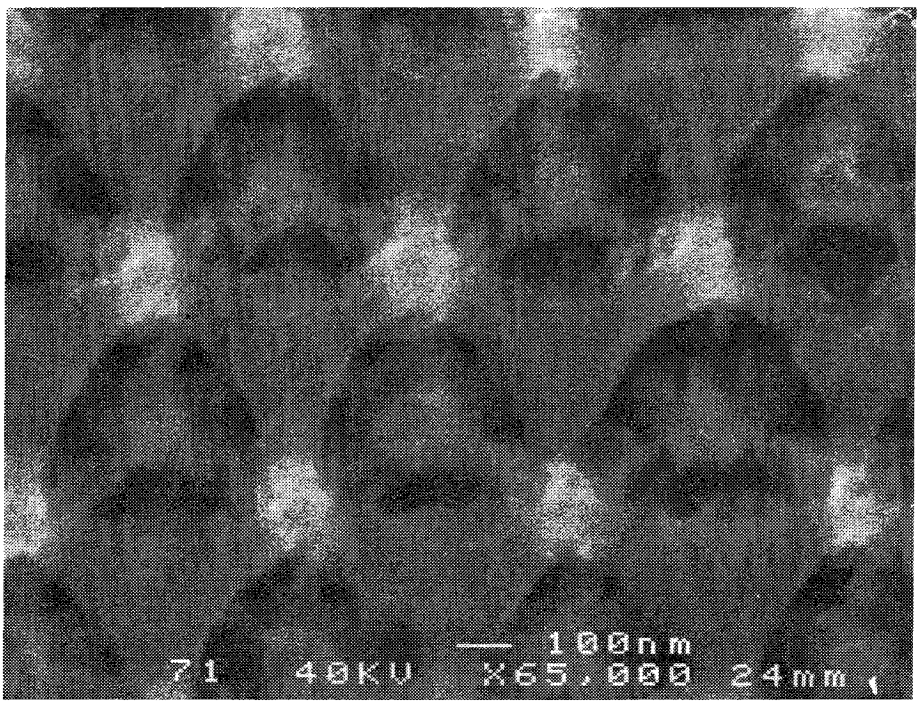

Figure 8.6: SEM image of rough surfaced structures due to less reactive gas

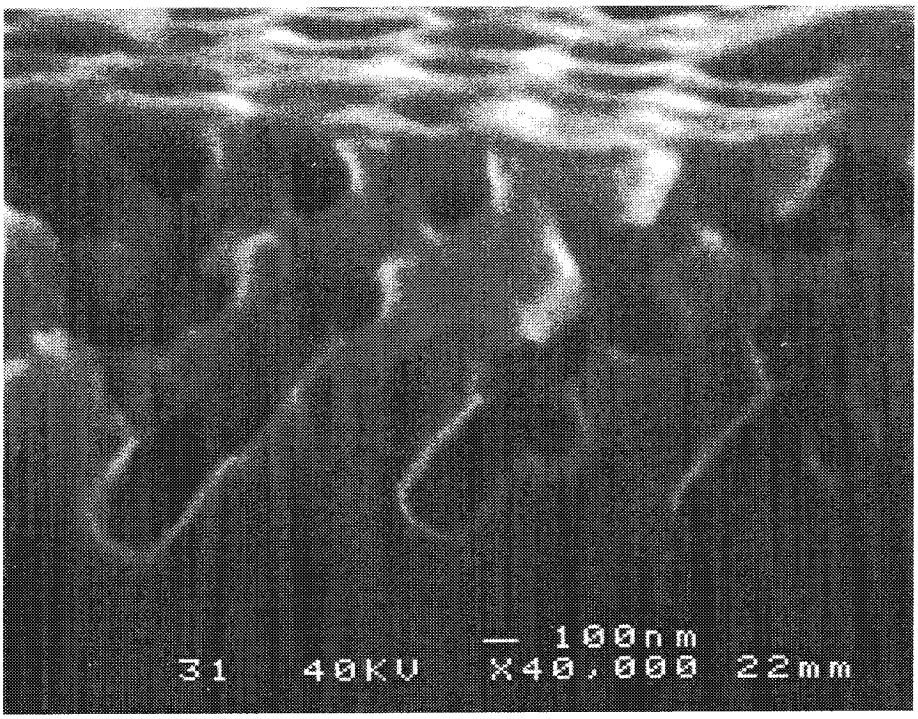

Figure 8.7: SEM image of structure with unbalance etching in three directions

etching. The first direction requires longer etching time to remove more material. The second direction etching time should be half as long and the third direction, one-third as long as the first direction's time. After two or three rotations, the etching depths are similar in all three directions. The other solution for the unbalanced etching depth is simultaneously using three ion guns which tilt at 35 degrees and 120 degrees apart instead of just using one ion gun. The problem of using three guns is the different etching rates among one another. More careful calibration is required to achieve similar etching rates. Mask erosion is also more serious when operating two or three ion guns at the same time. A robust mask is necessary when using multiple ion sources.

8.3 Fabrication using SiO_2 and Ni masks

As part of this research, we have reported the successful microfabrication of 3D photonic crystals with four repeating (1,1,1) layers in depth, fabricated for reflection in the infrared range [70]. These previous results were obtained by using a robust planar SiO_2 and Ni mask. Figure 8.8 shows the scheme of fabrication procedure. Here, we demonstrate the details of the fabrication procedure. First, a SiO_2 layer of thickness 400nm is deposited by reactive sputtering on the top of GaAs wafer and followed by a 100nm evaporated Au layer. The thickness of the SiO_2 mask is critical because a thinner layer would limit the total etch depth and a thicker layer would cause shadow effects during the final angle etching. A 30kV electron beam defines the hexagonal array of holes in a 70nm PMMA layer. The PMMA pattern is then developed at 3:7 cellusive:methanol for 15 seconds and works as a mask to transfer the pattern into the Au layer using argon ion milling accelerated at 1.5kV. Figure 8.9 shows the SEM image of the pattern after ion milling. Next, a SiO_2 layer is patterned by reactive ion etching using C_2F_6 as reactive gas at an etch rate of 20nm/min. Figure 8.10 shows the SEM image of the pattern after reactive ion etching. The selectivity in reactive ion etching between Au and SiO_2 is about 4:1, which is lower than Cr vs. SiO_2. The advantage of using an Au layer instead of a Cr layer is that we can transfer the pattern from PMMA into SiO_2 without wet chemical etching. Finally, three-directional angle etchings are performed using chemically assisted ion beam etching (CAIBE) with an argon ion beam assisted by Cl_2 reactive gas. One ion gun with careful rotation sequences is used. Figure 8.11 shows the first and the smallest 3D photonic crystal fabricated on GaAsP substrate with 350nm spacing and 300nm hole diameters [33]. The Ni mask is then developed to improve the selectivity between mask and material. We have demonstrated the first 3D photonic crystals with up to four repeating layers in the near infrared range. Figure 8.12 shows the top view of 3D photonic crystals. Figure 8.13 and 8.14 show the two different cross section views of 3D photonic crystals. The nondestructive way to determine the number of periods in normal direction can be obtained by tilting the sample at a high angle in SEM.

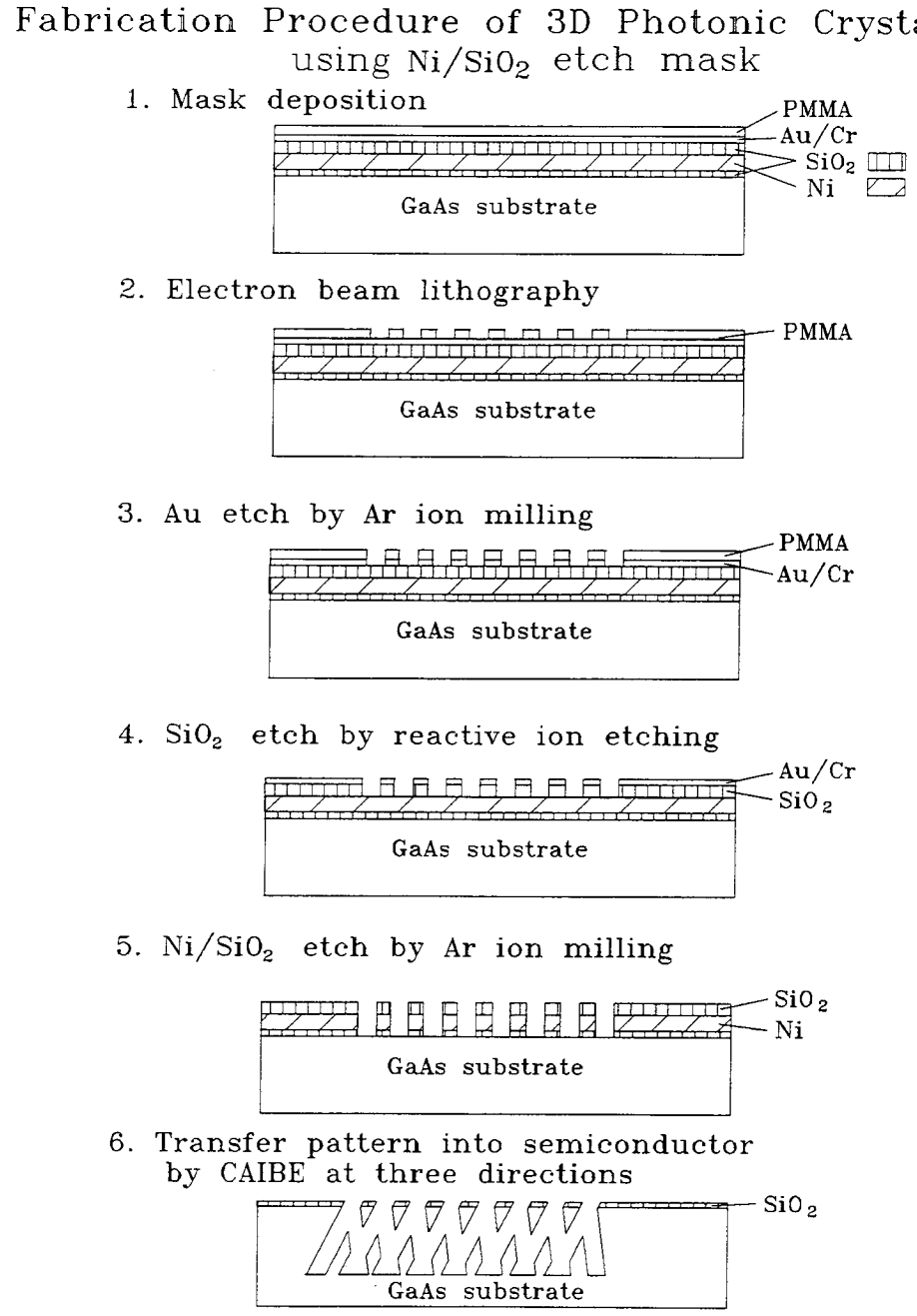

Figure 8.8: Fabrication procedure of 3D photonic crystals using Ni/SiO_2 etch mask

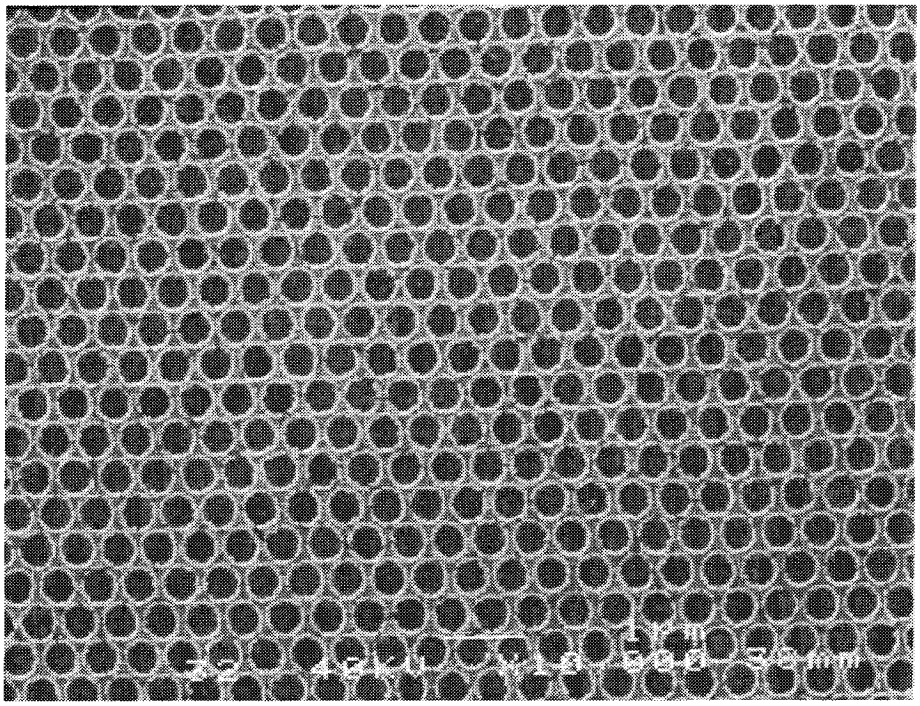

Figure 8.9: SEM image of Au hexagonal pattern after Ar ion milling

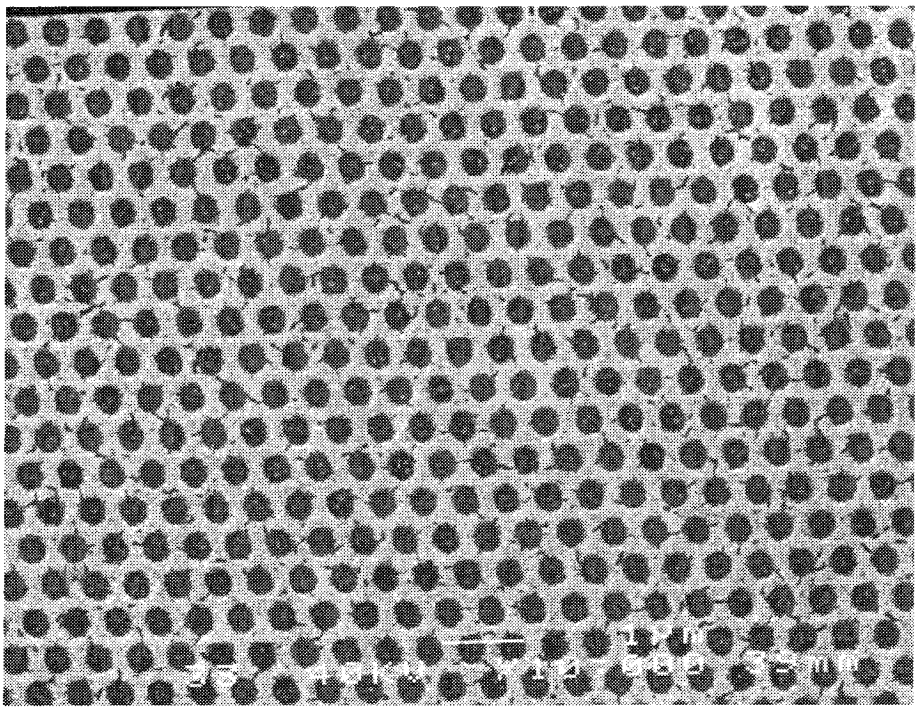

Figure 8.10: SEM image of hexagonal pattern after reactive ion etching

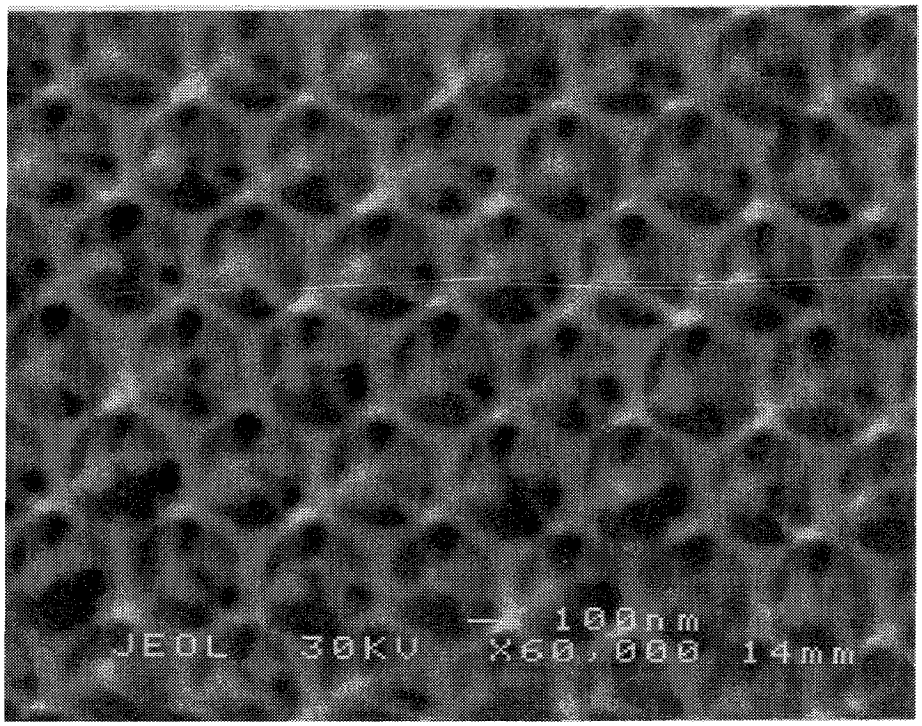

Figure 8.11: SEM image of the first and the smallest 3D photonic crystal on GaAsP substrate with 350nm spacing and 300nm hole diameter

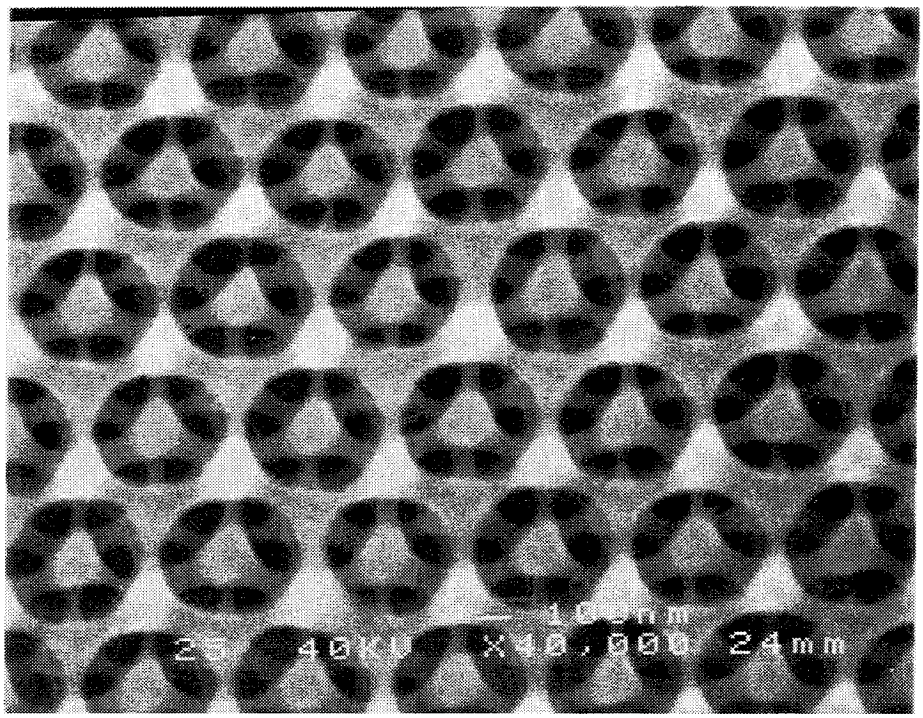

Figure 8.12: SEM image of top view of 3D photonic crystal

Figure 8.15 is the SEM image of four repeating layers of 3D photonic crystals tilting at 25 degrees. These can be compared with the computer generated figures from the previous chapter (see Figure 7.6-7.9), and it can be seen that they are exactly the same. The complicated sandwich Ni mask produces the deeper structure but also introduces fabrication errors. Figure 8.16 shows the fabrication error due to the Ni ion milling procedure. The main difficulties of constructing these crystals with dramatically improved optical performance lie in the limited depth of the crystals, as well as the fidelity of mask replication. Usually, the finite selectivity of a planar mask severely limits the total depth of the crystal.

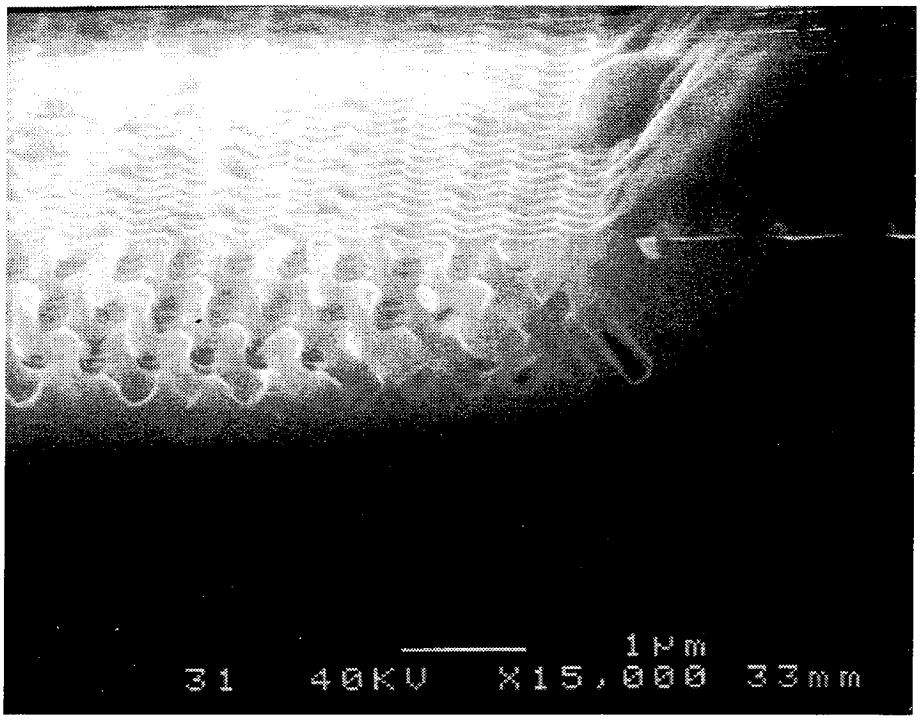

Figure 8.13: SEM image of cross section view of 3D photonic crystal

8.4 Results and measurements

8.4.1 Optical transmission measurements

The 3D photonic crystals are characterized using transmission measurements. The transmission spectrum is measured instead of the reflection spectrum because of the scattering loss in the latter measurement. The optical transmission characteristics of the nanofabricated photonic crystals are measured through a 40×40 μm^2 aperture in a Nickel mask, at room temperature, with the light incident along the photonic $\langle 111 \rangle$ axis parallel to the L^3 point in the photonic reciprocal space (surface normal to the GaAs wafer) [3]. The Ni aperture masks are thick enough to insure total opacity outside the area of the photonic crystal. The optical characterization setup is shown on Figure 8.17. A quartz tungsten halogen lamp along with an $f/4$ monochromator delivers wavelengths between 0.9 μm and 1.7 μm, within the transparent region of GaAs. This light is then focused onto the sample using an off-axis paraboloid mirror.

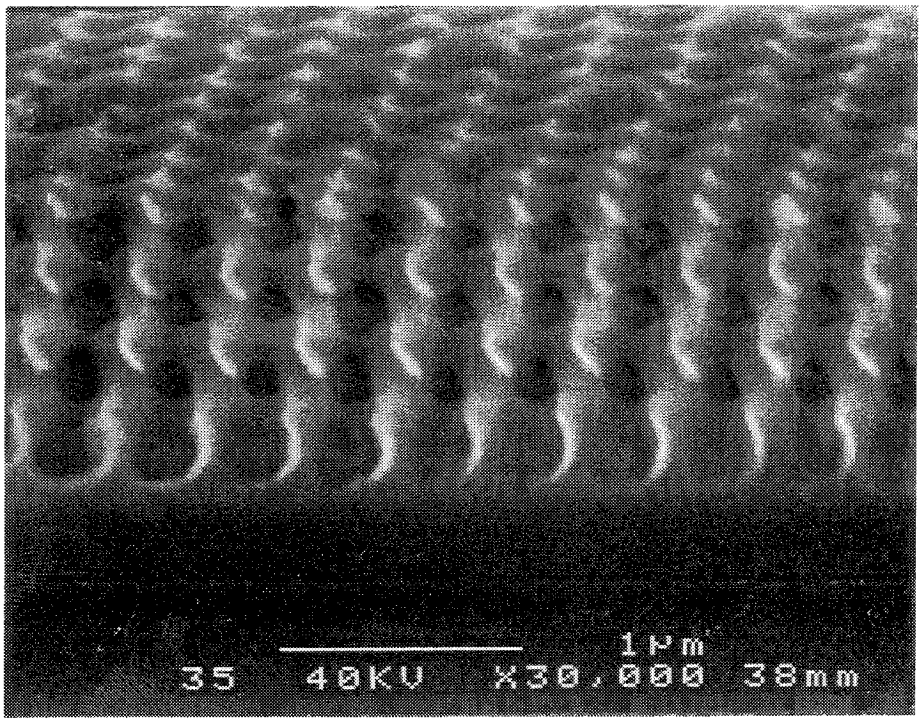

Figure 8.14: SEM image of cross section view of 3D photonic crystal

Reflective optical elements are needed in order to eliminate chromatic aberration, a severe problem in refractive optics while being used over the wide spectral range. The transmitted light is then collected in an InGaAs photodetector. For the absolute transmission calibration, the optical spectrum is normalized to the spectrum of an adjacent unpatterned 40×40 μm^2 aperture.

A measured optical transmission spectrum of a GaAs photonic crystal is shown by the solid line in Figure 8.18. The photonic bandgap lies in the near infrared with a width of about 19% of its mid-gap frequency. We notice that while the transmission at the photonic valence band edge approaches unity, the photonic conduction band exhibits only $\approx$40% transmission. This is quite common in the photonic crystals, and is due to the electromagnetic mode mismatch between external plane waves and internal Bloch conduction band modes [71]. The attenuation in the bandgap region of our microfabricated 3D photonic crystals only shows 80% reflectivity, which is lower than we expected from previous microwave measurements, described in the

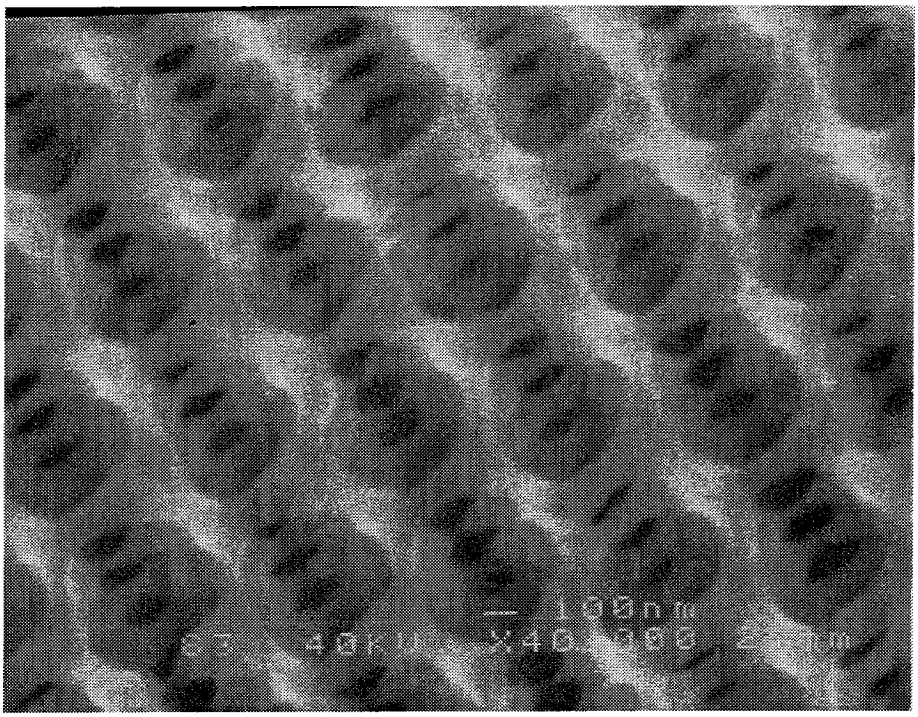

Figure 8.15: SEM image of tilted view of 3D photonic crystal

next section.

8.4.2 Comparison with microwave crystal

Microwave measurements for three repeating periods of a photonic crystal have been taken and scaled down to optical wavelength range to compare to our optical results. The scaling number is carefully chosen by the ratio of spacing, difference of dielectric constant, porosity change, and so on. The nondestructive inspection of microfabricated crystals is performed by scanning electron microscopy (SEM). We are able to determine the structure depth, variation of hole sizes as well as porosity by observation along the direction of one of the etched holes. Figure 8.18 shows that the conduction band of microwave models matches that of optical crystals, but the attenuation in the microwave models is much stronger than that in our photonic crystals. As the depth increases, the amount of attenuation should increase as predicted from microwave measurements. Three periods of a perfect 3D photonic crystal should yield

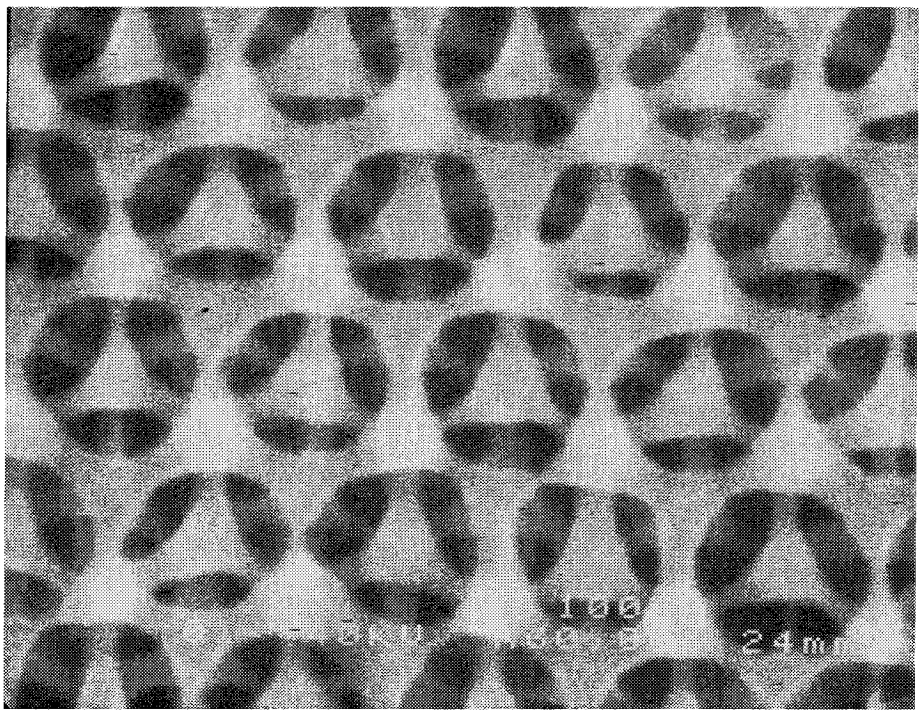

Figure 8.16: SEM image of top view of a 3D photonic crystal showing the fabrication error by Ni mask

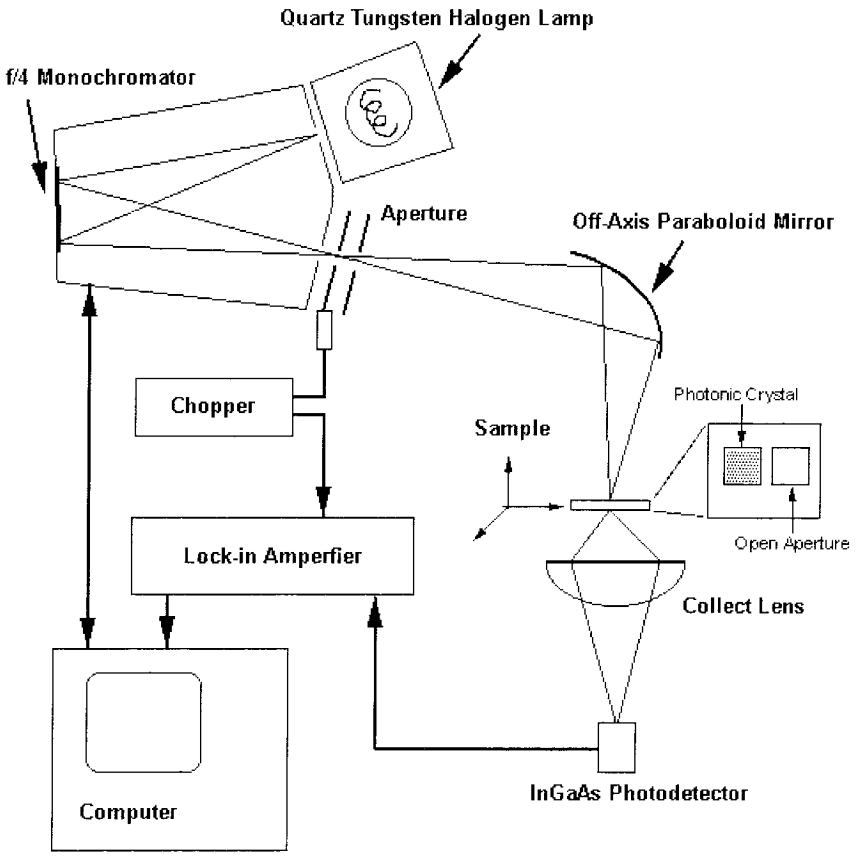

Figure 8.17: Optical characterization set up for 3D photonic crystal

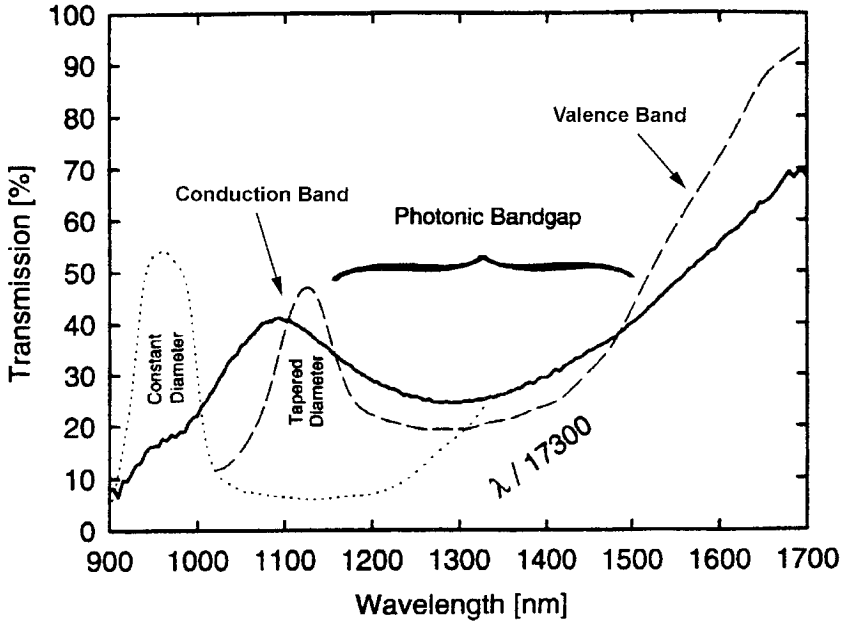

Figure 8.18: Typical transmission spectrum for four repeating layers of 3D photonic crystals showing 40% transmission on conduction band edge and 80% attenuation in the bandgap region.

a reflectivity in excess of 95%. We believe that the reason for the lower attenuation is the variation of hole sizes and tapered etching which results from mask erosion during the angle etching process.

Chapter 9 Spectra tuning by microfabrication

9.1 Lithographic tuning method

We have successfully fabricated 3D photonic crystals with up to four repeating layers in the optical wavelength range. The performance of these 3D photonic crystals is not as high as we expected because of microfabrication errors and limited depth. In order to verify the performance of these 3D crystals, we can deliberately change the structure spacing by microfabrication. With anisotropic angle etching, the 2D hexagonal mask pattern can be adjusted through changes in lithography to tune the spectral properties of the resulting crystals.

We have fabricated and characterized an array of photonic crystals with varying spacings and hole sizes on a double-polished GaAs wafer (Figure 9.1). The lithographic dimensions of these crystals are chosen from model predictions to yield photonic band gaps in the near-infrared wavelength range. The spacing between the holes in the lithographic pattern which defines the (111) plane of the FCC crystal is proportional to the lattice parameter and center wavelength of the band gap in a photonic crystal. Thus, it is possible to tune the center wavelength of a structure during the electron beam writing step by systematically changing the distances between holes. Similarly, the sizes of the holes with a given spacing also influence the spectral response since the hole size changes the porosity of the crystal, and thereby alters the average refractive index of the resulting photonic structure. The hole diameter can also be changed lithographically, and can be conveniently adjusted by altering the exposure dose during the beam writing process.

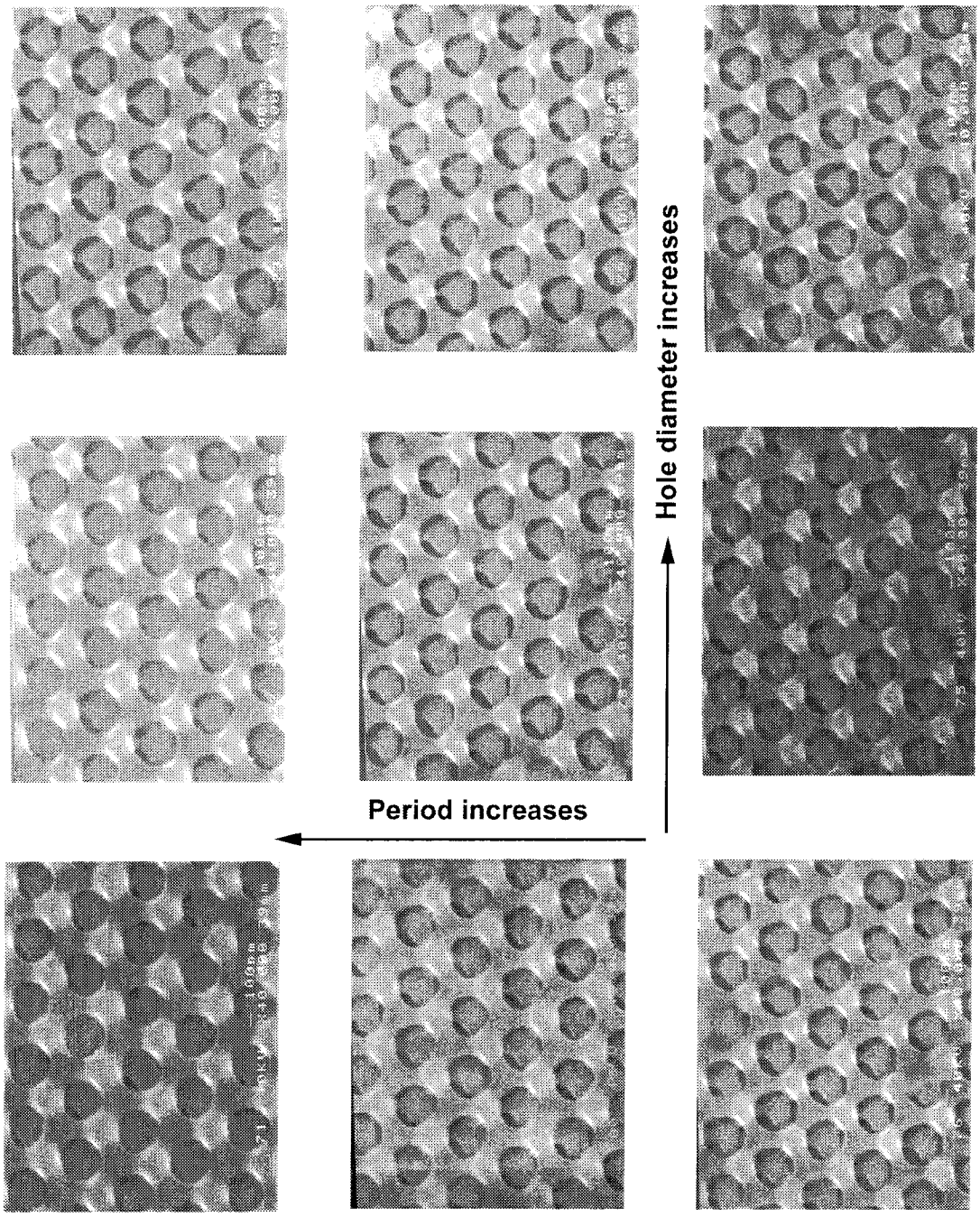

Figure 9.1: Array of 3D photonic crystals with varying center to center spacings and hole diameters by lithographically tuning

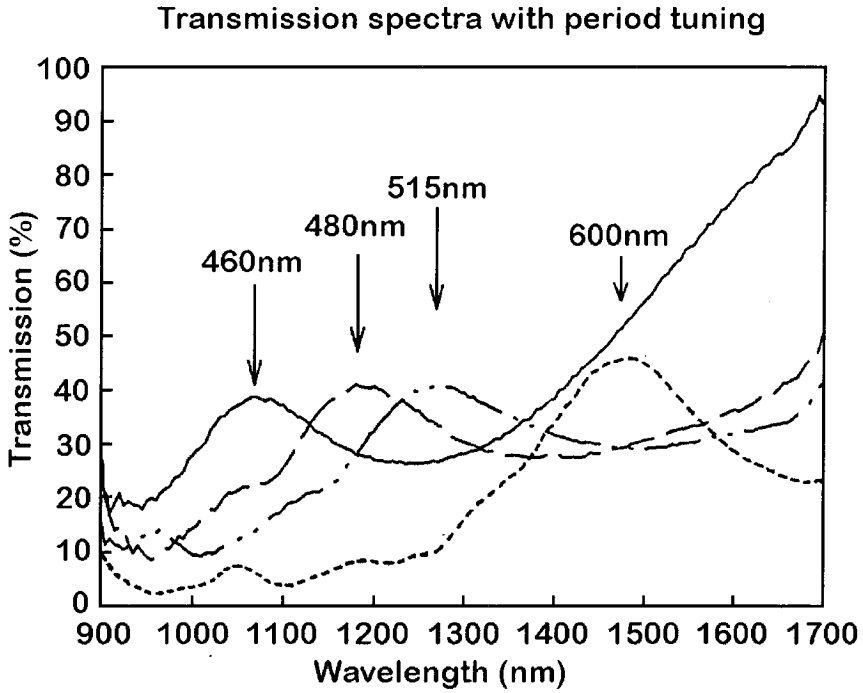

Figure 9.2: A series of transmission spectra show the shift of the conduction band edge by tuning the lattice constant of the structures. The period, which means the center to center spacings on (1,1,1) plane, is $\frac{\sqrt{2}}{2}\times$ lattice constant

9.1.1 Conduction band tuning

Optical measurements are undertaken on the series of microfabricated photonic band gap crystals shown in Figure 9.1. In Figure 9.2 we show transmission as a function of wavelength for the spectra of three of the crystals characterized by Figure 9.1(a), (b), and (c). For comparison, we also include another spectrum from a 850nm lattice spacing crystal which is measured on a separately fabricated GaAs chip. As would be expected when the lattice parameter becomes larger, we observe a shift of the spectral features to higher wavelengths.

When only the sizes of the holes are changed in a series of microfabricated crystals with fixed lattice parameters, we again observe a shift in the spectra. This is shown in Figure 9.3, where we note that crystals with higher porosity shift their spectral features to lower wavelength. This shift can be qualitatively explained by the lower

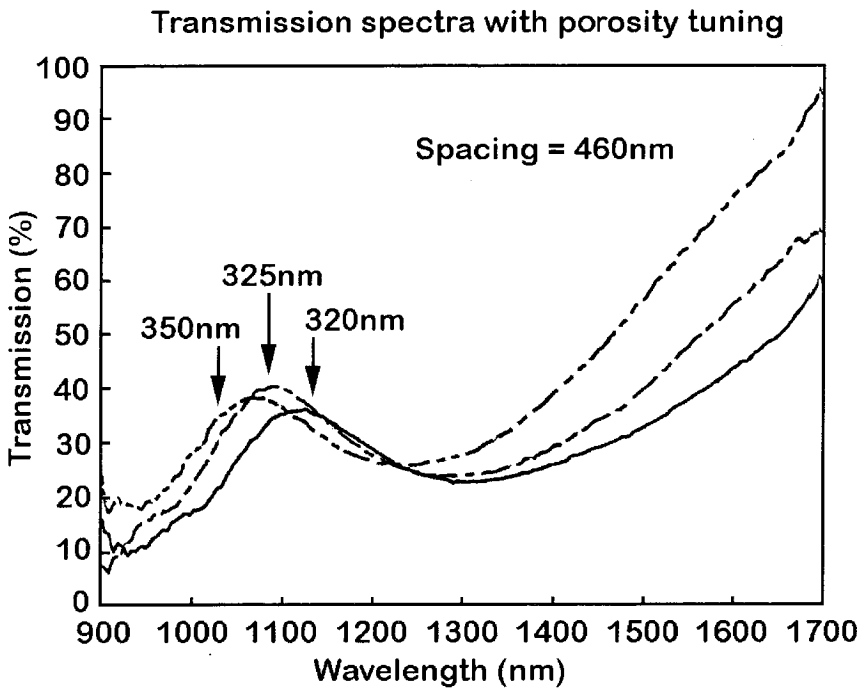

Figure 9.3: A series of transmission spectra show the shift of the conduction band edge by tuning the porosity of the structures which have the same lattice constant. The porosity is proportional to the major hole diameter and the lattice constant

average refractive index of the more porous crystals. The similar spectral shifts shown in Figure 9.2 and 9.3 are also found all over the whole array. We have so far reproduced these measurements on other microfabricated samples, and believe that it is possible to predict the spectral features of photonic crystals by careful control over the microfabrication mask.

9.2 Microwave measurement comparison

A measured optical transmission spectrum of a GaAs photonic crystal was shown by the solid line in Figure 8.18. In this sample, the photonic bandgap lies in the near infrared with a width of about 19% of its mid-gap frequency. The dotted and dashed lines on Figure 9.4 labeled "Constant Diameter" and "Tapered Diameter" correspond to microwave transmission spectra for 17300× scale models made of Stycast with a dielectric constant = 12, i.e., matching the dielectric constant of GaAs. These scale models were fabricated using precision tools in a conventional machine shop, and consisted of 2.5 lattice layers, $(2.5 \times a/\sqrt{3})$, bonded to a thick slab of Stycast material meant to simulate the GaAs substrate.

In order to represent the optical and microwave spectra on the same graph, the microwave-lengths are divided by the same scaling factor, 17300, for the photonic crystal of Figure 8.18. The evaluation of this factor deserves special clarification. At first glance, the GaAs photonic crystal is a compressed version of the "Constant Diameter" microwave model with the dielectric constant scaling relation $\varepsilon_{\mu-wave}(r) = \varepsilon_{optical}(r/s)$, where "$s$" is the ratio of center-to-center spacing between the two structures. However, the microwave model is fabricated using conventional drill bits with a round cross section, while the GaAs photonic crystal is angle etched through a circular hole pattern, producing elliptical cross section cylinders. The eccentricity of the cylinders is given by cos 35.26° = 0.82. This results in a larger remaining volume fraction of dielectric material in the GaAs photonic crystal, and consequently a red-shift in the forbidden gap relative to the round hole case. The actual shift is determined using the oval hole calculations by Qian *etal.*, with infrared refractive

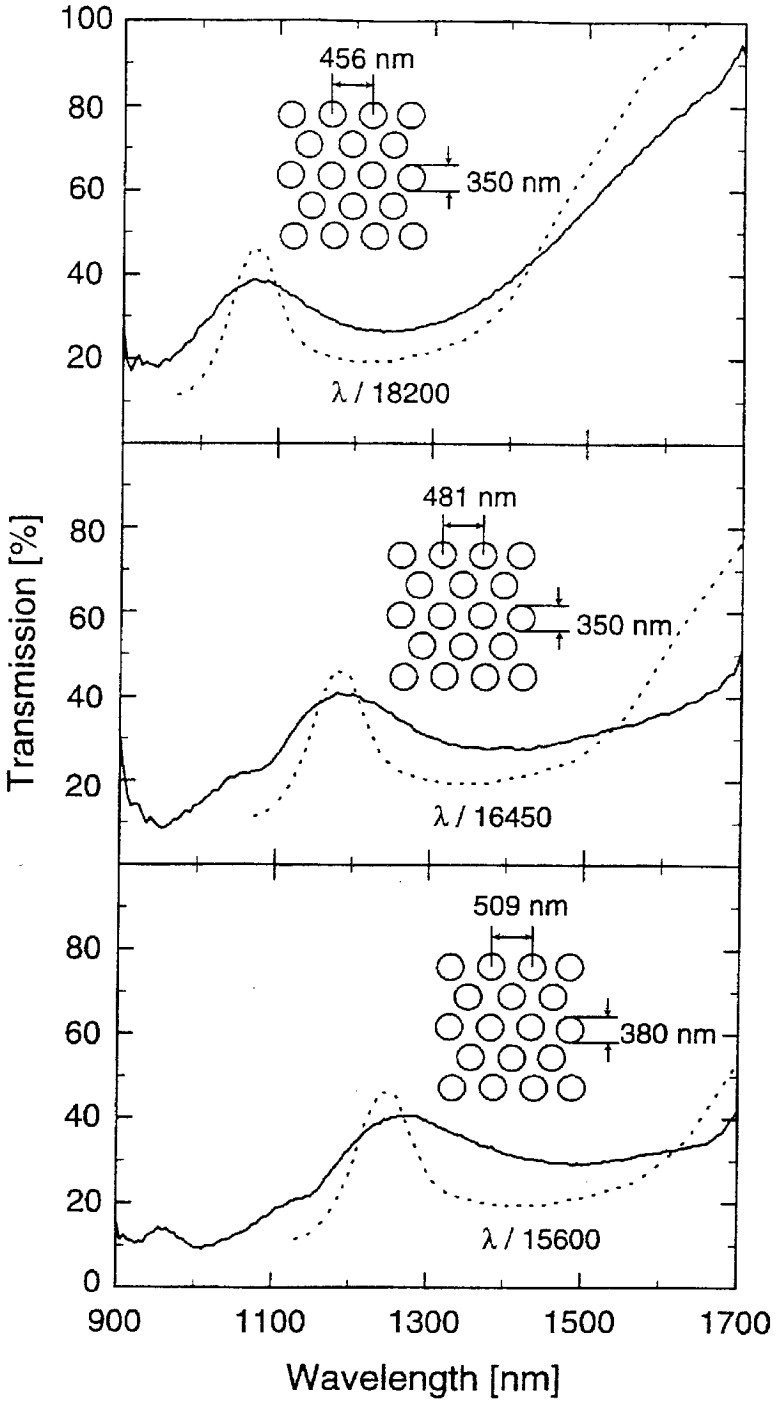

Figure 9.4: Systematic conduction band tuning of 3D photonic crystals, the dotted lines are taken from microwave measurements and scaled down to fit in the same wavelength range

index taken from the literature [7].

"Tapered Diameter" and "Constant Diameter" are meant to distinguish microwave models with and without a taper in the drilled hole diameter, dashed and dotted lines, respectively, shown in Figure 8.18. The "Constant Diameter" microwave scale model attenuates electromagnetic radiation by 95% at mid-gap. The dashed line shown as "Tapered Diameter" represents a similar microwave model, identical at the top surface, but with tapered holes meant to simulate the expected decreased hole diameter in the GaAs photonic crystal as we ion etch into the material. The overall taper was approximately 4.8% per layer or 12% from top to bottom. By weakening the interference effects on which the photonic bandgap depends, the taper considerably degrades the mid-gap attenuation to 80%. Further, since less dielectric material is removed due to the decreasing hole diameter, the band-edges also happen to shift towards longer wavelengths. The mediocre spectral match between the GaAs photonic crystal and the tapered microwave scale model indicates that the structural precision of our current nanofabrication process is no better than 12%. Small variations in hole diameter, as seen in Figure 9.1, are most likely responsible for some inhomogeneous broadening. (Parenthetically, computational modeling of the tapered geometry is sufficiently challenging that it leaves a role for scale model experimentation as done here.)

Further evidence for the accurate scaling between microwave and optical wavelengths is illustrated in Figure 9.4 by the systematic wavelength shift in the conduction band peak as a function of hole diameters and spacings (recorded from SEM micrographs). The dotted lines are the corresponding transmission spectra of the tapered microwave model.

Chapter 10 Discussion

10.1 Fabrication using Al_2O_3 etch masks

We have developed alternative methods for easier pattern transfer and for a higher selectivity between the etch rate of the mask and the semiconductor. Figure 10.1 shows the most recent fabrication procedure used for defining thicker 3D photonic crystals. First, a 200nm AlAs layer and a thin GaAs cap layer are grown by MBE on the top of the GaAs substrate. The sample is then coated with SiO_2 and Au. Next, electron beam lithography defines a triangular array of circular holes which corresponds to the (1,1,1) plane on PMMA. Then this pattern is transferred onto a 50nm thick SiO_2 layer by C_2F_6 reactive-ion etching. The SiO_2 layer serves as an etching mask under Ar/Cl_2 ion beam assisted etching at a 35 degree angle.[12] The three-hole symmetric pattern is transferred into an AlAs layer which is subsequently converted into Al_2O_3 by steam oxidation.[13] We have found that the Al_2O_3 layer has an etch rate selectivity over GaAs larger than 30. This robust Al_2O_3 mask combined with directional-angle ion beam etching can be used to define substantially deeper 3D photonic crystal. Care must be taken when etching in three directions since the holes are at a 35 degree angle to the surface normal. The first angle etch has to thin down the Al_2O_3 mask sufficiently to reduce any shadowing of the holes which must be projected in the other two directions. We have so far made photonic crystals with six repeating layers in depth by using such an Al_2O_3 angle-etch mask. Figure 10.2 shows the SEM image of a cross section of a six layer 3D photonic crystal. This method gives us more freedom in designing the structure compared with our previous work using a Ni or SiO_2 mask.

Figure 10.3 shows a transmission spectrum of a crystal with a conduction band at 1000nm. The attenuation in the bandgap region in this sample reaches 90% in the normal incident direction. We attribute this improvement over our previous work to

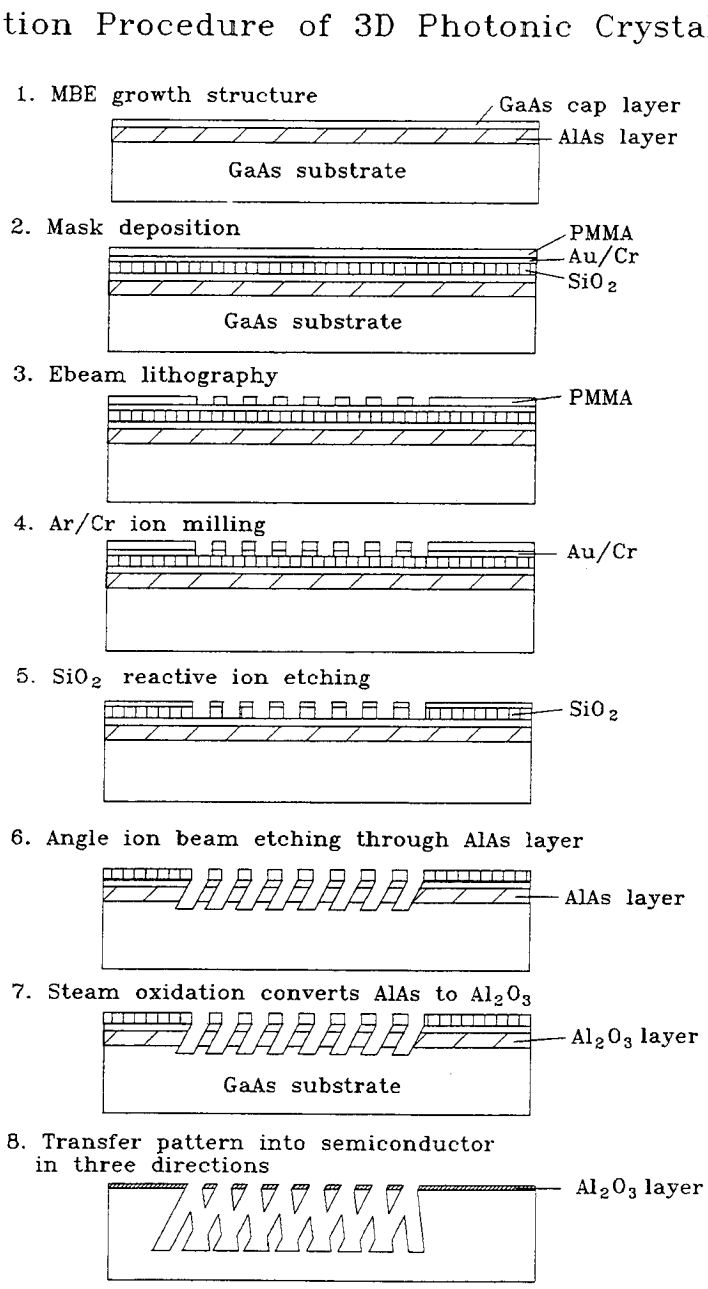

Figure 10.1: Fabrication procedure of 3D photonic crystal using Al_2O_3 etch mask

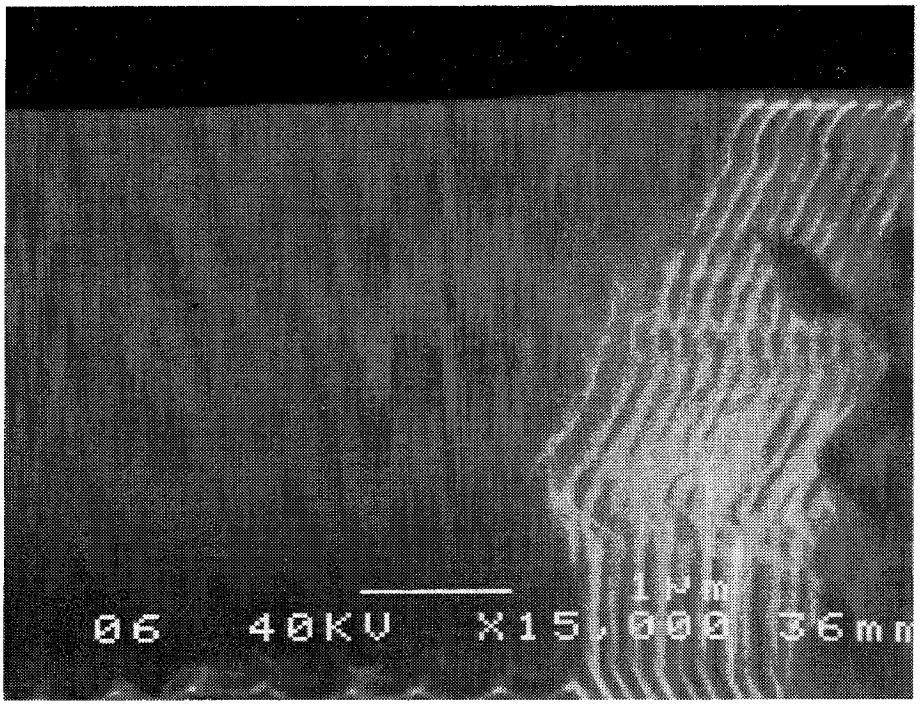

Figure 10.2: SEM image of cross section of a 3D photonic crystal showing six repeating layers

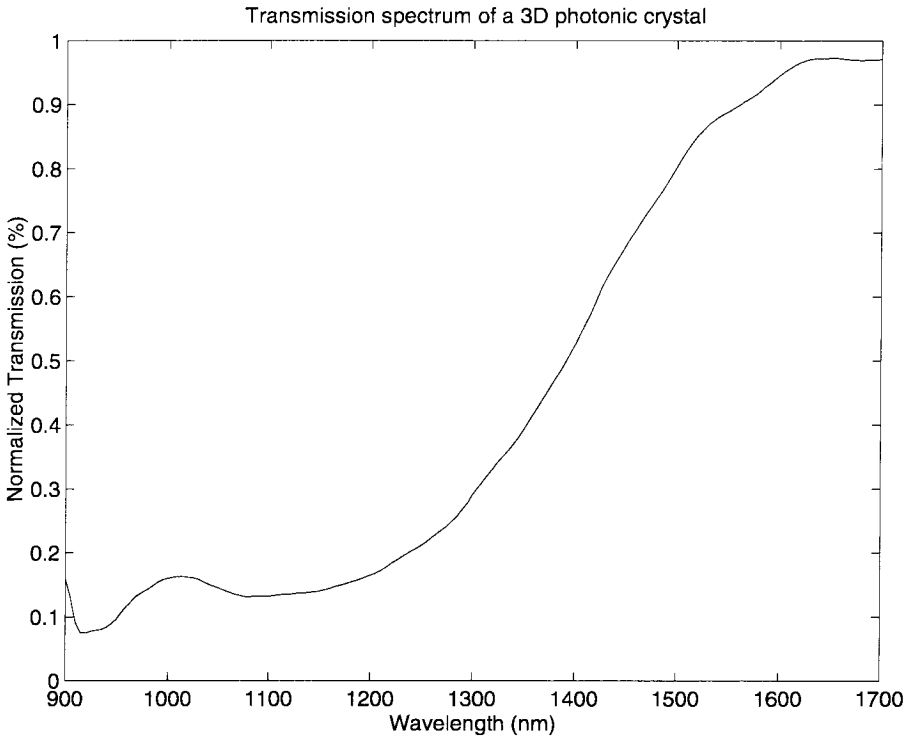

Figure 10.3: A transmission spectrum shows 90% attenuation in the bandgap region resulting from the deeper structure of 3D photonic crystals

the use of Al_2O_3 as an etching mask which increases the number of the periods in depth.

10.1.1 3D mask fabrication

The shadow effect which limits the thickness of a planar mask is a major limitation when fabricating a 3D photonic crystal. Building a three-dimensional mask is one of the obvious solutions to this problem. A good candidate must have several properties. The mold has to be fabricated in a simple and easy way and the mold becomes the most robust mask after an additional process. In the previous session, we have demonstrated the new techniques using steam oxidation of an Al_2O_3 etch mask. We could transfer 3D photonic structures into a thick AlAs layer instead of a GaAs substrate. This patterned AlAs layer serves as a mold. Steam oxidation of this mold can then form a robust 3D mask which no longer has any shadow effect during

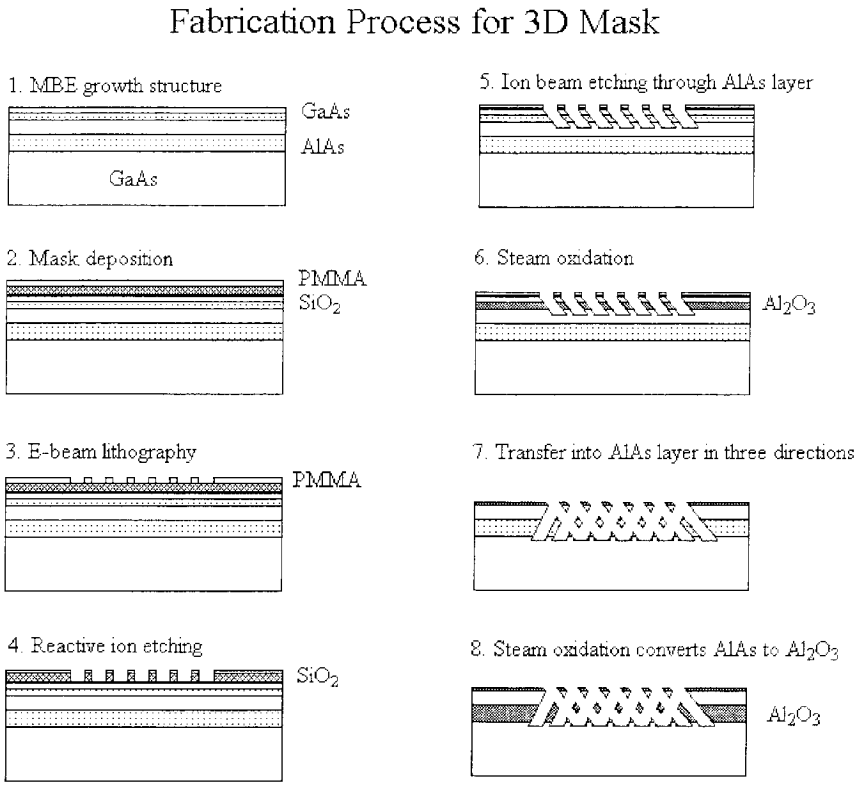

Figure 10.4: Scheme of 3D mask fabrication by steam oxidation of patterned AlAs layer

the angle ion beam etching process. Figure 10.4 shows the fabrication scheme of a three-dimensional mask.

10.2 Summary

We have developed the fabrication method to build high quality 3D photonic crystals. A robust mask along with anisotropic etching condition are the two main requirements in fabricating these 3D photonic crystals. During this research effort, the mask could be significantly improved in both the durability and the simplicity. AlAs with steam oxidation offers the most promising candidate in the GaAs/AlAs material system. Anisotropic etching is also improved when the selectivity of the mask is increased.

Optical characterization is needed to be improved to further examine the reflection properties of these microstructures. Finite-difference time domain calculations were found to be the powerful tools to design and to examine the new 3D photonic crystals geometry. Together with the optimization of nanofabrication techniques, simple and high performance 3D photonic crystals can now be manufactured in the future.

Thus far our best mid-gap attenuation for GaAs nanofabricated photonic crystal has been 90%. This modest performance can be understood by the observation that we are testing the photonic crystal in its most vulnerable k-space direction L_3 where the vertical periodicity is indirectly produced by the intersection of holes below the surface. On the other hand, the periodicity in the lateral directions is lithographically written coherently over the 40×40 μm^2 aperture. Therefore, the optical attenuation in the lateral directions is probably close to ideal. There are six lateral hexagonal facets to the Brillouin Zone, and two vertical hexagonal facets in our geometry. A weighted average indicates that spontaneous emission in all directions would probably be inhibited by $\approx$97%, even though the inhibition in the vertical direction is only 90%.

For stimulated emission, the lasing mode with the highest reflectivity would naturally be sought out, depending on which cavity modes are designed to be supported. The lateral reflectivity is probably more than sufficient to allow lasing in our photonic crystals. We believe that these photonic crystals are already of sufficient quality to allow commencement of experiments on modification of both spontaneous and stimulated emission.

Part IV

Conclusion

Chapter 11 Summary and future direction

This thesis describes all my work during my studies in Caltech. Some of my research was focused on the design and the improvement of fabrication processes which are essential and necessary for my project. We have developed and optimized both high resolution electron beam lithography and anisotropic ion beam etching for nanofabrication process. In the first part of this thesis, the resolution limitation of electron beam lithography was explored. We have successfully modified a scanning electron microscope (Hitachi S-4500II) to a high resolution electron beam writer controlled by a computer pattern generator. With optimized exposure dose and development condition, we have demonstrated 15nm wide nanostructures with 30nm periods both in dot arrays and line gratings using 30kV acceleration voltage and PMMA resist. The ultimate resolution and the flexibility of electron beam lithography opens our view on studying nanostructures. When combined with anisotropic angle ion beam etching, lithographic defined planar patterns are transferred into three-dimensional structures.

We are most interested in the periodic dielectric structures which exhibit very interesting and unique optical properties. These structures are named "photonic crystals." The third part of this thesis is the original work on 3D optical photonic crystals. To microfabricate structures with three-dimensional periodicity requires careful optimization of lithography and etching conditions. The first 3D photonic crystals, Yablonovite, with forbidden bandgap designed in the infrared range, was demonstrated in a GaAs substrate and characterized by transmission measurements. SEM images confirm the geometry of these photonic crystals with up to six repeating layers. Transmission spectrum of photonic crystals shows that the attenuation in the bandgap region reaches 90%. To further confirm the properties of photonic crystals,

an array of photonic crystals exhibiting geometric tuning by lithography were constructed. A series of transmission spectra confirmed the geometric tuning, a good agreement with a microwave model. Although the vertical transmission shows 90% only, the total spontaneous emission inhibition can reach 97% because of the near-perfection in the lateral direction. These optical photonic crystals are expected to be useful in studying single optical mode in a tiny cavity. We believe that these 3D photonic crystals can be manufactured using a simple way in the near future.

Compared with the complicated process procedure of 3D photonic crystals, microfabrication of these 2D periodic structures seems more straightforward. In the second part of this thesis, periodic structures with different functions were researched. Passive optical components such as form-birefringent nanostructures and micropolarizers were introduced by rigorous coupled wave analysis. Good agreement between simulated results and fabricated nanostructures was shown. These artificial single-substrate nanostructures exhibit larger form-birefringence effects ($-\pi$ to π) than natural crystals. With similar design, polarization selective computer generated holograms were introduced and characterized. These holograms show the high polarization contrast ratios (up to 275:1) between first order diffracted TE modes and TM modes. A new approach was presented to design a micropolarizer based on a 2D photonic crystal. The manufacturable micropolarizers exhibit very high extinction ratios (as high as 820:1) between transmitted TM modes and TE modes. These micropolarizers also raise the interest in the application of photonic crystals.

We have shown our capability in design and fabrication of many optical devices such as photonic crystals. We also have shown good agreement between theoretical prediction and experimental results. The presently-developed technology in lithography and etching may have limitations now, but further improvements should be possible. As photonic band engineering attracts more and more attention, and improvement in nanofabrication techniques develops, many applications of photonic crystals such as single-mode light-emitting diodes and polarization selective mirrors could be achieved.

Appendix A Chemically assisted ion beam etching

After definition by lithography, it is necessary to transfer patterns anisotropically without distortion. The condition of wet chemical etching with anisotropy has been demonstrated [9]. But undercutting and crystal facet orientation usually limit the use of wet etching in today's microfabrication. Within the sub-micron range, high aspect ratio structures require highly anisotropic etching. Therefore, energized ions together with reactive gas are the candidates for the anisotropic etching [72, 73, 21, 74, 75, 76].

We have designed an ion beam etching system assisted by reactive gas. Figure A.1 shows the system schematically. A tungsten filament is used as electron source to generate Ar (or inert gas) ions. High electric fields and magnets are added to extract and focus the ion beam. Energized ions bombard the sample covered by mask with the help of reactive gases. Different reactive gases, depending on the materials, can be used to improve the etching selectivity. GaAs, AlAs, InGaAs, or GaN can be etched by Ar ions assisted by Cl_2 gas [21, 74]. There are several advantages using these chemically assisted ion beam etching (CAIBE) system compared with conventional reactive ion etcher (RIE). First, the high energy ions can increase the etching rate and improve the anisotropy of the pattern transfer. Second, the longer distance between ion beam source and the sample gives the freedom of tilting the sample at an arbitrary angle. And high concentration of reactive gases can be added to change the surface chemistry independent of ion source. Table A.1 shows the etching rate for different materials in the CAIBE system. The sample holder can be modified by adding a heater or a cooler to change the temperature of the substrate during the etching process. In situ measurement can be made to control the process.

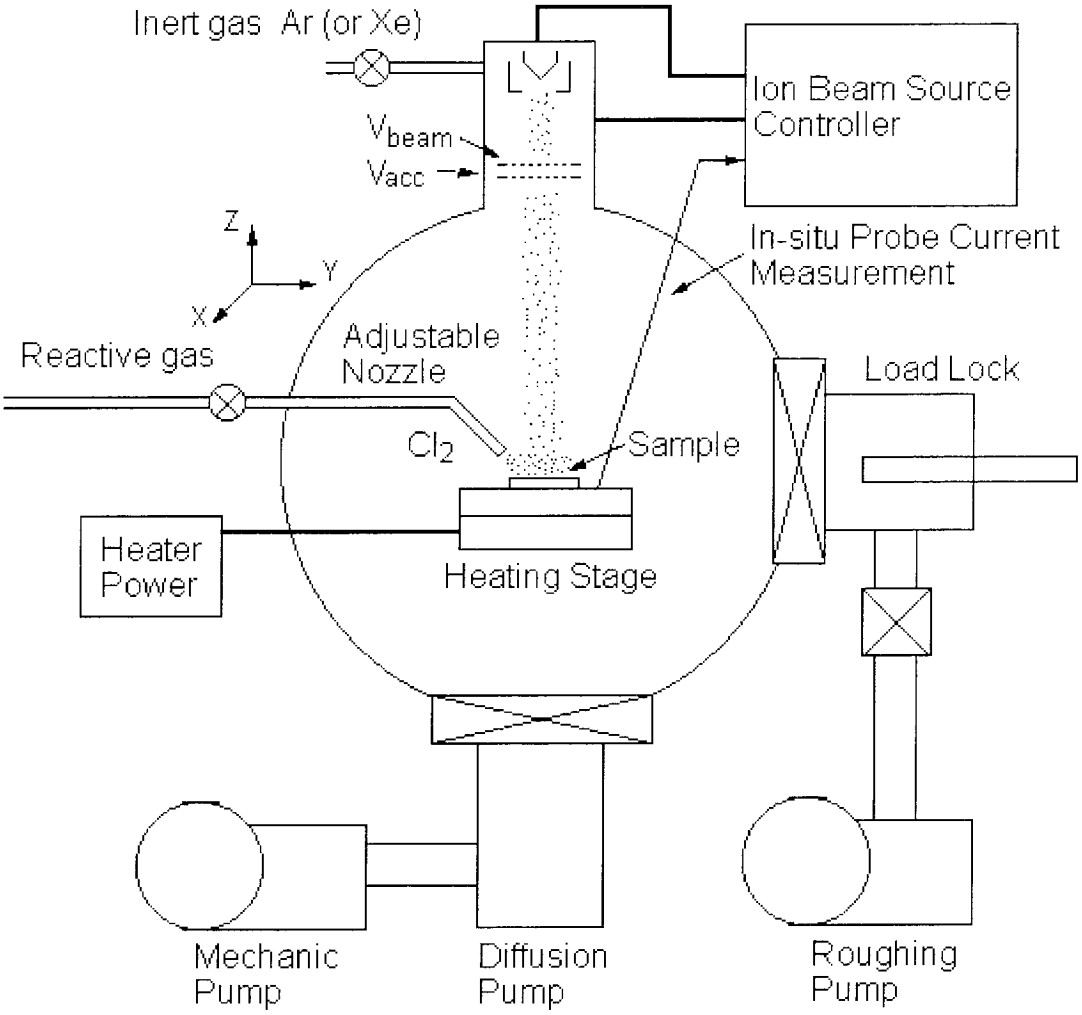

Figure A.1: Chemically assisted ion beam etching system

Table A.1: Etching rate table using our CAIBE system

Material	Etch rate(nm/min)
SiO_2	60
Cr	22
Ni	20
Au	100
Photoresist	150
GaAs	800

Appendix B Steam oxidation of AlAs mask

A robust etch mask is required for high resolution directional ion etching. Typically, it is defined by lift-off or mask amplification procedure. The techniques have been successfully used for high resolution fabrication, but are limited by the total thickness of the mask and the 2D geometry. In order to fabricate high aspect ratio structures or 3D photonic structures, an alternative mask fabrication is introduced [40]. By learning from the experience of fabricating low threshold vertical cavity surface emitting lasers (VCSELs), we have found that an AlAs layer can be easily patterned by chemically assisted ion beam etching and an Al_2O_3 layer has the highest selectivity ($> 40{:}1$) over a GaAs layer. We also learned that an Al_2O_3 layer can be converted from an AlAs layer by steam oxidation process [77, 78, 79, 80, 81]. The chemical reactions of the oxidation process are discussed. The arsenic leaves the structure as arsine (AsH_3), and thus requires hydrogen. The chemical equations are provided below:

$$2AlAs + 6H_2O_{(g)} \longrightarrow Al_2O_3 + As_2O_3 + 6H_2 \quad \text{(B.1)}$$

$$As_2O_3 + 3H_2 \longrightarrow 2As_{(s)} + 3\ H_2O \quad \text{(B.2)}$$

$$2As + 6H \longrightarrow 2AsH_3 \quad \text{(B.3)}$$

Hydrogen might help in accomplishing a more complete removal of arsenic. Porosity of the aluminum oxide seems to allow the arsine to exit the structure and also probably accounts for the discrepency in calculated vs. measured shrinkage in the oxide films.

We use steam oxidation of an epitaxially grown AlAs layer to define high resolution ion etch masks. These masks are extremely robust and form highly selective etch masks for the ion etching of GaAs/$Al_xGa_{1-x}As$ devices after oxidation, and they can be easily defined into intricate 3D structures while still in AlAs form. Figure B.1 shows

the simple sequence of the process. First, an AlAs layer with desired thickness and a GaAs cap layer are grown by MBE on the top of regular GaAs/$Al_xGa_{1-x}As$ devices. The mask is designed as a part of the structures. Then, high resolution features are defined by electron beam lithography on a thin PMMA layer. The PMMA layer is developed in 3:7 cellusive:methanol. The PMMA pattern is then transferred through an AlAs layer by a short ion beam etch with Cl_2 reactive gas. This AlAs layer is oxidized by steam oxidation conducted in a field oxide furnace with N_2 bubbled through hot H_2O at temperature between 300-400°C. During the oxidation procedure, the AlAs layer is laterally oxidized underneath the GaAs cap layer. The precise oxidation rate depends strongly on the furnace temperature and Al concentration of $Al_xGa_{1-x}As$ layer [78]. Finally, the pattern is transferred onto underlying structures by chemically assisted ion beam etching using Al_2O_3 layer as a mask.

We have obtained high selectivity (> 40:1) between GaAs/$Al_xGa_{1-x}As$ etch rate and Al_2O_3 erosion rate and high aspect ratio (> 10:1) structures. Figure B.2 shows a SEM image of high aspect ratio structures using Al_2O_3 as an etch mask. The top layer is an Al_2O_3 mask layer. The volume shrinkage from AlAs to Al_2O_3 is about 10%. The thermal expansion causes the lift off of the mask. The image shows the clean interface between mask and structure. This problem can be solved by using high Al concentration $Al_xGa_{1-x}As$ layers. Room temperature oxidation also exhibits interesting phenomena. Figure B.3 shows tube structures fabricated due to the room temperature oxidation of small holes followed by ion beam etching.

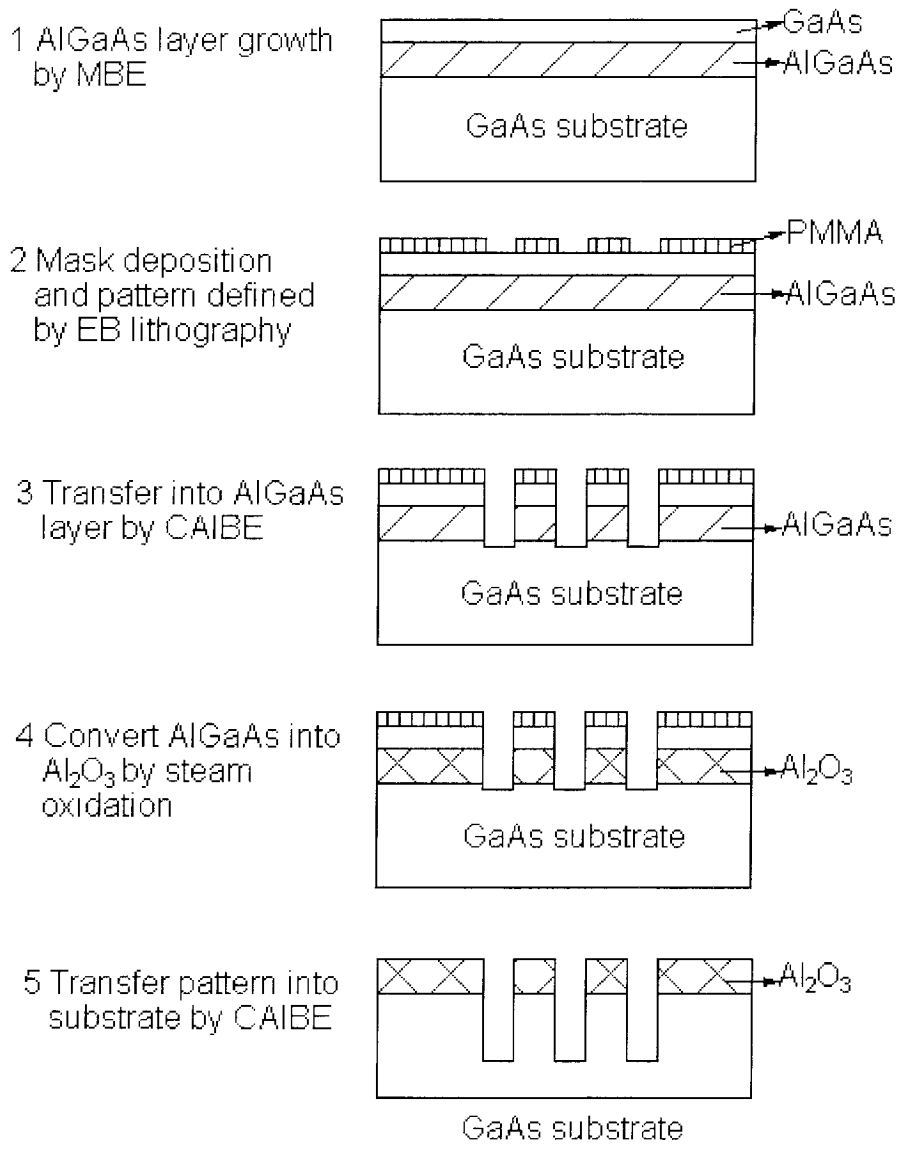

Figure B.1: Fabrication procedure using Al_2O_3 etch mask

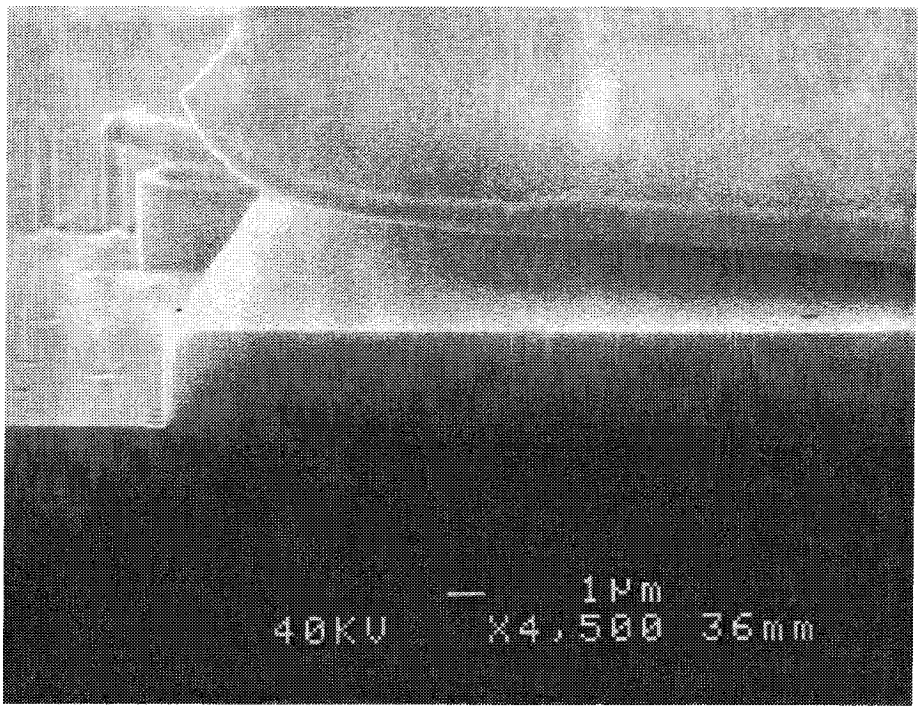

Figure B.2: SEM image of high aspect ratio structure using Al_2O_3 etch mask

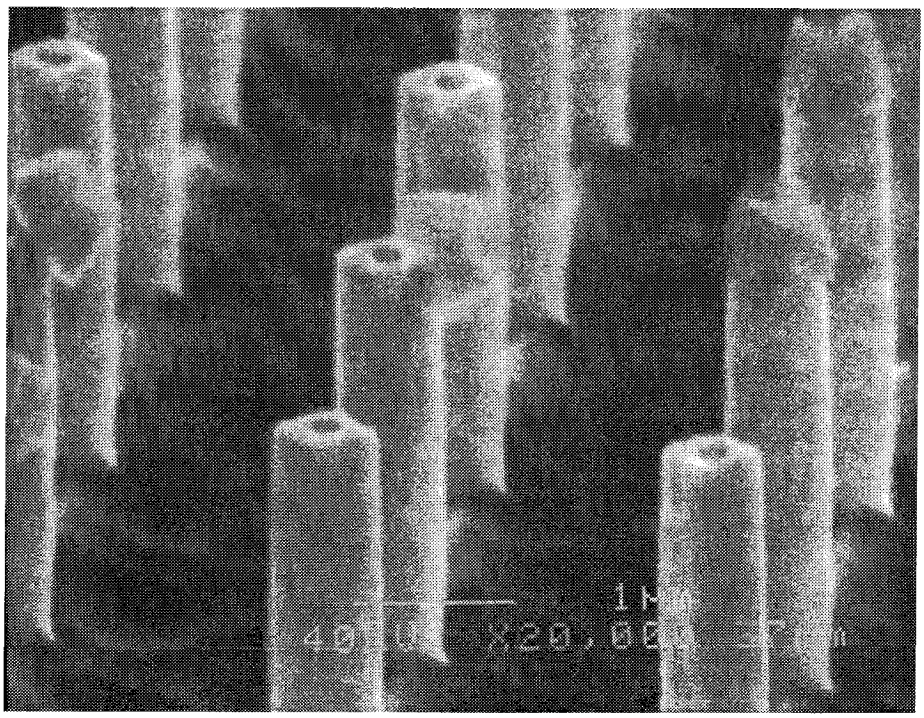

Figure B.3: SEM image of tube structures due to room temperature oxidation

Bibliography

[1] S. Okazaki, "Lithographic technologies for future ULSI," *Appl. Surface Sci.*, vol. 70, p. 603, 1993.

[2] M.G. Moharam and T. K. Gaylord, "Diffraction analysis of dielectric surface-relief gratings," *J. Opt. Soc. Am.*, vol. 72, p. 1385, 1982.

[3] E. Yablonovitch, "Photonic band-gap structures," *J. Opt. Soc. Am. B*, vol. 10, p. 283, 1993.

[4] K.M. Ho, C.T. Chan, C.M. Soukoulis, R. Biswas, and M. Sigalas, "Photonic band gaps in three dimensions: New layer-by-layer periodic structures," *Solid State Comm.*, vol. 89, p. 413, 1994.

[5] E. Yablonovitch, T.J. Gmitter, and K.M. Leung, "Photonic band structure: The face-centered-cubic case employing nonspherical atoms," *Phys. Rev. Lett.*, vol. 67, p. 2295, 1991.

[6] K. S. Yee, "Numerical solution of initial boundary value problems involving maxwell's equations in isotropic media," *IEEE Trans. Antenna. Propagat.*, vol. AP-14, p. 302, 1966.

[7] G.X. Qian and K.M. Leung, "Photonic band structure: The case of oval holes," *Phys. Rev. B*, vol. 44, p. 11482, 1991.

[8] G. Moore, "VLSI, What does the future hold," *Electron Aust.*, vol. 42, p. 14, 1980.

[9] S.M. Sze, *VLSI Technology.* New York: McGraw-Hill, 1988.

[10] S. Matsui, "Nanostructure fabrication using electron-beam and its application to nanometer devices," vol. 85, p. 629, 1997.

[11] F. Cerrina, "Application of X-rays to nanolithography," vol. 84, p. 644, 1997.

[12] J.I. Goldstein, D.E. Newbury, P. Echlin, D.C. Joy, C. Fiori, and E. Lifshin, *Scanning Electron Microscopy and X-ray Microanalysis.* New York and London: Plenum Press, 1981.

[13] T.H.P. Chang, "Proximity effect in electron-beam lithography," *J. Vac. Sci. Technol.*, vol. 12, p. 1271, 1975.

[14] R.E. Howard, H.G. Craighead, L.D. Jackel, P.M. Mankiewich, and M. Feldman, "Electron-beam lithography from 20 to 120 keV with a high-quality beam," *J. Vac. Sci. Technol.*, vol. B 1, p. 1101, 1983.

[15] H.G. Craighead, "10nm resolution electron-beam lithography," *J. Appl. Phys*, vol. 55, p. 4430, 1984.

[16] B.P. Van der Gaag and A. Scherer, "Microfabrication below 10 nm," *Appl. Phys. Lett.*, vol. 56, p. 481, 1989.

[17] W. Chen and H. Ahmed, "Fabrication of high aspect ratio silicon pillars of < 10 nm diameter," *Appl. Phys. Lett.*, vol. 63, p. 1116, 1993.

[18] W. Chen and H. Ahmed, "Fabrication of 5-7nm wide etched lines in silicon using 100keV electron-beam lithography and polymethylmethacrylate resist," *Appl. Phys. Lett.*, vol. 62, p. 1499, 1993.

[19] W. Xu, J. Wong, C.C. Cheng, R. Johnson, and A. Scherer, "Fabrication of ultra-small magnets by electroplating," *J. Opt. Soc. Am. B*, vol. 13, p. 2372, 1995.

[20] I.G. Salisbury, R.S. Timsit, S.D. Berger, and C.J. Humphreys, "Nanometer scale electron beam lithography in inorganic materials," *Appl. Phys. Lett.*, vol. 45, p. 1289, 1984.

[21] A. Scherer, B.P. Van der Gaag, E.D. Beebe, and P.S.D. Lin, "Fluoride etch masks for high-resolution pattern transfer," *J. Vac. Sci. Technol.*, vol. B 8, p. 28, 1990.

[22] G.S. Chen, C.B. Boothroyd, and C.J. Humphreys, "Electron-beam-induced crystallization transition in self-developing amorphous AlF_3 resists," *Appl. Phys. Lett.*, vol. 69, p. 170, 1996.

[23] O. Dial, C.C. Cheng, and A. Scherer, "Fabrication of high density nanostructures by electron beam lithography," *(to be published).*

[24] A. Yariv and P. Yeh, *Optical Waves in Crystals.* New York: Wiley, 1984.

[25] F. Xu, J.E. Ford, and Y. Fainman, "Polarization-selective computer-generated holograms: design, fabrication, and applications," *Appl. Opt.*, vol. 34, p. 256, 1995.

[26] F. Xu, R.C. Tyan, P.C. Sun, Y. Fainman, C.C. Cheng, and A. Scherer, "Fabrication, modeling, and characterization of form-birefringent nanostructures," *Opt. Lett.*, vol. 20, p. 2457, 1995.

[27] F. Xu, R.C. Tyan, P.C. Sun, Y. Fainman, C.C. Cheng, and A. Scherer, "Form-birefringent computer-generated holograms," *Opt. Lett.*, vol. 21, p. 1513, 1996.

[28] S.M. Rytov *Sov. Phys. JETP*, vol. 2, p. 466, 1956.

[29] I. Richter, P.C. Sun, F. Xu, and Y. Fainman, "Design considerations of form birefringent microstructures," *Appl. Opt.*, vol. 34, p. 2421, 1995.

[30] M. G. Moharam and T. K. Gaylord, "Rigorous coupled-wave analysis of planar grating diffraction," *J. Opt. Soc. Am.*, vol. 71, p. 811, 1981.

[31] S. T. Peng, T. Tamir, and H. L. Bertoni, "Theory of periodic dielectric waveguide," *IEEE Trans. Microwave Theory Tech.*, vol. MTT-23, p. 123, 1975.

[32] K. Knop, "Rigorous diffraction theory for transmission phase gratings with deep rectangular grooves," *J. Opt. Soc. Am.*, vol. 68, p. 1206, 1978.

[33] C.C. Cheng and A. Scherer, "Fabrication of 3-D photonic bandgap crystals," *J. Vac. Sci. Technol. B*, vol. 13(6), p. 2696, 1995.

[34] J. O'Brien, O. Painter, R. Lee, C.C. Cheng, A. Yariv, and A. Scherer, "Lasers incorporation 2d photonic bandgap mirrors," *Elect. Lett.*, vol. 32, p. 2243, 1996.

[35] T.F. Krauss, R.M. De La Rue, and S. Brand, "Two-dimensional photonic-bandgap structures operating at near-infrared," *Nature*, vol. 383, p. 699, 1996.

[36] D.R. Smith, R. Dalichaouch, N. Kroll, S. Schultz, S.L. McCall, and P.M. Platzman, "Photonic band structure and defects in one and two dimensions," *J. Opt. Soc. Am. B*, vol. 10, p. 314, 1993.

[37] M.M. Sigalas, C.M. Soukoulis, E.N. Economou, C.T. Chan, and K.M. Ho, "Photonic band gaps and defects in two dimensions: Studies of the transmission coefficient," *Phys. Rev. B*, vol. 48, p. 14121, 1993.

[38] R.C. Tyan, P.C. Sun, A. Scherer, and Y. Fainman, "Polarizing beam splitter based on the anisotropic spectral reflectivity characteristic of form-birefringent multilayer gratings," *Opt. Lett.*, vol. 21, p. 761, 1996.

[39] R.C. Tyan, A.A. Salvekar, H.P. Chou, C.C. Cheng, A. Scherer, P.C. Sun, F. Xu, and Y. Fainman, "Design, fabrication, and characterization of form-birefringent multilayer polarizing beam splitter," *J. Opt. Soc. Am. A*, vol. 14, p. 1627, 1997.

[40] C.C. Cheng, R. Tyan, Y. Fainman, G. Witzgall, E. Yablonovitch, and A. Scherer, "New fabrication techniques for high quality photonic crystals," *J. Vac. Sci. Technol. B*, vol. 15(6), p. 2764, 1997.

[41] J.L. Jewell, J.P. Harbison, A. Scherer, Y.H. Lee, and L.T. Florez, "Vertical-cavity surface-emitting lasers – design, growth, fabrication, characterization," *IEEE J. Quantum Electron.*, vol. QE-27, p. 1332, 1991.

[42] A. Scherer, J.L. Jewell, and J.P. Haribson *Opt. Phot. News*, vol. 2, p. 9, 1991.

[43] E. Yablonovitch, "Inhibited spontaneous emission in solid-state physics and electronics," *Phys. Rev. Lett.*, vol. 58, p. 2059, 1987.

[44] S. John, "Strong localization of photons in certain disordered dielectric superlattices," *Phys. Rev. Lett.*, vol. 58, p. 2486, 1987.

[45] J.D. Joannopoulos, R.D. Meade, and J.M. Winn, *Photonic Crystals: Molding the Flow of Light.* Princeton, NJ: Princeton Univ. Press, 1995.

[46] C. Kittel, *Introduction to Solid State Physics, 6th ed.* New York: John Wiley & Sons, Inc., 1986.

[47] N.W. Ashcroft and N.D. Mermin, *Solid State Physics.* New York, NY: Saunders College Publishing, 1976.

[48] E. Yablonovitch and T.J. Gmitter, "Photonic band structure: The face-centered-cubic case," *Phys. Rev. Lett.*, vol. 63, p. 1950, 1989.

[49] E. Yablonovitch and T.J. Gmitter, "Photonic band structure: The face-centered-cubic case," *J. Opt. Soc. Am. A*, vol. 7, p. 1792, 1990.

[50] E. Yablonovitch and K.M. Leung, "Photonic band-structure — nonspherical atoms in the face-centered cubic case," *Physica B*, vol. 175, p. 81, 1991.

[51] E. Yablonovitch, T.J. Gmitter, R.D. Meade, A.M. Rappe, K.D. Brommer, and J.D. Joannopoulos, "Donor and acceptor modes in photonic band structure," *Phys. Rev. Lett.*, vol. 67, p. 3380, 1991.

[52] E.M. Purcell, "Spontaneous emission probablities at radio frequencies," *Phys. Rev.*, vol. 69, p. 681, 1946.

[53] Y. Yamamoto, S. Machida, and W.H. Richardson, "Photon number squeezed states in semiconductor-lasers," *Science*, vol. 225, p. 1219, 1992.

[54] P.W. Anderson, "Absence of diffusion in certain random lattices," *Phys. Rev.*, vol. 109, p. 1492, 1958.

[55] K.M. Ho, C.T. Chan, and C.M. Soukoulis, "Theory of photon bands in three-dimensional periodic dielectric structures comment," *Phys. Rev. Lett.*, vol. 66, p. 393, 1991.

[56] D.R. Smith, S. Schultz, N. Kroll, M. Sigalas, K.M. Ho, and C.M. Soukoulis, "Experimental and theoretical results for a two-dimensional metal photonic band-gap cavity," *Appl. Phys. Lett.*, vol. 65, p. 645, 1994.

[57] S.L. McCall, P.M. Platzman, R. Dalichaouch, D. Smith, and S. Schultz, "Microwave propagation in two-dimensional dielectric lattices," *Phys. Rev. Lett.*, vol. 67, p. 2017, 1991.

[58] S.Y. Lin and G. Arjavalingam, "Tunneling of electromagnetic waves in two-dimensional photonic crystals," *Opt. Lett.*, vol. 18, p. 1666, 1993.

[59] D.F. Sievenpiper, M.E. Sickmiller, and E. Yablonovitch, "3D wire mesh photonic crystals," *Phys. Rev. Lett.*, vol. 76, p. 2480, 1996.

[60] E. Ozbay, A. Abeyta, G. Tuttle, M. Tringides, R. Biswas, C.T. Chan, C.M. Soukoulis, and K.M. Ho, "Measurement of a three-dimensional photonic band gap in a crystal structure made of dielectric rods," *Phys. Rev. B*, vol. 50, p. 1945, 1994.

[61] S. Fan, P.R. Villeneuve, R.D. Meade, and J.D. Joannopoulos, "Design of three-dimensional photonic crystals at submicron length scales," *Appl. Phys. Lett.*, vol. 65, p. 1466, 1994.

[62] T.F. Krauss and R.M. De La Rue, "Optical characterization of wave-guide based photonic microstructures," *Appl. Phys. Lett.*, vol. 68, p. 1613, 1996.

[63] A. Yariv, *Optical Electronics, 4th ed.* New York: Saunders College Publishing, 1991.

[64] H.A. Haus, *Waves and Fields in Optoelectronics.* Englewood Cliffs, NJ: Prentice-Hall, Inc., 1984.

[65] K.M. Ho, C.T. Chan, and C.M. Soukoulis, "Existence of a photonic gap in periodic dielectric structures," *Phys. Rev. Lett.*, vol. 65, p. 3152, 1990.

[66] K.Sakoda, "Optical transmittance of a two-dimensional triangular photonic lattice," *Phys. Rev. B*, vol. 51, p. 4672, 1995.

[67] M. Bartsch, M. Dehler, M. Dohlus, F. Ebeling, P. Hahne, R. Klatt, F. Krawczyk, M. Marx, Z. Min, T. Pröpper, D. Schmitt, P. Schütt, B. Steffen, B. Wagner, T. Weiland, S.G. Wipf, and H. Wolter, "Solution of Maxwell's equations," *Comp. Phys. Comm.*, vol. 72, p. 22, 1992.

[68] G. Mur, "Absorbing boundary conditions for the finite-difference approximation of the time-domain electromagnetic-field equations," *IEEE Trans. Electromagn. Compat.*, vol. EMC-23, p. 377, 1981.

[69] B. D'Urso, O. Painter, J. O'Brien, T. Tombrello, A. Yariv, and A. Scherer, "Modal reflectivity in finite-depth two-dimensional photonic-crystal microcavities," *J. Opt. Soc. Am. B*, vol. 15, p. 1, 1998.

[70] C.C. Cheng, V. Arbet-Engels, E. Yablonovitch, and A. Scherer, "Lithographic conduction band tuning of 3-D photonic crystals," *J. Vac. Sci. Technol. B*, vol. 14(6), p. 4110, 1996.

[71] W.M. Robertson, G. Arjavalingam, R.D. Meade, K.D. Brommer, A.M. Rappe, and J.D. Joannopoulos, "Measurement of photonic band structure in a two-dimensional periodic dielectric array," *Phys. Rev. Lett.*, vol. 68, p. 2023, 1992.

[72] A. Scherer and M.L. Roukes, "Quantum device microfabrication - resolution limits of ion-beam patterning," *Appl. Phys. Lett.*, vol. 55, p. 377, 1989.

[73] H. Yamada, H. Ito, and H. Inaba, "Anisotropic reactive ion etching technique of GaAs and AlGaAs materials for integrated optical-device fabrication," *J. Vac. Sci. Technol. B*, vol. 3, p. 884, 1985.

[74] S.W. Pang, G.A. Lincoln, R.W. McClelland, P.D. DeGraff, M.W. Geis, and W.J. Piacentini, "Effects of dry etching on GaAs," *J. Vac. Sci. Technol. B*, vol. 1, p. 1334, 1983.

[75] K. Asakawa and S. Sugata, "GaAs and AlGaAs anisotropic fine pattern etching using a new reactive ion beam etching system," *J. Vac. Sci. Technol. B*, vol. 3, p. 402, 1985.

[76] K. Asakawa and S. Sugata, "Damage and contamination-free GaAs and AlGaAs etching using a novel ultrahigh-vacuum reactive ion beam etching system with etched surface monitoring and cleaning method," *J. Vac. Sci. Technol. A*, vol. 4, p. 677, 1986.

[77] A.R. Sugg, E.I. Chen, N. Holouyak, K.C. Hsieh, J.E. Baker, and N. Fiuiegau, "Effects of low-temperature annealing on the native-oxide of $Al_xGa_{1-X}As$," *J. Appl. Phys.*, vol. 74, p. 3880, 1993.

[78] K.D. Choquette, R.P. Schneider, K.L. Lear, and K.M. Gelb, "Low-threshold voltage vertical-cavity lasers fabricated by selective oxidation," *Elect. Lett.*, vol. 30, p. 2043, 1994.

[79] D.L. Huffaker, D.G. Deppe, K. Kumer, and T.J. Rogers, "Native-oxide defined ring contract for low-threshold vertical-cavity lasers," *Appl. Phys. Lett.*, vol. 65, p. 97, 1994.

[80] E.I. Chen, N. Holouyak, and M.J. Ries, "Planar disorder-defined and native-oxide-defined photopumped AlAs-GaAs superlattice minidisk lasers," *J. Appl. Phys.*, vol. 79, p. 8204, 1996.

[81] D.L. Huffaker, J. Shia, H. Deng, C.C. Liu, D.G. Deppe, and B.G. Streetman, "Improved mode-stability in low-threshold single-quantum-well native-oxide," *Appl. Phys. Lett.*, vol. 65, p. 2642, 1994.